(79)

Residual Actuation and Stiffness Properties of Piezoelectric Composites: Theory and Experiment

by

Alessandro Pizzochero

B.S. Aerospace Engineering
The University of Texas at Austin, 1994

Submitted to the Department of Aeronautics and Astronautics in Partial Fulfillment of the Requirements for the Degree of

Master of Science in Aeronautics and Astronautics
at the
Massachusetts Institute of Technology

February 1998

Signature of Author: _____
Department of Aeronautics and Astronautics
September 22, 1997

Certified by: _____
Professor Nesbitt W. Hagood
Associate Professor, Department of Aeronautics and Astronautics
Thesis Supervisor

Accepted by: _____
Professor Jaime Peraire
Chair, Graduate Office

Residual Actuation and Stiffness Properties of Piezoelectric Composites: Theory and Experiment

by

Alessandro Pizzochero

SUBMITTED TO THE DEPARTMENT OF AERONAUTICS AND ASTRONAUTICS ON SEPTEMBER 22, 1997, IN PARTIAL FULFILLMENT OF THE REQUIREMENTS FOR THE DEGREE OF MASTER OF SCIENCE.

Active Fiber Composites have been developed as a new technology for the actuation and sensing of structures. Many engineering applications, aerospace in particular, could benefit greatly from the use of active composites to address the issue of vibration suppression. Some of the key benefits are increased robustness to damage, actuation capability, and efficient integration into structures. One pertinent example is the use of active fiber composites in helicopter blades for higher harmonic control. The active composites employed in this environment must withstand the extreme stresses in the spinning blade and provide sufficient actuation capability.

This work attempts to characterize and model the effective stiffness and actuation properties of active composite materials under high uniaxial tensile loads. The motivations for this undertaking are to obtain effective material properties as damage accumulates in the active element, and to identify the mechanisms affecting stiffness and actuation to improve the material. A unified model with predictive capability for overall laminate effective material properties was developed. Key model assumptions include a constant linear elastic fiber recovery length and a Weibull form for fiber strength. A one dimensional shear lag model was employed to characterize the load transfer between the composite's layers. In order to validate this model several experiments were conducted on interdigitated electrode piezoelectric fiber composites embedded in E-glass laminae. Stiffness and actuation data were obtained by performing active tests: specimens were subjected to increasing tensile loads and measurements of actuation under load were taken at selected strain levels.

A considerable amount of experimental data was available for correlation with the model. Characteristic fiber statistical data was extrapolated from fiber fragmentation patterns, and was subsequently used to describe actuation and stiffness properties. Some variability in measured fragmentation, actuation, and stiffness properties was observed during the experimental work. Nevertheless excellent agreement with the model was successfully demonstrated. These results illustrated the merits of this characterization effort. This model can now be used as a viable tool for further enhancement of active fiber composite technology.

Thesis Supervisor: Prof. Nesbitt W. Hagood, Ph. D.,
Associate Professor of Aeronautics and Astronautics

Acknowledgments

This work was jointly funded by AFOSR under contract #SSRC F49620-95-2-0097 and ARO under contract #DAAH04-95-1-0104. The authors wish to thank them for their support on this project.

There are many people who deserve my gratitude for their effort in the support of my Masters studies. Special thanks go to my advisor, Nesbitt Hagood, for his continued support and for providing a challenging, but rewarding, twist to my studies. I would also like to thank him for the freedom I was given to pursue a wide variety of interesting tasks during the course of this work. Then there is the invaluable input provided by my fellow researchers: the quality of my learning experience at MIT has been greatly improved by sharing ideas and working together. Aaron Bent, John Rodgers, Kamyar Ghandi, Tim Glenn, Patrick Trapa, my UROPs and everyone else (you know who you are): thanks for all your help! I am forever grateful to my parents for their continued support in pursuing my studies: I hope I didn't cause you too much trouble! Most importantly, I would like to thank my wife for helping me in the good and the bad times. Magda, thank you very much; I hope I didn't overwork you too much in the last two-week crunch! Lastly I would like to thank everyone in AMSL and SSL for helping throughout the good, the bad, and the M∞ times...

Table of Contents

List of Figures

List of Tables

Chapter 1

Introduction

1.1 Motivation

Active Fiber Composites (AFCs) are an innovative combination of active and passive materials to create a new hybrid material capable of meeting the increasingly high demands of current and upcoming high-tech engineering applications. The basic concept of an AFC calls for small diameter electro-ceramic fibers in a soft polymer matrix, and is typically configured as an active ply for planar actuation. AFCs were introduced at MIT approximately four years ago as a means for improvements in solid state actuation technology. As applications became more demanding, it was evident that the then current means of structural actuation, typically monolithic piezoceramics, were not capable of meeting the new challenges. Although piezoceramics seemed to be ideally suited for planar structural actuation applications, they suffered from particular disadvantages associated with reliability, strength, and large scale distributed control. AFCs have been specifically developed to address these limitations. The main driver for this development is the benefit that can be derived from the application of active materials to a wide variety of potential applications.

The application of AFCs to structures leads to the definition of an *active structure*. Active structures are defined as structures that possess an intrinsic capability to change geometry or to change their response to various loading conditions. While this goal in itself is not new, AFCs provide the capability to attain this goal more effectively as a result of improved performance, strength and conformability, and large scale actuation.

Potential applications have been identified in vibration suppression in rotorcraft and airplanes, which can lead to reduced maintenance, increased structure life and passenger comfort, and improved flight performance. The helicopter environment has been historically characterized by considerable maintenance, high noise levels, operator fatigue and limited payload capability. Unsteady aerodynamic loads acting on the rotor system result in considerably high levels of vibrations. This is particularly magnified in forward flight when the blades on one side of the helicopter encounter a different velocity field than on the other side (one is moving into the wind, the other away from it). One of the possible solutions to reduce the effects of this problem is to change the twist distribution along the rotating blade according to the azimuth angle [1]. This approach involves controlling the pitch of individual blades without affecting the collective pitch for general flight functions. To this end, the use of active composites *integral* to the helicopter blade has been suggested. With this configuration , the active materials (actuators) would have to operate against the torsional stiffness of the blade, since they are directly in the structural load path. And this is where the challenge lies: *it is critical to ensure that actuation and mechanical properties are not lost due to the effect of structural loads, in*

particular tension loads. For the rotorblade application the actuator system must be capable of blade pitch changes of ±2° at the tip [2]. Therefore the design must account for damaged actuators to provide the proper level of actuation (including the effect of coupling with structural stiffness). The application of active composites to helicopter rotorblades for higher harmonic control (HHC) is currently under research at MIT [3]. Other similarly promising applications range from the acoustic control of helicopter /aircraft fuselages, submarines and torpedoes, and automotive vehicles to airplane wing de-icing.

1.2 Objectives

The goal of this work is to develop a methodology for modeling and predicting the effect of large tensile loads on the actuation capability and mechanical properties of active fiber composites. A subsidiary objective is to experimentally validate the model. This work is directly involved with the advancement of the active rotorblade concept. The results, however, are applicable to many other applications. A set of requirements has been determined for this application, and they drive the selection of the actuator configuration: in its present form, the selected actuator configuration calls for a PZT-based active composite ply to be embedded in a host structure.

1.3 Background

Piezoelectric monolithic wafers embedded in a host laminate, have typically been applied as a means of providing actuation capabilities to a wide variety of structures. Unfortunately, monolithic wafers are not well suited for a

more diverse array of applications; the limiting factors being a combination of performance and packaging difficulties. Particularly important are the actuator/sensor's performance, robustness and conformability; properties effectively displayed in composite materials. For *integral* application in helicopter blades, conformability becomes critical in order to properly embed the actuators in the blade while still maintaining performance and robustness. Composite materials have historically been successful at providing tailored properties as well as robustness to damage. The basic concept of a composite is in fact that of a material which can withstand internal damage by virtue of internal load transfer. For instance, if brittle fibers in a tough matrix are used, then load transfer across a fiber crack occurs through the matrix (which also provides load sharing). This has lead to the application of composite technology to active materials resulting in the development of active composite materials [4-10]. An illustration of the active composite concept is provided in Fig. 1.1a, and a cross-section photomicrograph of an active composite is shown in Fig. 1.1b.

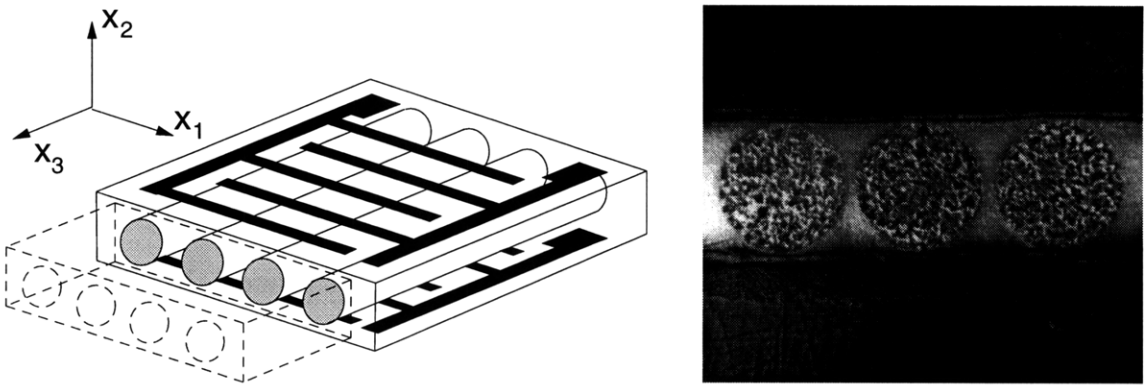

(a) (b)

Figure 1. 1. (a) Illustration of the active composite material concept: piezoelectric fibers, matrix, and interdigitated electrodes are represented. (b) Photomicrograph of the cross section of a laminated active composite.

To address the above limitations, active composite materials have been developed as a lamina composed of active fibers embedded in a matrix material and enclosed between electrodes [4,6]. This active lamina can then be integrated in a host structure (typically composite or surface bonded). Illustrated in Figure 1.1a are the critical components that comprise an active fiber composite: (1) piezoelectric fibers, which provide stiffness and actuation capability, (2) polymer matrix, which surrounds, protects, and distributes load among the fibers, and (3) interdigitated electrodes, which effectively deliver the electric field. A fourth element is associated with AFCs but is not illustrated in Figure 1.1a: reinforcing fibers or plies. Reinforcing material is an essential component as it provides increased robustness and structural support.

The benefits of the AFC configuration have been emphasized with the aid of models for the characterization of performance parameters. Some of the improvements include:

- *Performance.* The active lamina is characterized by good stiffness and bandwidth properties, characteristic of piezoceramics. The composite configuration improves damage tolerance through alternate load paths. Additionally the unidirectional nature of the fibers creates anisotropic actuation, which is desirable for tailored performance (induced strain). When combined with interdigitated electrodes, this leads to a configuration with high actuation energy densities due to the more effective delivery of electric field to the piezoelectric fibers.
- *Conformability and Robustness.* The combination of fine, strong ceramic fibers and soft, tough matrix provides load transfer mechanisms that increase robustness to damage, and provides reinforcements for higher ultimate static strain levels. This characteristic is further magnified when reinforcing fibers or plies are introduced in the configuration. The increased robustness provides for improved conformability as active composites can then be applied to more irregular or curved surfaces/structures.

The current manifestation of AFCs, illustrated in Figure 1.1a, is called interdigitated electrode piezoelectric fiber composite (IDEPFC). The piezoelectric Fibers are aligned in-plane in order to couple to in-plane forces, with fiber orientation taken to be along the 3-axis. The unidirectional fiber alignment

permits maximum fiber volume fraction, and hence, maximum actuation authority over the host structure. Current fibers used in manufacture are commercially manufactured using an extrusion process, while new methods are also being investigated for reducing fabrication costs and providing large-scale manufacturing capability. The matrix material is responsible for playing both a mechanical and electrical role in the composite structure: it surrounds and protects the ceramic fibers, distributes the load among the active and passive fibers, and acts to re-distribute load around cracks or fiber discontinuities. The matrix can also carry the electric field to the active fibers: this requires maximizing matrix dielectric to improve composite performance. When necessary, the matrix can be combined with dopants and chemical additives for this purpose. Interlaminar electrodes are present to deliver the electric field to the active composite and are constructed of a copper or silver pattern on a Kapton substrate. The electrode also provides electrical insulation from surrounding passive layers and is independent of the ceramic, which desensitizes the actuation performance from material cracking. The electrode patterns have fingers of alternating polarity, and are exact mirror images on the top and bottom faces. Poling is predominantly along the 3-axis direction. Application of an electric field produces primary actuation along the fibers (shown as an extension in Figure 1.1a), and an out of phase transverse actuation (a contraction) perpendicular to the fibers. The application of the electric field is effectively displayed in Figure 1.2. The cross-section, showing a 1/8 section of the representative volume element of a single fiber between electrode fingers, is taken along planes of symmetry in all three axes.

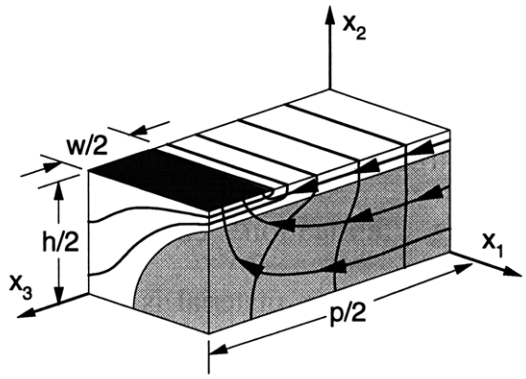

Figure 1.2. Section of model representation of IDEPFC actuator showing equipotential and field lines (with arrows). The electrode is represented by the shaded region at the top.

While much work has been devoted to predicting actuation properties of active composites [5,8], little is still known about the degradation of actuation capability and stiffness properties under high loading. Particularly important is the ability to maintain sufficient stiffness and effective actuation capabilities in heavily loaded structures such as helicopter rotor blades, where actuators must withstand the extreme stresses of the blade environment.

The effect of high-load conditions on composite material structures is typically manifested as cracking of either the matrix material or of the reinforcing fibers, depending on their relative strengths and stiffness. Although composite materials technology is relatively new, many models exist for the characterization of either matrix or fiber fracture under load [11-13]. However, no work has been done to provide similar tools for active composite materials. In the case of active composite materials, the problem is complicated by the necessity to characterize the effect of damage on the actuation/sensing capabilities. This will involve a study of the load transfer mechanisms as they occur in general composites. Many

researchers have developed exceptionally detailed load transfer models, ranging from single-fiber composite to multi-fiber composite models [14-17]. Investigations have also been made into load transfer models with interacting fibers; these analyses are however mostly suited to numerical simulations as no closed form solution is available.

1.4 Approach

This work concerns the evolution of damage in laminated active composite materials with a tough matrix and brittle piezoelectric actuators (fibers) embedded in structural plies; additionally the residual properties of the composite after damage has been introduced are of interest. The active composites in question are subjected to tensile loads only, with no out of plane deformations. In this case, it is assumed that damage under load occurs in the form of fracture in the active fiber. Therefore modeling degradation will entail (1) identifying the mechanisms behind fiber fracture in the active element and (2) the corresponding effect on overall laminate properties.

Chapter 2 will concern the modeling of active composites under load. The problem of the evolution of passive fiber fragmentation has been extensively studied in the past. Researchers have developed models based on the underlying fiber statistical strength and fiber/matrix interfacial properties [5,18]. The typical model studied, commonly referred to as a single fiber composite, is composed of a finite fiber in an infinite matrix. This will serve as starting point for the *Fiber Cracking Model* section. Load transfer models are extensively available for composite materials. In its simplest form, a micromechanics shear lag model

characterizes the stress distribution along a fiber embedded in a matrix [14]. For the more complex case of load transfer between two different media across a matrix, a similar analysis can be performed. In particular results are available for the load transfer between an active and a passive structural layer [19]. The subsection on *Effective Properties* of a material fragment will be developed from these concepts. Each fragment then has different effective properties based on its length and its interaction with the elastic layer. As a result, an averaging scheme was developed to derive overall composite effective properties. Details of this scheme will be given in the *Effective Composite Properties* subsection. As a composite material is first loaded and damaged, it will have acquired permanent damage. Upon further loading, the material will behave according to the amount of damage present. Characterization of these residual properties will be approached in the subsection on *Residual Property Characterization.*

Chapter 3 will detail the issues associated with the experimental methods. A thorough description of the most current manufacturing process will be provided in the *Test Article Manufacture* section. Steps will be outlined in detail, including techniques used for the manufacture of the interdigitated electrodes, and all preliminary performance tests. The section on *Testing Procedures* will then discuss test methods and equipment used for the experimental characterization. Two basic tests were conducted on the available pool of composites: actuation under load and stiffness measurements. The last section, *Test Matrix*, will detail the planned testing schedule and what type of data will be collected from each composite.

Chapter 4 will then concern validating the modeling effort with experimental data. Here, results from several test specimens will be analyzed and correlated to provide accurate representation of material behavior. Effectively, the validation effort is mainly comprised of two parts. The first relates to fitting the main model statistical parameters to the available fragmentation data. The second will build on this knowledge and apply the results of the modeling effort to the measured performance data.

Chapter 5 closes the thesis with principal conclusions from each chapter, and recommendations for future work in characterizing active fiber composites.

Chapter 2

Modeling Actuation and Stiffness

2.1 Introduction

One of the key challenges facing this work is to understand what drives and affects the performance of active fiber composites subject to uniaxial tensile loads. In order to achieve this understanding, a modeling effort will be undertaken with the goal of characterizing actuation performance and stiffness. Experiments have helped identify two key phenomena that affect the composite's response. First there is the load-induced *fiber fragmentation* and, second, the effect of *shear lag* on load transfer between the active and passive composite elements. The main focus of this chapter will be the integration of available fiber fracture and load transfer theories into a unified model which will give predictive capability for the characterization of actuation and stiffness. Of interest are effective material properties as well as the identification of mechanisms and parameters affecting the composite's performance. Particularly important is the characterization of residual properties once damage has been introduced in the structure. A thorough understanding of this phenomenon is essential for the successful integration into heavily loaded structures; in particular determining the effect of damage on the composite's capability to still

fulfill its functional requirements. Overall, the emphasis will be on the accumulation of damage within the composite, i.e. the main cause of degraded performance.

The subject of this work is an active multi-fiber composite with brittle non-interacting active fibers, and with linear elastic shear transfer to/from reinforcing passive fibers. This modeling chapter will deal with the mechanisms affecting actuation and stiffness performance of active composites. Theories will be presented to characterize the effect of statistical, geometrical and material properties on composite response. The objectives for this chapter are:

- to identify and model the details of fiber fragmentation/cracking,
- to characterize the effective properties of a material fragment based on shear lag considerations, and the corresponding effect on the overall composite response, and
- to model the response of the composite once damage has been accumulated in the structure.

While all derivations presented in this chapter refer to laminae, the results can be equally applied to the case of reinforcing fibers surrounding active fibers or of piezoelectric plates in laminates.

This chapter is divided into four major sections describing: active fiber cracking, effective property characterization of a material fragment, averaged fragment properties to yield overall composite response, and composite response once damage has been accumulated in the structure, i.e. residual properties. A theory for the characterization of the evolution of fiber fragmentation will be presented for a composite loaded monotonically in tension along its longitudinal

axis. Subsequently the fragmentation results will be integrated into a mechanical shear lag model which will provide a framework for the characterization of the mechanical response of a composite fragment (the length of which is equal to the fiber fragment length). With the composite effective properties identified, the next section will develop an averaging scheme to obtain overall composite properties. The last section will then be concerned with the modeling of actuation and stiffness properties of a damaged composite, i.e. previously loaded to a certain static strain value.

2.2 Fiber Cracking Model

2.2.1 Introduction

The objective of this section is to model the evolution of fragmentation with applied stress as a function of the underlying statistical strength and interfacial shear transfer. The subject of this section is a fiber surrounded by matrix and structural material; loads are transferred to/from the fiber and the structural material through the intermediate layer of matrix material. Ultimately it is desirable to obtain a relationship between applied stress and the resulting number of breaks and distribution of fragment lengths in the composite. This problem has been solved for a single-filament-composite with constant interfacial shear stress around the fiber cracks [11]. Curtin's work concerns itself with standard brittle, passive fibers in a tough matrix, an arrangement very similar in nature to the active fiber composite concept. While some of the assumptions for Curtin's fragmentation model do not directly apply to the case

of active composites, it provides a general framework for an accurate representation of fiber fracture.

The key factors underlying the performance of general composite materials are the fiber/matrix interfacial properties and the *in situ* tensile strength of the fibers. The interfacial properties determine how an applied load is transferred to the fibers through the matrix while the fiber strength determines the ultimate load-bearing capacity of the composite. The fiber strength must be described statistically, however, because the strength is controlled by the distribution of defects along the fiber length; furthermore, the average fiber strength depends on fiber length. Longer fibers will have a higher number of defects which ultimately favors fiber fracture. Defects typically are in the form of volume voids: the larger the fiber, the more voids. Since fiber fragmentation in a composite under high loads ultimately leads to the formation of fragments with lengths of the order of the fiber's diameter, it is important to know the strength distribution at these lengths.

2.2.2 Fiber Recovery Length

One important parameter for the characterization of fiber fragmentation is the *fiber recovery length*. The recovery length is the length of fiber over which stresses recover from a value of zero, at the fiber end (crack), to the applied stress value. In actuality the applied stress value is never fully recovered along the fiber length due to the nature of the linear shear lag/transfer phenomenon. This leads to complications for the accurate characterization of load transfer. By employing simplifying assumptions, however, it is possible to reduce the problem

to a more manageable one. Let us take a look at the case of elastic shear lag in a simple composite where fibers are surrounded solely by matrix material.

For materials where the fiber and matrix are well bonded, an elastic shear lag analysis accurately describes the stress transfer between the fibers and the matrix. This analysis is very commonly employed in general composite analysis and is originally due to H. L. Cox (1952). In its simplicity it captures very effectively the underlying mechanism of load transfer within a composite material. The basic assumption is that the matrix transfers stress between broken and intact fibers by deforming elastically in shear. In this case the fiber and the matrix have equal displacements at the interface as opposed to slippage in the case of constant shear stress interfaces.

In order to quantify the stress transfer between fiber and matrix, consider a fiber fragment of length L embedded in an appropriate volume of matrix as illustrated in Figure 2.1. The fiber/matrix group can then be referred to as a representative volume element.

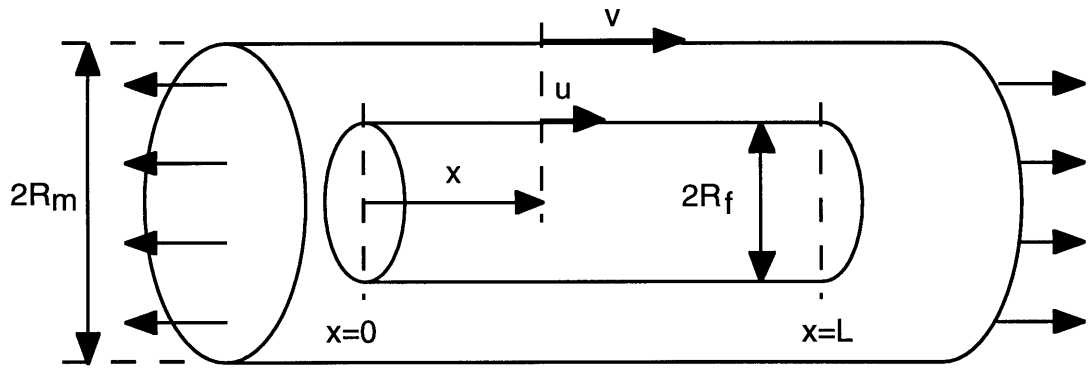

Figure 2.1. Simple shear lag model of fiber embedded in a volume of matrix.

If the representative volume element is subjected to a strain, ε, assume that the load in the fiber varies according to

$$\frac{dP_f(x)}{dx} = H(u - v) \tag{1}$$

where $P_f(x)$ is the load carried in the fiber at a distance x from the end, u is the longitudinal displacement in the fiber, v is the corresponding displacement if the fiber were absent (or the displacement remote from the fiber), and H is a constant that depends on the geometrical arrangement of fibers and matrix and on the elastic moduli. Relating the load to the strain in the fiber yields

$$P_f(x) = E_f A_f \frac{du}{dx} \tag{2}$$

where A_f is the fiber cross-sectional area and du/dx is the fiber strain. By definition,

$$\frac{dv}{dx} = \varepsilon = \text{constant}. \tag{3}$$

Differentiating equation (2) and substituting into (3) yields the following differential equation:

$$\frac{d^2P_f}{dx^2} = H\left(\frac{P_f}{E_f A_f} - \varepsilon\right). \tag{4}$$

Solutions to equation (4) are of the form:

$$P_f(x) = E_f A_f \varepsilon + R\sinh(\beta x) + S\cosh(\beta x) \tag{5}$$

where,

$$\beta = \sqrt{\frac{H}{E_f A_f}}. \tag{6}$$

The boundary conditions in this case are P_f=0 at x=0, x=L and lead to the following expression for the stress distribution in the fiber:

$$\sigma_f = E_f \varepsilon \left\{ 1 - \frac{\cosh\left[\beta\left(\frac{L}{2} - x\right)\right]}{\cosh\left(\beta\frac{L}{2}\right)} \right\}. \tag{7}$$

In order to derive an expression for the constant H, assume that $2R_m$ is the mean center to center spacing of the fibers. Let $\tau(r)$ be the shear stress in the direction of the fibers on a plane parallel to the fiber axis. At the surface of the fiber ($r=R_f$):

$$\frac{dP_f}{dx} = -2\pi R_f \tau(R_f) = H(u - v) \tag{8}$$

therefore,

$$H = -\frac{2\pi R_f \tau(R_f)}{u - v}. \tag{9}$$

Now, let w be the actual displacement of the matrix close to the fiber. At the fiber-matrix interface there is no slippage (w=u) and at $r=R_m$, w=v. For the matrix to be in equilibrium,

$$2\pi r\tau(r) = \text{constant} = 2\pi R_f \tau(R_f) \tag{10}$$

therefore the shear strain in the matrix is given by:

$$\frac{dw}{dr} = \frac{\tau(r)}{G_m} = \frac{R_f \tau(R_f)}{rG_m} \tag{11}$$

and by integrating over the radial position:

$$\Delta w = \frac{R_f \tau(R_f)}{G_m} \ln\left(\frac{R_m}{R_f}\right). \tag{12}$$

Recalling that $\Delta w = (v-u)$, then

$$H = \frac{2\pi G_m}{\ln\left(\frac{R_m}{R_f}\right)} \tag{13}$$

and ($A_f = \pi R_f^2$) finally

$$\beta = \frac{1}{R_f}\sqrt{\left(\frac{G_m}{E_f}\frac{2}{\ln\left(\frac{R_m}{R_f}\right)}\right)}. \tag{14}$$

Additionally, by combining equations (7) and (8) it is possible to get an expression for the shear stress in the fiber:

$$\tau(x) = E_f \varepsilon \left\{ \frac{1}{R_f} \sqrt{\left[\frac{G_m}{E_f} \frac{2}{\ln\left(\frac{R_m}{R_f}\right)} \right]} \frac{\sinh\left[\beta\left(\frac{L}{2} - x\right)\right]}{\sinh\left(\beta \frac{Ll}{2}\right)} \right\}. \qquad (15)$$

The stress and shear stress distribution along the fiber axis are illustrated in Figure 2.2. Note that the stress at the center of a fragment never quite reaches the applied stress in an infinitely long fiber.

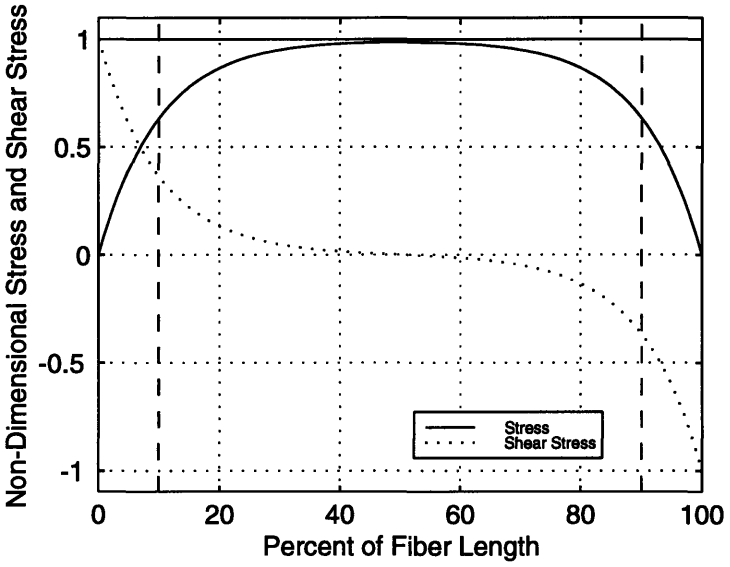

Figure 2.2. Illustration of shear lag transfer along a fiber. The dashed vertical lines indicate the location at a distance 1/β from the fiber end. This is the point where the shear stress is reduced to 36.8% of its value at the fiber end. The continuous horizontal line at 1 indicates the non-dimensional far-field stress value.

There is, however, a length over which most of the stress has been recovered. For the case of elastic shear lag this distance is 1/β, the shear lag

length. This is the distance over which stress transfer occurs. The normal stress is effectively recovered at a distance $1/\beta$ from the fiber end: this is the distance where the shear stress is reduced to 36.8% of its maximum value at the fiber end. For this reason the shear lag length $1/\beta$ is an indicative parameter for the characterization of shear transfer in a composite material. It gives a good indication of the scale effects involved when analyzing a composite material's properties.

Effectively, a certain fiber length around a fracture may be considered ineffective as stress must recover from zero at the crack location to a finite value, approaching the far-field value, somewhere inside the fiber. It is normally assumed that further fiber cracks can occur only outside of the recovery region. The reason being that the largest stresses occur in the middle portion of the fiber. Curtin assumed the recovery length to vary linearly with applied stress, and that the far-field stress value would be recovered at the end of the ineffective length [5]. His analysis showed this is a viable assumption, although work was being done to include the actual behavior. It is interesting to note that other researchers have been able to produce similar fragmentation results [18]. Further work has been performed by running a Monte Carlo simulation which yields results that compare very favorably [20].

In this thesis it is assumed that the model developed by Curtin can be applied to a multi-fiber composite with non-interacting fibers. In this treatment, however, the recovery length is assumed to be *constant* and linear as a simplification of the linear elastic shear transfer around a crack, and is independent of applied stress. This is effectively equivalent to including the

effect of reinforcing fibers in the fragmentation process as their tight positioning around the active fibers provides rapid load transfer (linear elastic). It is also assumed that no further breaks can occur within the recovery region. As may be seen in the following example on the evolution of fragmentation, this is a slightly inaccurate portrayal of the actual phenomenon. Strictly speaking, maintaining a constant linear recovery length implies that a portion of the original recovery length will see increasing loads, therefore adding to the possible occurrence of a break. This effect has been neglected as it would most likely have minimal impact on the fragmentation process.

With these consideration in mind it is now possible to look at a sample fragmentation process. Consider a hypothetical single fiber composite subjected to a tensile test: this leads to the development of a progression of breaks as illustrated in Figure 2.3. Let δ be the constant fiber stress recovery length. Also assume there is a statistical description of the number of defects of a certain strength. Then, when applying an increasing stress some defects will fail at a certain stress level. In this example only one fracture occurs at each stress level. This is only a simplification; certainly more than one fracture can occur at once, depending on the strength distribution. As illustrated in Figure 2.3, the first fracture occurs at a stress σ_1. As a result of the crack the stress recovers linearly from a value of zero (at the location of the crack) to the far-field applied value of σ_1 over a distance equal to the recovery length (δ). The applied stress is then raised to a larger value σ_2; at this new stress level crack number 2 is formed. At this point three fragments have been formed, all of length greater than 2δ. At stress σ_3 the third crack is then formed. This time, however, the crack develops

within a distance twice that of the recovery length (2δ) from the nearest crack. Since the stress recovers linearly at a fixed rate (slope) from the crack, then to the right of crack number 3 there is not enough space for a full recovery to σ_3. This creates a fragment of length greater than δ but smaller than 2δ, which cannot incorporate new breaks at larger stresses, as the maximum stress it can see is fixed and occurs in the middle of the fragment. This stress can be no larger than the currently applied value. The only case when it can be equal to the applied far-field value is illustrated when the fourth crack develops. At a stress σ_4 crack 4 is formed exactly at a distance 2δ from the nearest crack. The resulting fragment is 2δ long and the maximum stress, σ_4, occurs over an infinitesimal length in the middle of the fragment

The foundation for Curtin's model may be traced back to the original work performed by Widom regarding the distribution of gaps produced by the random sequential addition of hard spheres on an infinite line [13]. Curtin was faced with the problem of characterizing the statistics and distribution functions for equisized fragments placed at fixed positions along a line, and Widom's work on spheres provided an equivalent solution. His work on the problem of hard spheres provided a framework for the derivation of the theory of probability distribution for fiber strength at the length scale of micromechanical load transfer around a fiber fracture.

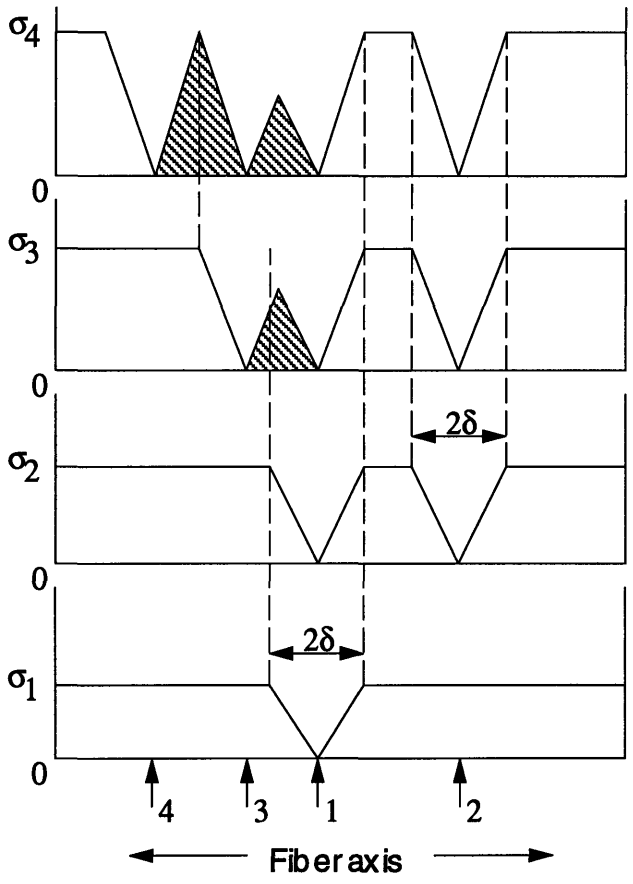

Figure 2.3. Evolution of fragmentation with increasing stress. δ is the fiber stress recovery length. Arrows indicate new fractures. Note the constant recovery length surrounding each crack, except in the case when a new crack occurs at a distance less than 2δ from a previous crack (crack 3).

In terms of the mathematical representation of the driving equations, the constant recovery length simplifies Curtin's original work. The computational advantages are particularly significant in terms of speeding the fragmentation algorithms.

2.2.3 Weibull Distribution

Most reinforcing fibers are strong but brittle. The fiber strength is governed by the fracture toughness of the fibers and the maximum flaw size in

the gage length being tested. The statistical distribution function first used to describe such "weakest link" problems was proposed by Weibull (1951). Using the two parameter version of the statistical model, the probability of survival of a length L of fiber at a stress σ is:

$$P_s(\sigma) = \exp\left[-\frac{L}{L_o}\left(\frac{\sigma}{\sigma_o}\right)^{\rho}\right] \tag{16}$$

or of the same specimen failing

$$P_f(\sigma) = 1 - \exp\left[-\frac{L}{L_o}\left(\frac{\sigma}{\sigma_o}\right)^{\rho}\right], \tag{17}$$

where σ_o and L_o are a reference stress and length respectively, and ρ is the Weibull modulus. Most notable is the effect of the Weibull modulus: a large value indicates a narrow distribution of strengths, i.e. a more closely deterministic strength distribution. The probability of failure as described in equation (17) is illustrated in Figure 2.4.

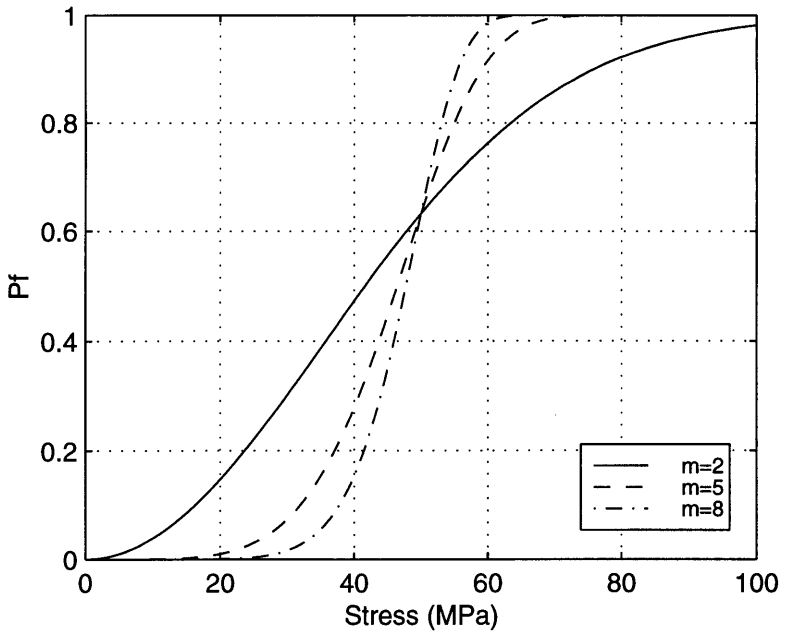

Figure 2.4. Example of probability of failure for a fiber at different Weibull moduli and with L=0.1 m, L_o=0.1 m, and σ_o=50 MPa. At small stresses, the probability of failure is very small. As stress increases the probability of failure becomes higher. For composites with a wider range of strength (smaller Weibull modulus), an increase in stress will produce greater probability of failure.

Given that fibers have a distribution of strengths it is important that fiber strengths are accompanied either quoted in terms of the parameters of the Weibull distribution or are accompanied by the gage length under test. It must be noted that the above refers to a single fiber, therefore very low strengths are possible. In a composite this is effectively compensated by the fact that multiple fibers are present and the matrix material provides stress transfer capability.

2.2.4 Statistics of Fiber Fragmentation

The evolution of fracture in a fiber is generally characterized by the number of defects of a certain strength present in the material. In the case of Curtin's work the distribution of number of defects of strength σ in a fiber of

length L, μ, is assumed to be of the Weibull form. The theory, however, is not restricted to this special case. For a fiber of length L, the Weibull form for the fiber strength distribution in question is:

$$\mu(\sigma,L) = \frac{L}{L_o}\frac{\rho}{\sigma_o}\left(\frac{\sigma-\sigma_{pre}}{\sigma_o}\right)^{\rho-1} \tag{18}$$

where L_o is the fiber gage length appropriate to the scale parameter σ_o, σ_{pre} is the compressive prestress present in the active fiber, and ρ is the Weibull modulus. This form is formulated to fit in a Poisson distribution where the intensity is equal to $\mu(\sigma,L)$ [20]. Note that this form for $\mu(\sigma,L)$ assumes that defects in the fiber are spatially uncorrelated and thus that the probability of finding any type of defect scales linearly with fiber length. The scale parameters are significant in that σ_o is the applied stress required to cause exactly (on average) one failure in a fiber of length L_o. Multiplying by a stress increment $\Delta\sigma$ gives $\mu(\sigma,L)\Delta\sigma$ which is the number of defects of strength between σ and $\sigma+\Delta\sigma$ in a length L of fiber. Assuming N is the number of fiber fragments currently present, then the evolution of fragments as stress is increased may be described as:

$$\frac{dN}{d\sigma} = \mu(\sigma,L^*) \tag{19}$$

where L^* is the remaining breakable fiber length. L^* is determined by removing twice the recovery length, 2δ, around existing cracks, and removing all fragments which can no longer fracture (those shorter than 2δ). L^* may be expressed as an integral over the fragment distribution:

$$L^* = N\int_{2\delta}^{\infty}(x-2\delta)P(x;n,\delta)dx \qquad (20)$$

where $P(x;n,\delta)$ is called the distribution of fiber fragment lengths, δ is the fiber recovery length, and n is equal to N/L. $P(x;n,\delta)$ is the distribution of fragment lengths of a fiber of unique strength σ, length L^* and number of fragments N, and drives all successive fiber fractures. It is a continuous function of x and provides information about the distribution of fragment lengths. This distribution is a direct function of break density and recovery length. An expression for $P(x;n,\delta)$ has been derived by considering this function as the distribution of near-neighbor center-to-center distances of N rods of length δ positioned randomly on a line of length L^*, without overlap [21]. The following are the resulting expressions:

$$P(x;n,\delta) = \frac{2}{n\delta^2}\int_0^{\eta}\psi(\eta')e^{-(x/\delta-1)\psi(\eta')}d\eta', \qquad \delta \le x \le 2\delta \qquad (21)$$

$$P(x;n,\delta) = \frac{1}{n\delta^2}\frac{\psi^2(\eta)}{\psi'(\eta)}e^{-(x/\delta-2)\psi(\eta)}, \qquad 2\delta \le x \qquad (22)$$

where ψ is defined implicitly from

$$\eta = \int_0^{\psi}\exp\left(-2\int_0^{t}\frac{1-e^{-s}}{s}ds\right)dt, \qquad (23)$$

and,

$$\eta = \frac{N\delta}{L}. \tag{24}$$

2.2.5 The Implicit Function $\psi(\eta)$

The function $\psi(\eta)$ was obtained numerically. The quantity η is defined as the dimensionless break density. It is worthwhile to illustrate the fidelity of the numerical approximation used for describing the implicit function $\psi(\eta)$. The numerical approximation was obtained by assigning values to ψ and solving for the corresponding η. Various analytical approximations exist for $\psi(\eta)$, however they are limited to defined ranges of η. It is nevertheless useful to compare the approximation with different analytical forms.

At large fragmentation densities, the available space for adding new breaks (L^*) is greatly reduced. To be more precise it approaches zero while the number of fragments N approaches a finite value; this means that η will reach a finite limiting value. The limit value of η will be referred to as η^*. Curtin showed that L^* may be expressed in terms of the derivative ψ of with respect to η, $\psi'(\eta)$:

$$L^* = N\int_{2\delta}^{\infty}(x-2\delta)P(x;n,\delta)dx = \frac{L}{\psi'(\eta)}. \tag{25}$$

Since L^* goes to zero as η approaches η^* (saturation, therefore no more space available for fracture), then from equation (25) it may be inferred that $\psi'(\eta^*) = \infty$. Consequently, from equation (22) it results that $\psi(\eta^*)=\infty$ and from equation (23) [22]:

$$\eta^* = \int_0^\infty \exp\left(-2\int_0^t \frac{1-e^{-s}}{s} ds\right) dt = 0.7476.... \tag{26}$$

The mean fragment length, L/N, at saturation (η^*) is therefore given by:

$$\bar{x} = \frac{L}{N} = \frac{\delta}{\eta^*} = 1.337\delta \tag{27}$$

This result gives an approximation of the average fragment length at saturation; as may be seen, the average is slightly biased toward the smallest possible fragment length δ. This result has been demonstrated through various simulations [21,22].

For the case of low fragmentation density the following approximate analytical form is accurate to within 1% for $\psi<1$ ($\eta<0.47$):

$$\psi(\eta) = \frac{1}{\left(1-\frac{\eta}{\eta^*}\right)^{\eta^*}} - 1. \tag{28}$$

For the case of large fragmentation density (η approaching η^*) the behavior is well represented by the following:

$$\psi(\eta) = \frac{e^{-2\gamma}}{\eta^* - \eta} \tag{29}$$

where γ=0.577216 is Euler's constant. A direct comparison of the analytical forms with the numerical approximation is illustrated in Figure 2.5.

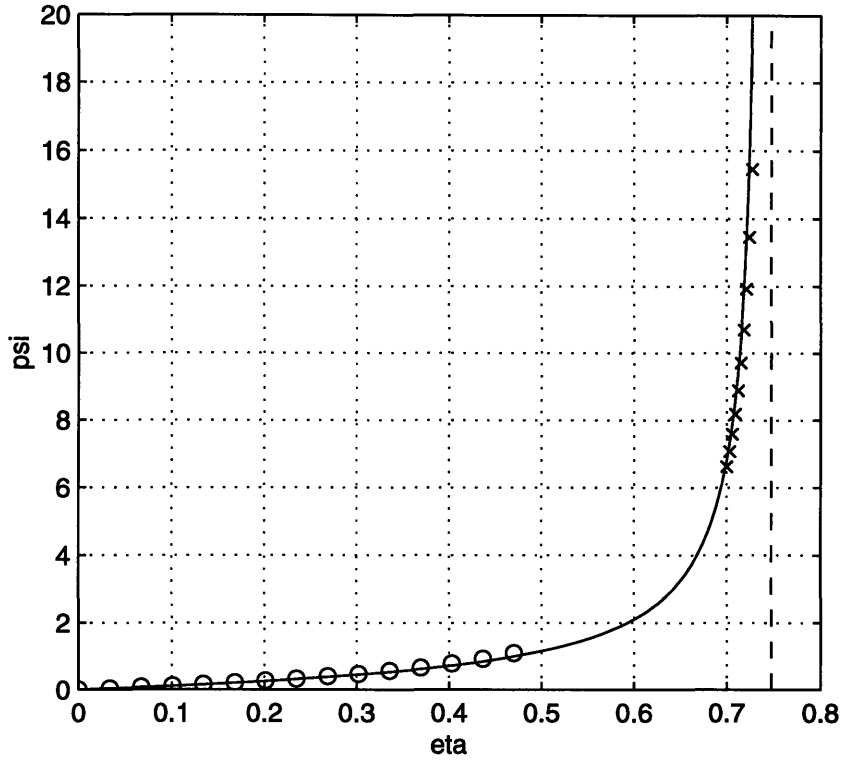

Figure 2.5. A visual representation of the function $\psi(\eta)$ as computed via the implicit integral (continuous line) and with the (o) low- [eq. 28] and (x) high-density [eq. 29] approximations. The vertical dashed line indicates the $\eta^*=0.7476$ asymptote.

2.2.6 A Note on Distribution Functions

Examples of the distribution functions are given in Figure 2.6, where the cumulant of the fragment distribution, F, is used and the quantity log(-log(1-F)) is plotted. The cumulant F may be defined as:

$$F(x;n,\delta) = \int_0^x P(\tilde{x};n,\delta)d\tilde{x}. \qquad (30)$$

As fragmentation progresses, smaller fragments are formed and thus the distribution shifts to the left. It is therefore possible to predict the full evolution

of fiber fragmentation, up to the saturation point. The final solution is obtained numerically with a sequential process. Each step in the process, corresponds to an increase in applied stress. Note that by definition of constant recovery length, the minimum fragment length is δ (this occurs when a crack occurs exactly at the end of a fiber's recovery length). In the example of Figure 2.6, all curves start at a value of -3.824 which is the log of the selected recovery length of 0.15 mm.

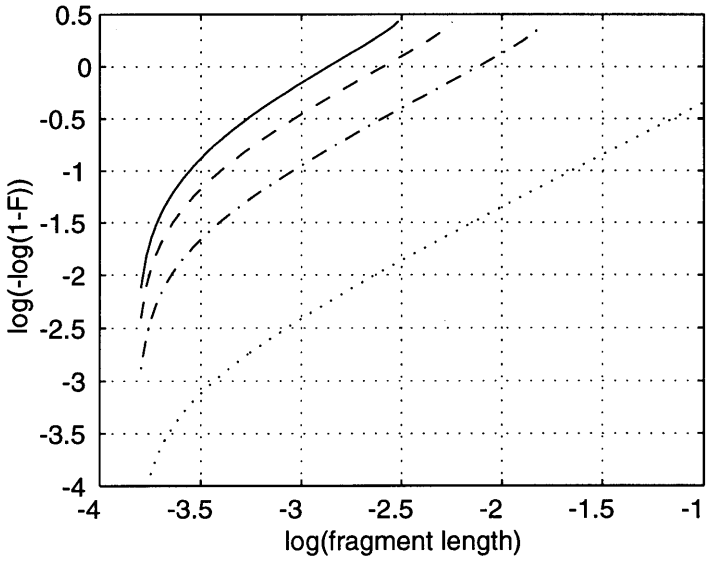

Figure 2.6. Examples of distribution functions for peak strains of (...) 0 με, (-.) 4000 με, (--) 8000 με, and (-) 12000 με. The Weibull plot is in the form log(-log(1-F)) vs log(fragment length) where F is the cumulant of the fragment distribution. Characteristic parameters for this fiber are: δ=0.15 mm, L=0.1 m, L_o=0.025 m, σ_o=56.1 MPa, σ_{res}=1.64 MPa, and ρ=2.2.

2.2.7 Evolution of Fragment Distribution

At the beginning there is one single fragment when no load is applied. As the load is increased, the number of breaks varies according to equation (19). At the same time, a new value for L^* may be determined (this is used in the next

time step to determine the new number of fragments). Using the newly determined break density it is possible to define the new distribution functions. These quantities can then be used to determine material properties before the process is repeated with a new stress value. A typical representation of fragmentation may be given in terms of number of breaks versus strain as illustrated in Figure 2.7. The rate of change in fiber fragmentation is mostly driven by the Weibull modulus. The saturation regime is mostly determined by the fragment recovery length.

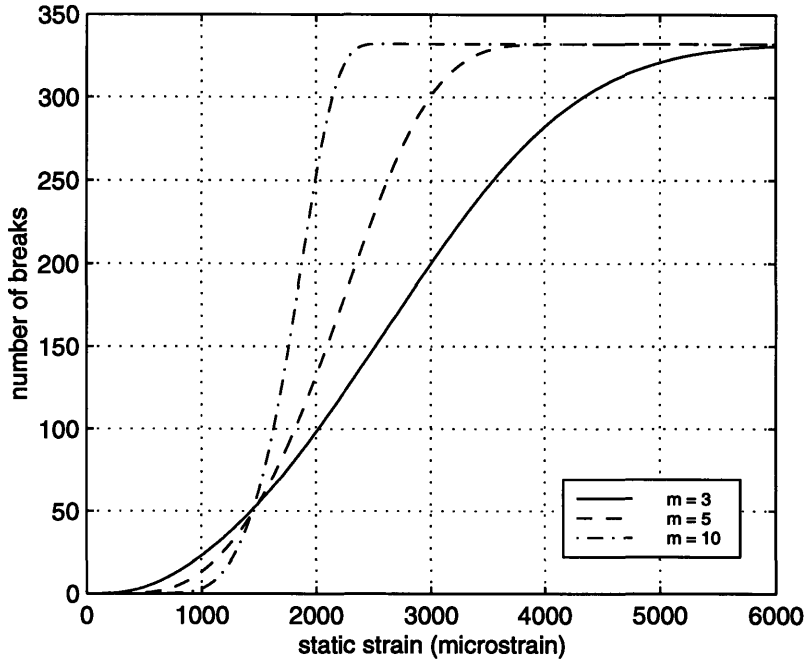

Figure 2.7. Example of break evolution as a function of strain at different Weibull modulus (m) values. Note that equal recovery lengths cause equal saturation regimes. Characteristic parameters for this fiber are: δ=0.15 mm, L=0.1 m, L_o=0.001 m, σ_o=56.1 MPa, and σ_{res}=1.64 MPa.

2.3 Effective Properties

This section concerns the derivation of the effective fragment properties. This is accomplished by analyzing the details of load transfer between the actuation and structural plies through the matrix material, considering both the applied external loads and the induced strain. The matrix material plays a critical role in this process, since it must provide efficient stress transfer among plies. Various models (shear lag) exist for the characterization of stress transfer through a matrix material [14]. A one-dimensional model also exists for the characterization of stress transfer in a system composed of an active plate bonded to a passive structure [19]. This last model provides the foundation for the model employed in this work.

The goal is to characterize the stress transfer from fiber fragments to the neighboring reinforcement. Some preliminary simplifications must be considered. A representative volume element (RVE) may be defined to identify a repetitive section around a single fiber in the actual composite. Consider the transverse line fraction of fibers X_2 defined as

$$X_2 = \frac{N_a d_a}{w_{tot}}, \tag{31}$$

where N_a is the number of fibers in the composite, d_a is the fiber diameter, and w_{tot} is the total active ply width. Note that the subscript 'a' has been used to represent the fiber: it stands for *actuator* which is a more general term for the active element in the active ply. Similarly for the E-glass layer, the subscript 's'

will be used for *structural material*. Then the representative element's width will be

$$w = \frac{d_a}{X_2}. \tag{32}$$

Because of the non-interactive assumption on the fibers, this element is sufficient to represent the composite's behavior. In order to simplify the analysis however, it is important to define an active composite *equivalent* representative volume element (ERVE). This element must capture the elastic properties of the composite's RVE like longitudinal stiffness and shear transfer mechanisms. The length of the ERVE represents the generalized fragment length and varies according to the corresponding distribution of fragment lengths from the previous section.

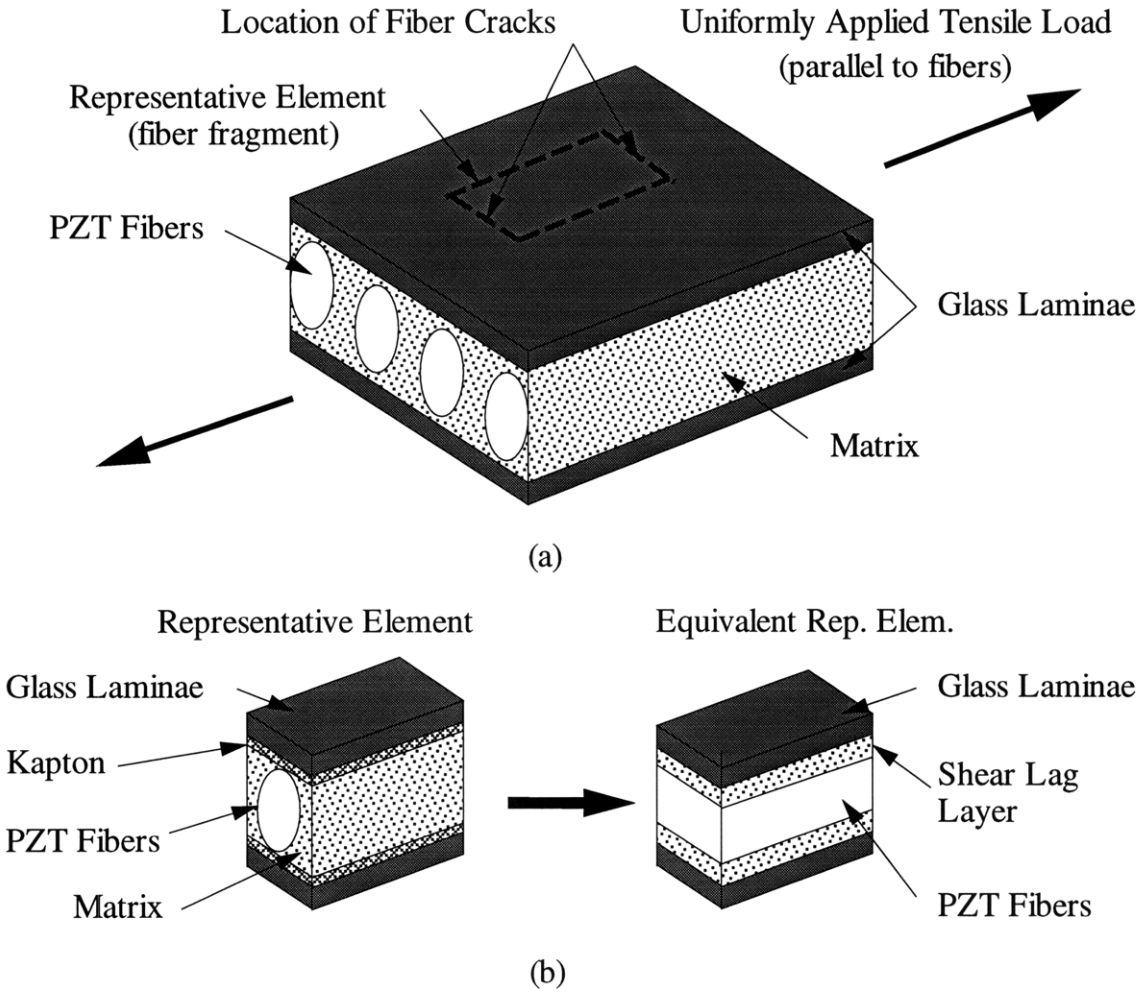

Figure 2.8. (a) Representative volume element for unidirectional active composite material, (b) transformation to equivalent element.

A composite fragment is a section of the composite the length of which is equal to the length of the corresponding active fiber fragment. Figures 2.8a and 2.8b illustrate the qualitative transformations from active composite RVE to equivalent representative element. In these transformations, the actuator and structure cross-sectional areas are maintained constant, based on element width, w. The main dimensions and transformations are illustrated in Figure 2.9.

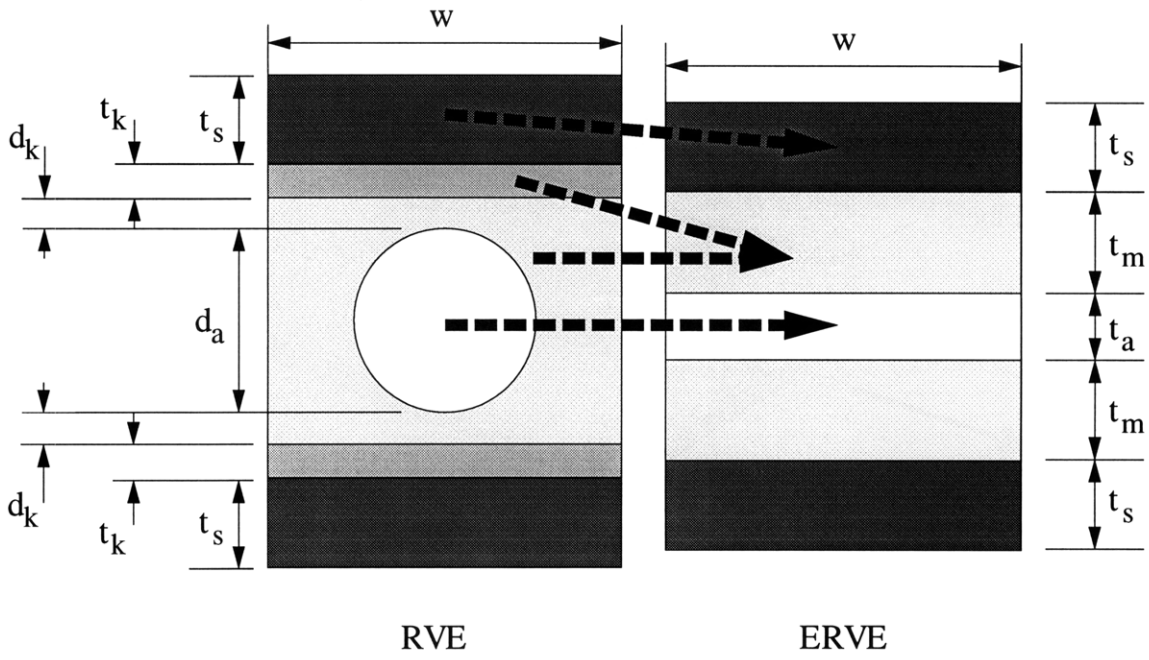

Figure 2.9. Illustration of all representative volume element thicknesses and dimensions.

The matrix and Kapton electrode material are transformed into a single material with equivalent stiffness. The fiber (actuator) area in the RVE is given by

$$A_a = \frac{\pi d_a^2}{4} \tag{33}$$

and in the ERVE by

$$A_a = w t_a \tag{34}$$

where d_a is the fiber diameter, t_a is the equivalent active layer thickness in the ERVE, and w is the element's width. Solving for t_a yields:

$$t_a = \frac{\pi X_2 d_a}{4}. \tag{35}$$

These transformations ensure that equivalent properties are used in the RVE. The matrix layer in the ERVE is obtained by effectively combining the stiffness ratio-scaled (Kapton to matrix, E_k/E_m) Kapton area and the matrix area as they appear in the RVE. Since Kapton and matrix have similar stiffness (2.9 GPa and 5 GPa respectively) it is safe to 'fuse' them into a single layer. Assume the Kapton layer is separated from the top of the fiber by a distance d_k. Then the combined Kapton and matrix area in the RVE are therefore

$$A_m = w(2d_k + 2t_k \frac{E_k}{E_m} + d_a) - \frac{\pi d_a^2}{4} \tag{36}$$

where t_k and E_k are Kapton layer thickness and stiffness respectively, and E_m is the matrix stiffness. Since the matrix area in the ERVE is simply $A_m=2wt_m$, then the matrix thickness, t_m, in the ERVE is:

$$t_m = d_k + t_k \frac{E_k}{E_m} + \frac{d_a}{2} - \frac{\pi d_a^2}{8w}. \tag{37}$$

Manufacturing concerns drive this configuration. Additionally, it must be noted that the composites are manufactured in such a way that the width of the active layer does not extend all the way out to the edges of the structural ply (see Fig 2.10). This passive area counteracts induced actuation therefore it effectively corresponds to a thicker E-glass (passive) ply. This in turn implies that for the same assumed width of actuator and structure, the structure's stiffness must be scaled appropriately. This is accounted for in the E-glass thickness used in the RVE. The actual E-glass layer width is 14 mm whereas the active area width is

only 10.5 mm. This means that the E-glass (structural) layer in the RVE must be inflated' by a factor equal to this width ratio (14/10.5):

$$t_s = t_g \frac{14}{10.5} \tag{38}$$

where t_g is the physical thickness of the E-glass plies and t_s is the scaled thickness of the passive structural ply in all representative volume elements. In this case the similar effect on the matrix is neglected as it provides comparatively smaller stiffness.

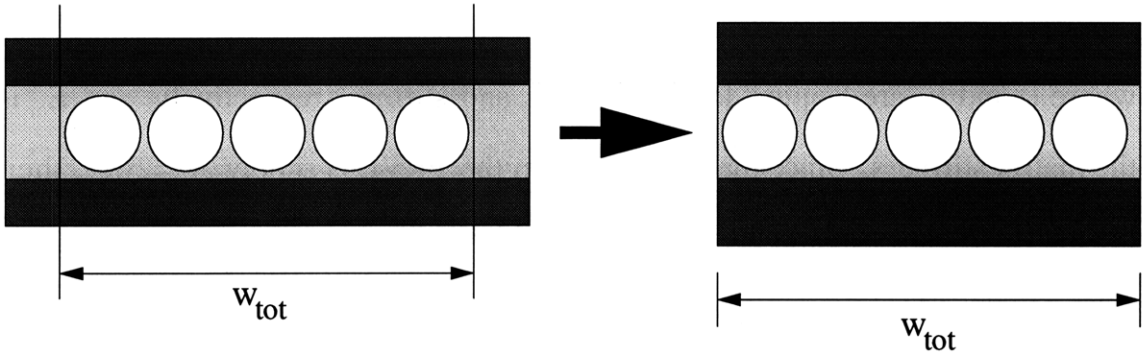

Figure 2.10. Illustration of the width of active and structural layers in a typical composite cross-section. In order to properly represent stiffness it is necessary to scale the structural layer's thickness. Note the drawing is not to scale.

In the model the composite is loaded through the two outer structural glass plies and actuated through the central active lamina. The matrix medium provides the elastic shear transfer between the active and structural plies (or fibers). All this information is introduced as boundary conditions on the representative volume element as illustrated in Figure 2.11.

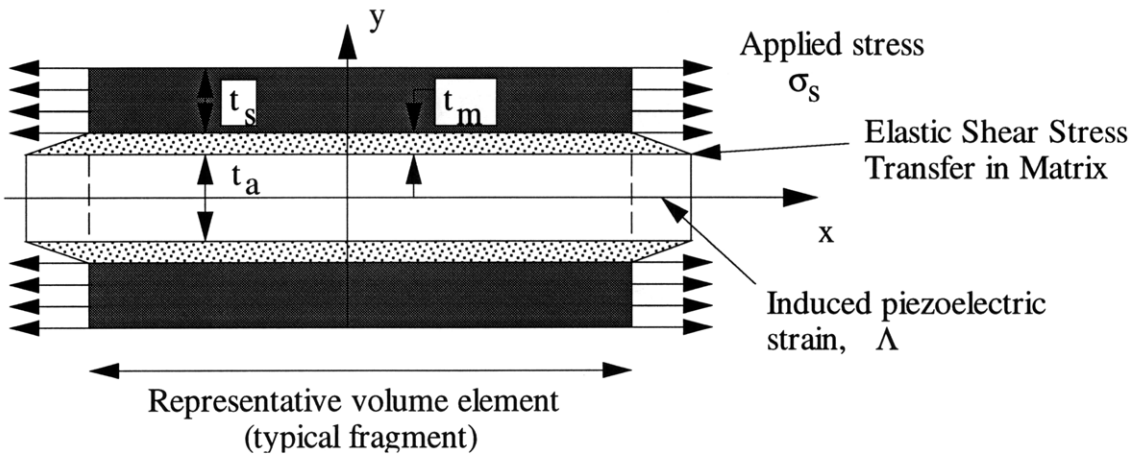

Figure 2.11. Boundary conditions applied to RVE.

Boundary conditions may be considered applied either combined or independently using linearity of the system based on superposition. The overall results may be analyzed in terms of stiffness, by looking at the response of the RVE to loading, or in terms of actuation, by observing the deflections induced by the active fibers on the reinforcing plies. The interactions will be monitored in terms of strains of the active and reinforcing plies. It is important to note that this model does not apply uniquely to the case of fiber composites but it is very general in its structure. *By construction, since the representative volume element is one-dimensional in nature, it is equally applicable to the more general case of active composites constructed from active plates bonded to substrates.*

The basic shear lag equations are derived from equilibrium on free body diagrams of sections of the actuator and structural ply [19]. Consider a section of length dx of 1/4 symmetry simplified representative element as illustrated in Figure 2.12.

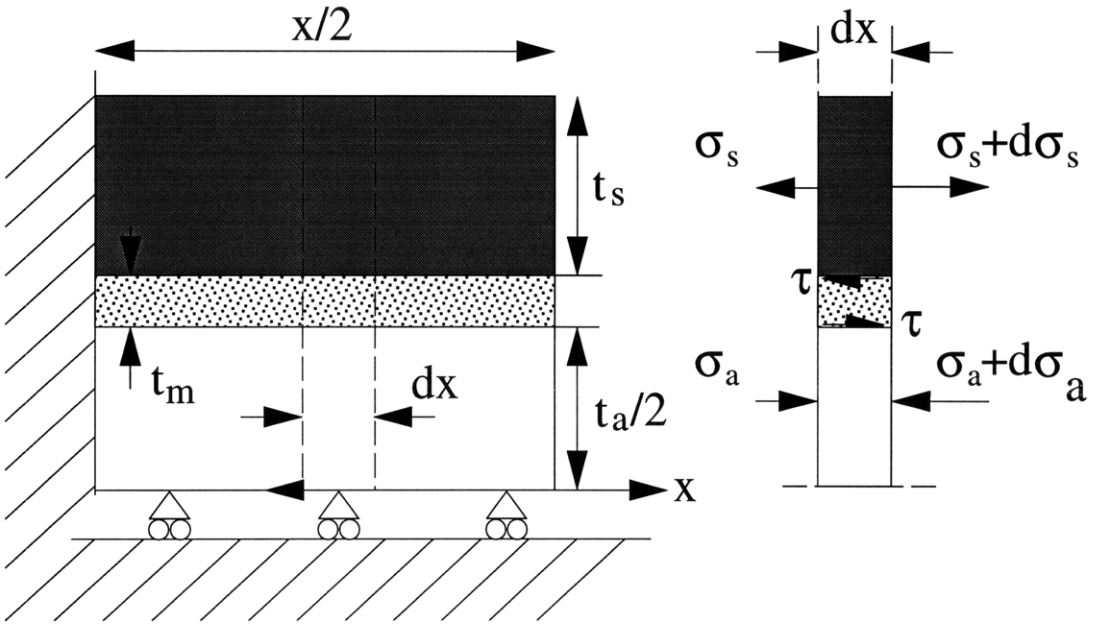

Figure 2.12. Simplified representative volume element.

Then enforcing equilibrium on the actuator and structure respectively gives:

$$d\sigma_a t_a w + 2wdx\tau = 0 \tag{39}$$

$$d\sigma_s t_s w - wdx\tau = 0 \tag{40}$$

where the subscripts a and s refer to actuator and structure. The shear stress τ is given by:

$$\tau = G\frac{u_s - u_a}{t_m}. \tag{41}$$

where G is the matrix shear modulus and u_s and u_a are the structure and actuator displacements respectively. Differentiating equations (39) and (40) yields

$$\frac{d^2\sigma_a}{dx^2}+\frac{2G}{t_a t_m}(\varepsilon_s-\varepsilon_a)=0 \tag{42}$$

$$\frac{d^2\sigma_s}{dx^2}+\frac{G}{t_s t_m}(\varepsilon_s-\varepsilon_a)=0 \tag{43}$$

Recalling that $\sigma_a=E_a\varepsilon_a$ and $\sigma_s=E_s\varepsilon_s$, then solving for ε_s in (42) and for ε_a in (43) gives:

$$\varepsilon_s=\varepsilon_a-\frac{E_a t_a t_m}{2G}\varepsilon_a'' \tag{44}$$

$$\varepsilon_a=\varepsilon_s-\frac{E_s t_s t_m}{G}\varepsilon_s''. \tag{45}$$

Substituting ε_s from (44) for ε_s into (45) yields:

$$\varepsilon_a''+\frac{2E_s t_s}{E_a t_a}\varepsilon_s''=0. \tag{46}$$

Differentiating equations (44) and (45) twice yields:

$$\varepsilon_s''=\varepsilon_a''-\frac{E_a t_a t_m}{2G}\varepsilon_a'''' \tag{47}$$

$$\varepsilon_a''=\varepsilon_s''-\frac{E_s t_s t_m}{G}\varepsilon_s'''' \tag{48}$$

Solving (46) for ε_s, substituting into equation (48) and simplifying gives the following fourth order differential equation:

$$\varepsilon_s'''' - \left(\frac{G}{E_s t_s t_m}\right)\left(\frac{2E_s t_s + E_a t_a}{E_a t_a}\right)\varepsilon_a'' = 0 \tag{49}$$

and similarly for ε_a:

$$\varepsilon_a'''' - \left(\frac{G}{E_s t_s t_m}\right)\left(\frac{2E_s t_s + E_a t_a}{E_a t_a}\right)\varepsilon_s'' = 0. \tag{50}$$

Let

$$\Gamma_o^2 = \left(\frac{G}{E_s t_s t_m}\right)\left(\frac{2E_s t_s + E_a t_a}{E_a t_a}\right) \tag{51}$$

then equations (49) and (50) simplify to the following fourth order differential equations in the strain variables ε_a and ε_s (actuator and structural ply strains respectively):

$$\frac{d^4\varepsilon_s}{dx^4} - \Gamma_o^2 \frac{d^2\varepsilon_s}{dx^2} = 0 \tag{52}$$

$$\frac{d^4\varepsilon_a}{dx^4} - \Gamma_o^2 \frac{d^2\varepsilon_a}{dx^2} = 0. \tag{53}$$

The general form for the solution of these differential equations is

$$\varepsilon_s = B_1 + B_2 x + B_3 \sinh(\Gamma_o x) + B_4 \cosh(\Gamma_o x) \tag{54}$$

$$\varepsilon_a = C_1 + C_2 x + C_3 \sinh(\Gamma_o x) + C_4 \cosh(\Gamma_o x) \tag{55}$$

Substituting equation (54) into (44) gives

$$\begin{aligned} \varepsilon_s &= C_1 + C_2 x + C_3 \sinh(\Gamma_o x) + C_4 \cosh(\Gamma_o x) - \ldots \\ &\ldots - \frac{E_a t_a t_m \Gamma_o^2}{2G}\left[C_3 \sinh(\Gamma_o x) + C_4 \cosh(\Gamma_o x)\right] \end{aligned} \tag{56}$$

then comparing (56) to (54):

$$B_1 = C_1 \;\&\; B_2 = C_2$$

$$B_3 = C_3\left(-\frac{E_a t_a}{2E_s t_s}\right)$$

$$B_4 = C_4\left(-\frac{E_a t_a}{2E_s t_s}\right) \tag{57}$$

Finally, a general expression for the actuator and structure strains is obtained:

$$\varepsilon_a = C_1 + C_2 x + C_3 \sinh(\Gamma_o x) + C_4 \cosh(\Gamma_o x) \tag{58}$$

$$\varepsilon_s = C_1 + C_2 x - \frac{E_a t_a}{2E_s t_s}\left[C_3 \sinh(\Gamma_o x) + C_4 \cosh(\Gamma_o x)\right] \tag{59}$$

Boundary conditions are then applied separately; solutions are obtained by superposition. It is convenient to illustrate the boundary conditions separately: on one hand there is the effect of the constrained active layer, as it is actuated, on the reinforcing plies; on the other there is the effect of the passive reinforcing plies, as they strain under applied loads, on the active layer. The first set is for the case of mechanical load applied through the structural ply:

$$\varepsilon_s(\pm x/2) = \frac{\sigma_s}{E_s} \;\&\; \varepsilon_a(\pm x/2) = 0 \tag{60}$$

The second set is for the case of induced piezoelectric strain in the active lamina:

$$\varepsilon_s(\pm x/2) = 0 \quad \& \quad \varepsilon_a(\pm x/2) = \Lambda. \tag{61}$$

The constants C_i result from the boundary conditions:

$$C_1 = \frac{1}{2E_s t_s + E_a t_a}\left(E_a t_a \Lambda + 2 t_s \sigma_s\right) \tag{62}$$

$$C_2 = C_3 = 0 \tag{63}$$

$$C_4 = \frac{1}{\cosh\left(\frac{\Gamma_o L}{2}\right)}\left(\frac{2E_s t_s}{2E_s t_s + E_a t_a}\right)\left(\Lambda - \frac{\sigma_s}{E_s}\right) \tag{64}$$

Substituting the constants back into equations (58) and (59) gives expressions for the local strains in the composite fragment:

$$\varepsilon_a(x) = \frac{1}{2E_s t_s + E_a t_a}\left[E_a t_a \Lambda + 2t_s\sigma_s + \frac{2E_s t_s\left(\Lambda - \frac{\sigma_s}{E_s}\right)}{\cosh\left(\frac{\Gamma_o L}{2}\right)}\cosh(\Gamma_o x)\right] \quad (65)$$

$$\varepsilon_s(x) = \frac{1}{2E_s t_s + E_a t_a}\left[E_a t_a \Lambda + 2t_s\sigma_s - \frac{E_s t_s\left(\Lambda - \frac{\sigma_s}{E_s}\right)}{\cosh\left(\frac{\Gamma_o L}{2}\right)}\cosh(\Gamma_o x)\right] \quad (66)$$

The overall fragment elongation is then obtained by integrating over the fragment length from -L/2 to L/2:

$$\Delta L_a = \int_{-L/2}^{L/2}\varepsilon_a dx = \frac{1}{2E_s t_s + E_a t_a}\ldots$$
$$\ldots\left[E_a t_a \Lambda L + 2t_s\sigma_s L + \frac{4E_s t_s}{\Gamma_o}\left(\Lambda - \frac{\sigma_s}{E_s}\right)\tanh(\Gamma_o x)\right] \quad (67)$$

$$\Delta L_s = \int_{-L/2}^{L/2}\varepsilon_s dx = \frac{1}{2E_s t_s + E_a t_a}\ldots$$
$$\ldots\left[E_a t_a \Lambda L + 2t_s\sigma_s L - \frac{2E_s t_s}{\Gamma_o}\left(\Lambda - \frac{\sigma_s}{E_s}\right)\tanh(\Gamma_o x)\right] \quad (68)$$

Reducing and simplifying yields the final expressions for the total fragment strains:

$$\frac{\Delta L_s}{L} = \left\{ \frac{2\Psi}{2\Psi+1}\left[1 + \frac{1}{\Psi\overline{\Gamma_o}}\tanh\left(\frac{\overline{\Gamma_o}}{2}\right)\right]\right\}\frac{\sigma_s}{E_s} + \ldots$$
$$\ldots + \left\{ \frac{1}{2\Psi+1}\left[1 - \frac{2}{\overline{\Gamma_o}}\tanh\left(\frac{\overline{\Gamma_o}}{2}\right)\right]\right\}\Lambda \tag{69}$$

$$\frac{\Delta L_a}{L} = \left\{ \frac{2\Psi}{2\Psi+1}\left[1 - \frac{2}{\overline{\Gamma_o}}\tanh\left(\frac{\overline{\Gamma_o}}{2}\right)\right]\right\}\frac{\sigma_s}{E_s} + \ldots$$
$$\ldots + \left\{ \frac{1}{2\Psi+1}\left[1 + \frac{4\Psi}{\overline{\Gamma_o}}\tanh\left(\frac{\overline{\Gamma_o}}{2}\right)\right]\right\}\Lambda \tag{70}$$

where,

$$\overline{\Gamma_o} = \Gamma_o L \tag{71}$$

$$\Psi = \frac{E_s t_s}{E_a t_a}. \tag{72}$$

Equations (69) and (70) determine the effective properties of the two constituent plies of the composite. The results are consistent with expectations about the distribution of strain within each component. The case of induced strain transfer from actuator to structural material is illustrated in Figure 2.13. Here the boundary conditions are no applied mechanical load and an induced strain of 800 με in the actuator. Note that after a certain recovery length, strains are effectively equal in both material systems as expected. Both cases of

constant and continuously varying recovery length are illustrated. The constant recovery length in this case has been selected to be equal to $1/\Gamma_o$. These results are also consistent with the discussion in section 2.2.2 regarding the fiber recovery length. Once again it is clear that some portions of the composite elements are less effective in the stress transfer mechanism. This in turn means that when a composite has a large fiber fragmentation level, the load transfer capability is impaired and reduced mechanical and actuation properties are present. The net effect of this phenomenon is illustrated in the next section.

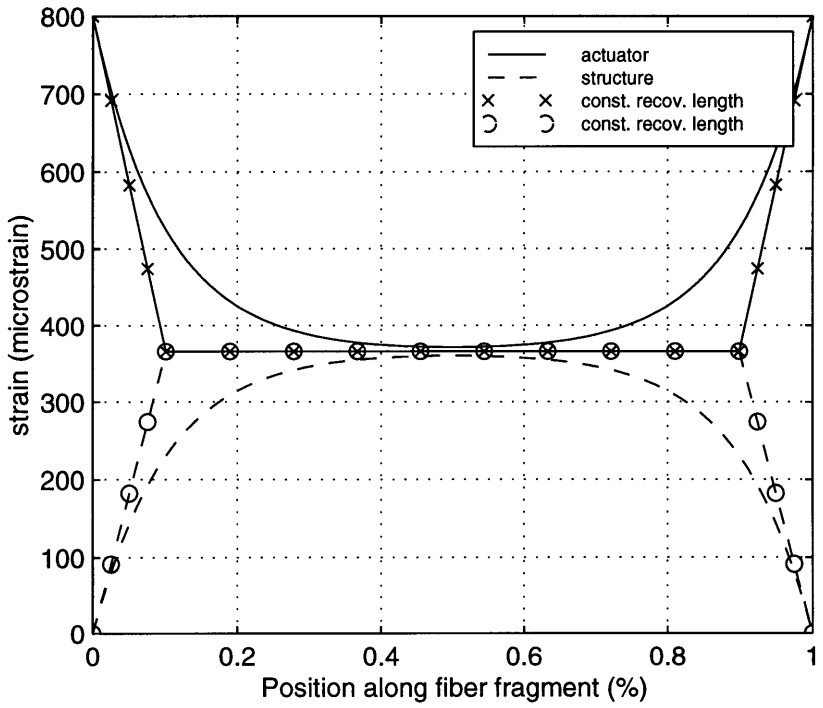

Figure 2.13. Strain distribution in representative volume element under the effect of an 800 με induced strain. The recovery length has been assumed to be equal to $1/\Gamma_o$. This plot refers to an element 0.02 m long, with the following material properties: δ=0.15 mm, ρ=2.2, L_o=0.025 m, σ_o=56 MPa, and σ_{res}=1.64 MPa.

2.4 Effective Composite Properties

This section defines the averaging scheme employed to obtain effective composite properties. At the end of the load cycle, a certain distribution of fragment lengths is present in the composite. Each fragment section obeys equations (69) and (70). The combined effect of all fragment lengths is quantified by averaging the response over the entire fragment distribution to yield the total composite properties. It is therefore possible to obtain an expression for the total composite response by introducing the previously determined fragment distribution and integrating over all possible lengths:

$$\frac{\Delta L_{tot}(\sigma,\Lambda)}{L} = \eta\int_0^\infty \frac{\Delta L_s(x,\sigma,\Lambda)}{\delta} P(x;n,\delta)dx. \qquad (73)$$

This is an important equation of this model, as it unifies and integrates the results of fiber damage statistics with mechanical shear transfer properties. This gives the effective properties sought at the beginning of this work. Unfortunately there is no closed form solution to this problem and a numerical answer must be obtained. Nevertheless it is possible to characterize the composite's response to both applied stress or induced strain. Note that the response of the composite is directly given by the deflection of the supporting structural lamina. The active fiber mechanics are implicitly represented in the composite's response. An example of actuation response predicted by this model is given in Figure 2.14. Here, two curves are shown: one is obtained using the actual fragment distribution as per equation (73), the other is obtained computing an average fragment length at each stress level step and applying the

result to L in equation (69). As may be observed, results are overall similar in nature although asymptotes and specific trends may not necessarily be equal. The model derived in this work is based on using the actual fragment distribution (eq. 73).

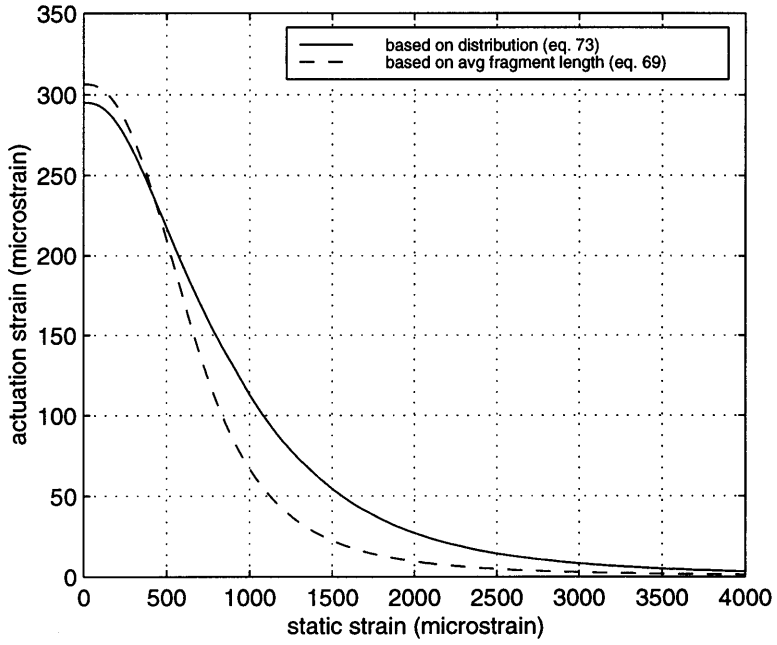

Figure 2.14. Comparison of model actuation results using the (-) actual fragment distribution function and the (–) average fragment length to average material properties. Material parameters are: δ=0.15 mm, ρ=2.2, L=0.1 m, L_o=0.025 m, σ_o=56 MPa, and σ_{res}=1.64 MPa.

2.5 Residual Properties Characterization

In this last modeling section a method to obtain residual material properties will be presented. Once the composite material has been loaded to a certain stress level, damage is permanently introduced. Damage stops accruing when no further load is applied to the composite. However, the active fiber has been cracked and new material properties now characterize the damaged

composite. Broken fibers are present, therefore the load transfer capability within the composite is reduced. It is thus expected that upon reloading, the composite will have diminished stiffness and actuation properties, provided the compressive prestress in the active material is exceeded. If the compressive prestress is still greater than the applied load then the cracks will not open and the material segment will behave as if it were undamaged. This section will provide a methodology to quantify these new material properties. The basic method for the determination of new properties is similar to that employed for the characterization of effective material properties. If the specimen is now loaded up to a strain level which does not exceed the maximum level seen in its loading history, then no further damage is introduced. Furthermore, a single non-varying fragment distribution is present. On the other hand, if the maximum strain level is exceeded, then fragmentation will evolve as discussed in the previous sections.

A model has been developed for the prediction of material properties in strain regimes not exceeding the maximum level previously encountered. The main effect of a fragment distribution already present in the composite is that if an actuator fragment is locally in compression, the fracture gap will be closed. In this case the representative element will effectively behave as if no shear lag was present, i.e. the matrix material has an infinite shear coefficient. This in turn translates into an infinite shear lag parameter, Γ_o. The load will be transferred instantaneously and the composite will locally deform as a uniform material (as if no cracks were present). If the active fiber in the representative element is in tension, then the fracture gap will have opened, thus the composite will perform

with its normal shear lag parameter. Additionally, if the composite is actuated, there might be instances where the gap is opened and some others where the gap is closed by the induced actuation strain Λ.

Typically, as a result of manufacturing and poling, the active ply is subjected to a compressive prestress. Effectively there is a residual prestress locked in the structure which contributes a length change, ΔL_{pre}. Additionally, there is the added effect of the change in fragment length resulting from the combined application of stress and induced piezoelectric strain, $\Delta L(\sigma,\Lambda)$. For both the actuator and the structural ply, the effective element length may be expressed as:

$$L_a = L_{o,a} - \Delta L_{pre,a} + \Delta L_a(\sigma, \Lambda, \Gamma_o) \tag{74}$$

$$L_s = L_{o,s} + \Delta L_{pre,s} + \Delta L_s(\sigma, \Lambda, \Gamma_o) \tag{75}$$

where L_a and L_s are the actual representative volume element lengths of the actuator and the structural ply respectively, and $L_{o,a}$ and $L_{o,s}$ are the initial lengths. L_a and L_s are equal when there are no applied stress and induced strain. The change in length due to the internal prestress may be expressed as:

$$\Delta L_{pre,a} = \frac{F_{pre}}{E_a A_a} L_a \tag{76}$$

$$\Delta L_{pre,s} = \frac{F_{pre}}{E_s A_s} L_s \tag{77}$$

where the prestress, F_{pre}, is:

$$F_{pre} = \left(L_{o,a} - L_{o,s}\right)\left(\frac{1}{\frac{1}{E_s t_s} + \frac{1}{E_a t_a}}\right). \tag{78}$$

In order to compute the actuator stress, the change in actuator length must be computed:

$$\Delta L_{tot,a} = L_a - L_{o,a} = \frac{\sigma_a}{E_a} L + \Lambda L \tag{79}$$

Comparing to equation (74), the following expression for the actuator stress results:

$$\sigma_a = \frac{E_a}{L}\left[-\Delta L_{pre,a} + \Delta L_a(\sigma, \Lambda, \Gamma_o) - \Lambda L\right]. \tag{80}$$

The condition for a crack to be closed is when $\sigma_a<0$, in which case $\Delta L_a(\sigma,\Lambda)$ is computed with an infinite value of Γ_o from equation (74), otherwise its normal value, as computed from the effective properties model section, will be used:

$$\Gamma_o = \begin{cases} \sqrt{\left(\frac{G}{E_s t_s t_m}\right)\left(\frac{2E_s t_s + E_a t_a}{E_a t_a}\right)} & \sigma_a > 0 \\ \infty, & \sigma_a < 0 \end{cases} \tag{81}$$

The response of the composite to actuation will then be reflected in the deflection of the structural lamina as:

$$\Delta L_{tot,s}(\sigma,\Lambda) = N_o \int_0^{\infty} P_o(x;n,\delta)\left\{\int_{-\Lambda_{min}}^{\Lambda_{max}} \frac{d(\Delta L_s(\sigma,\Lambda,\Gamma_o))}{d\Lambda} d\Lambda\right\} dx \qquad (82)$$

where N_o and $P_o(x;n,\delta)$ are the number of breaks and distribution function respectively, corresponding to the furthest damage point, and $d\Delta L_s/d\Lambda$ is derived from equation (69) using the proper value of Γ_o from equation (74):

$$\frac{d\Delta L_s}{d\Lambda} = \left\{\frac{1}{2\Psi+1}\left[1 - \frac{2}{\overline{\Gamma_o}}\tanh\left(\frac{\overline{\Gamma_o}}{2}\right)\right]\right\}. \qquad (83)$$

In order to characterize the residual *stiffness* of the composite a similar approach may be considered. However, all terms with the induced piezoelectric strain, Λ, in equation (80) should be neglected, as stiffness is independent of actuation properties. In the same manner, the final expression for the static elongation may be derived as in equations (73) and (82) with ΔL_s computed, with the proper value of Γ_o, from equation (69):

$$\Delta L_{tot,s}(\sigma) = N_o \int_0^{\infty} P_o(x;n,\delta)\left\{\int_0^{\sigma}\int_{-\Lambda_{min}}^{\Lambda_{max}} \frac{\partial(\Delta L_s(\sigma,\Lambda,\Gamma_o))}{\partial\sigma\partial\Lambda} d\Lambda d\sigma\right\} dx. \qquad (84)$$

Note that the static strain is affected by the induced actuation strain. In this work, however, static strain is obtained from purely mechanical conditions (no induced actuation strain).

Figures 2.15a and 2.15b provide examples of the behavior predicted with this model using realistic, but unoptimized, values for all model parameters.

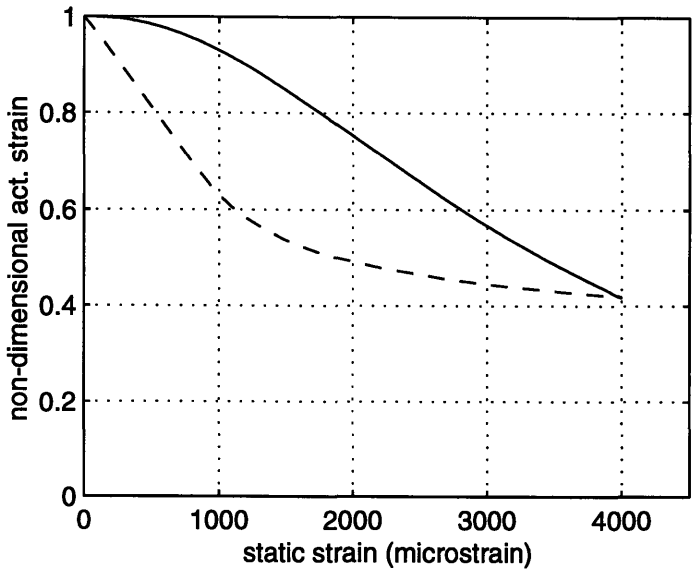

(a)

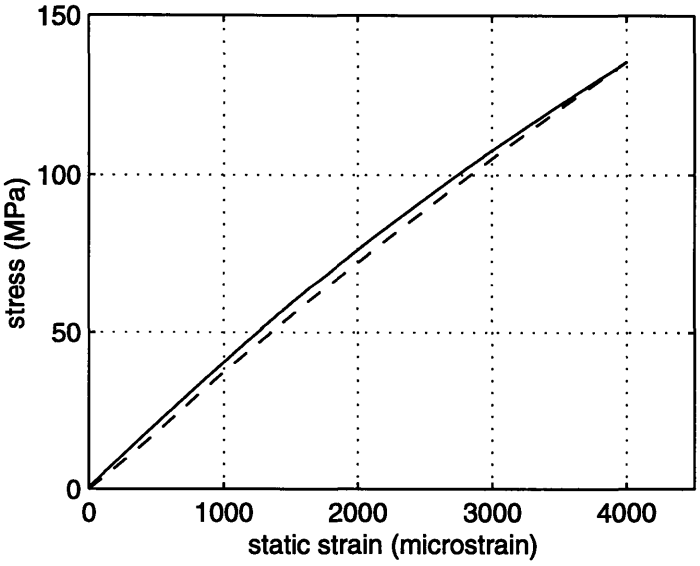

(b)

Figure 2.15. Prediction of (-) first load and (--) residual (a) actuation and (b) stiffness properties for a sample composite loaded to a max first load of 4000 με. Material parameters used for this simulation are: δ=0.15 mm, L=0.1 m, L_o=0.04 m, σ_o=60 MPa, σ_{res}=1 MPa, and ρ=2.55.

2.6 Summary

This chapter presented the theoretical formulation of the model developed for the prediction of actuation and stiffness properties of active composites. The theories of fiber fragmentation and load transfer were used to characterize the fundamental behaviors. In particular it was useful to invoke the load transfer model for an active element bonded to a passive structure: this provided the key link for integrating piezoelectric elements in the host composite structure. A theory was also presented for modeling residual material properties.

Chapter 3

Experimental Program

3.1 Introduction

A large portion of the effort in understanding active composite materials is directed at their experimental characterization. Active composites are relatively new materials and much of the manufacturing techniques are still being developed and improved upon. While initial manufacturing efforts yielded non-uniform and variable results [23], current techniques allow for a more repeatable process with more consistent results. Similarly, testing procedures are now being standardized and provide opportunities to effectively learn about the behavior of active composites. In its current definition, an active composite includes what was previously referred to as an interdigitated electrode piezoelectric fiber composite (IDEPFC). The testing and manufacturing described in this work are an evolution of what is already available in the literature for IDEPFCs [4-10,23].

All the work presented in this chapter builds on the manufacturing and optimization knowledge gained in the development of active composites carried

out in the Active Materials and Structure Laboratory at the Massachusetts Institute of Technology. Specific objectives for this chapter are:

- to provide an understanding of the manufacturing procedure for the active composites used in this study,
- to identify the testing procedures used in the gathering of actuation and stiffness data,
- to discuss and analyze manufacturing-related performance problems, and
- to illustrate the testing program employed for this work.

The experimental program consisted of manufacturing and testing laminated active composites for calibration and validation of the model developed in Chapter 2. The first part of this chapter will explain current manufacturing techniques as well as provide details on the composite configuration and geometry selected for this series of tests. In particular, some of the most significant manufacturing improvements and changes will be discussed. The next part will concern the procedures employed for actuation, stiffness and fragmentation estimation tests. A section will be devoted to discuss current unresolved quality problems in the manufacturing process and their possible effects on composite performance. The last section will also include the test matrix used for the experimental program and describe in details what key data sets will be collected. Overall, a statistically large number of composites were tested in order to provide thorough validation of the modeling effort.

3.2 Test Article Manufacture

All manufacturing work for this program was done in-house at MIT. This section intends to provide a complete description of the baseline manufacturing method employed for this work. Additionally the key manufacturing issues that drive final performance and manufacturing repeatability will be identified. The development process has been the subject of considerable attention over the course of the past three years. One of the most important issues was the convergence to a process which would provide consistent and repeatable results. While some issues still need to be resolved, a general procedure is now available. With this capability it was then possible to further investigate more basic key performance issues.

This is a representation of the most up-to-date manufacturing procedure. This procedure was initially developed at MIT [4]. Significant improvements have since been incorporated. To date, more than 100 composites have been manufactured and considerable testing and characterization has been accomplished. Due to this large number of composites it has been possible to create a consistent statistical pool, useful for overall correlation.

3.2.1 Test Article Geometry

The test articles consisted of interdigitated electrode piezoelectric fiber composite actuators laminated between two 0.005" thick E-glass (0°/90°) fabric plies. This is a symmetric three-ply composite. A standard geometrical configuration was selected to be used during the manufacturing and testing effort and is illustrated in Figure 3.1.

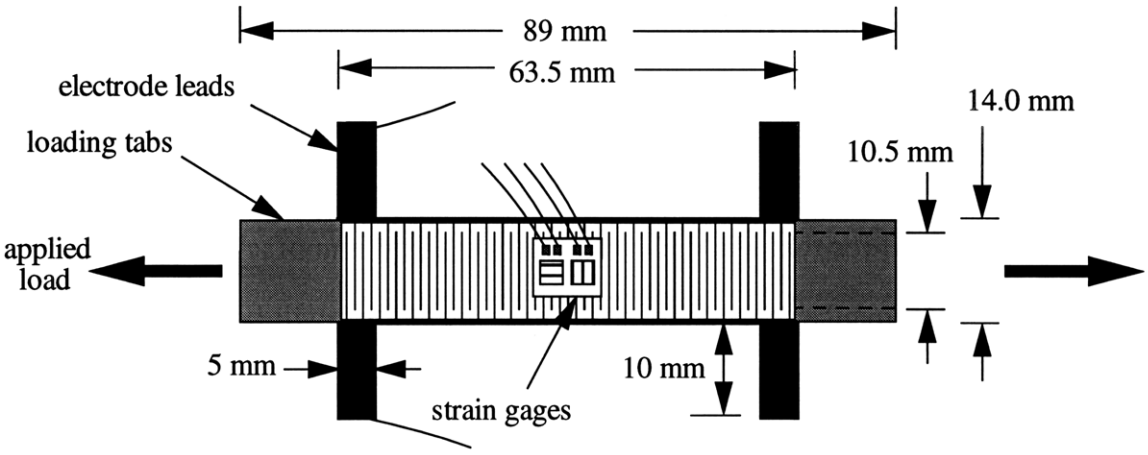

Figure 3.1. Laminated IDEPFC test article ready for actuation tests (includes strain gages and loading tabs).

A rectangular shape was chosen with the following overall dimensions: 89 mm (3.5") long and 14.0 mm (0.55") wide. However the active area covered a smaller region: 63.5 mm (2.5") long and 10.5 mm (0.41") wide. This corresponds to an active area aspect ratio of 5 which nearly conforms to ASTM D3039 standards for tensile specimen testing [24]. The overall larger dimensions provide room in the non-active area for mounting tensile test gripping tabs. One of the constraints leading to this configuration was the active fiber length. Since fiber length cannot be modified, it was decided that the overall composite length be equal to the fiber length (this size was compatible with the maximum manufacturable size of electrodes). The composite's width was then derived accordingly from the specified aspect ratio. The number of fibers that can be fitted in each specimen is limited by the specimen's width and by the line fraction of ceramic to be used. Ideally, the more ceramic the more actuation authority, however it would also lead to fiber packing problems. For all composites used in this work and all other

development work a line fraction of 80% was used. This provides an ideal balance between final performance and manufacturability. Given the selected composite geometry, this translates to 74 fibers per composite.

Manufacture of the test article is accomplished through several steps, and can be broken down into three main stages: (1) manufacture of the active fiber composite (AFC) followed by poling, (2) lamination with E-glass laminae, and (3) preparation for testing, which includes re-poling, applying loading tabs and strain gages. The next sections will provide details for each of the three steps.

3.2.2 Active Ply Manufacturing

This is the most important and time consuming portion of the entire manufacturing process. Some of the steps are critical in terms of their effect on the final electro-mechanical properties. The most significant effects are either breakdown or reduced actuation performance. Part of the efforts in developing the process have been directed at improving these steps. The problem areas are concerned with the presence of *voids*, the quality and type of the *electrodes*, and *compaction*. The effects of these issues will be discussed after the manufacturing process has been outlined. Another critical issue is the quality of the piezoelectric fibers. This problem, however, is not directly controllable as the fibers used are manufactured at an outside company. In brief, the manufacturing consists of laying the bottom electrode onto a cure plate, constructing the necessary mold, laying down the fibers, adding epoxy, degassing (if necessary), and finally setting the top electrode in place. More cure materials are added to protect and seal the materials and then pressure is applied with mechanical

clamps. The composite is then ready to be cured. More details will be provided after a brief description of the materials used. The following is a breakdown of the components used.

- **Aluminum Cure Plate**

  Manufacturing is conducted on an aluminum cure plate designed to fit 4 specimens. This cure plate is also fitted with a vacuum port which provides the capability to apply a vacuum for matrix degassing when necessary. In order to ensure proper alignment of the electrode materials, locator pins (1/8" diameter) have been press-fitted into the plate. A total of four pins are used per composite. A matching top cover has also been manufactured and is used to help distribute the clamping load uniformly over the composites. One of the cure plates (with matching top plate) used is illustrated in Figure 3.2.

Figure 3.2. Cure plate.

- **Electrodes**

A considerable amount of work has been devoted to the development of electrode technologies. This effort included the selection of the proper materials as well as identifying manufacturing techniques. While the selection of the materials was mostly a performance-driven choice, the selection of the ideal production technique was a combination of cost, quality, and ease of manufacturing and strongly depended on the materials selected.

An electrode for use with active composites consists of a conductive pattern on a supporting substrate. The electrode is in the form of an interdigitated pattern designed to maximize the amount of electric field provided to the active fibers while maintaining sufficient distance between fingers to avoid electrical breakdown. The active area (illustrated in Figure 3.3a) is 63.5 mm long and 14.0 mm wide. The side feeder rails extend the length of the active area and have terminal pads at each end. The pattern's main features are 0.19 mm (0.0075 in) wide fingers with a 1.143 mm (0.045 in) center-to-center spacing. These features are illustrated in Figure 3.3b.

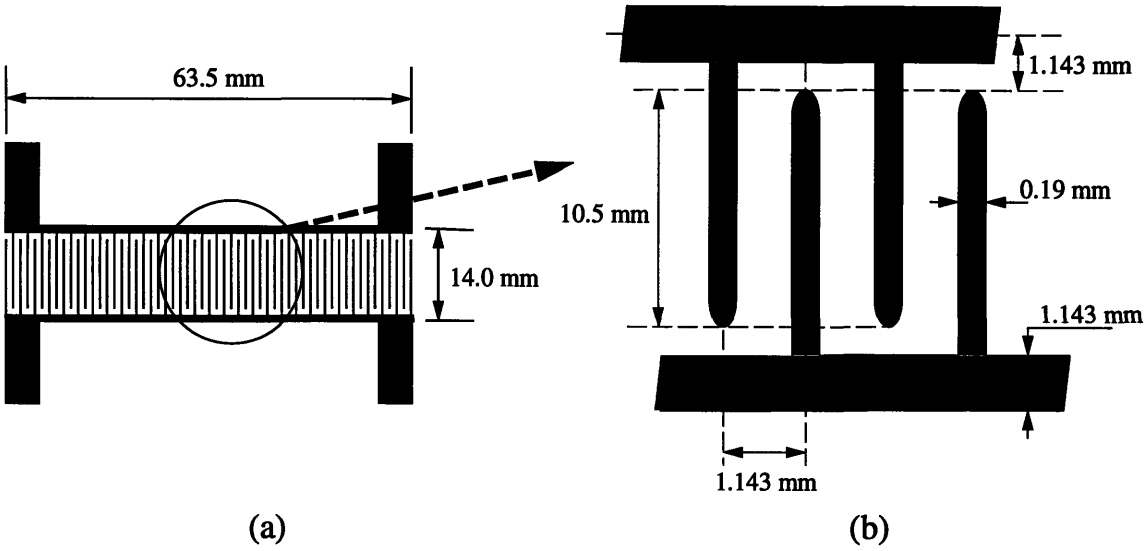

Figure 3.3. Electrode features: (a) overall dimensions, and (b) details of the interdigitated pattern. Drawing not to scale.

Some of the requirements for the substrate material were resistance to high curing temperatures (350 °F), good adhesion to the conductive material, and good mechanical properties (toughness and strength). Because of its excellent high-temperature and mechanical properties, and wide availability, a Kapton polyimide film was selected as the baseline substrate material. The choice for the conductive material was, and still is, a difficult one. The material of choice for all past work and for this series of tests has been, although a few samples have been made with silver-based electrodes. As a matter of fact, copper has been the sole electrode material until recently, when investigations into silver-based polymers and screen printing were undertaken.

Copper-based electrodes were manufactured by means of photolithography, the process used in the manufacturing of computer

chip logic circuits. In this process a 5 mil Kapton substrate with a 2500Å layer of sputtered copper was used. The material was provided by Southwall Technologies. Photolithography has been the technique of choice for manufacturing electrodes for active composite materials. This process allows etching patterns at high resolution and accuracy, leading to very homogeneous patterns. It is, however, a very time consuming and expensive process. Furthermore large area electrodes cannot be printed in-house due to size limitations of the photolithography equipment available. On the other hand, large interdigitated patterns with silver inks onto the same Kapton can be made with screen printing. Silver-based conductive polymers (DuPont CB115) are used in this process. While electrodes are printed with lower accuracy on line features, screen-printing produces a thicker electrode pattern which reaches deeper between the active fibers, resulting in more efficient application of electric field. As an added benefit, production times and cost are greatly reduced. The two manufacturing techniques are illustrated in Figures 3.4a and 3.4b.

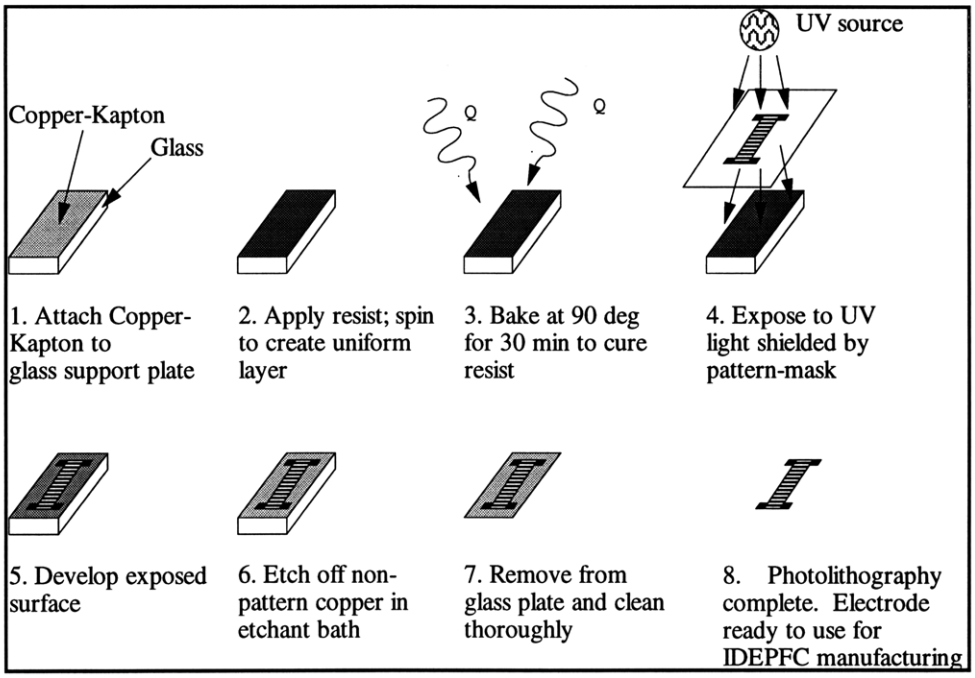

(a)

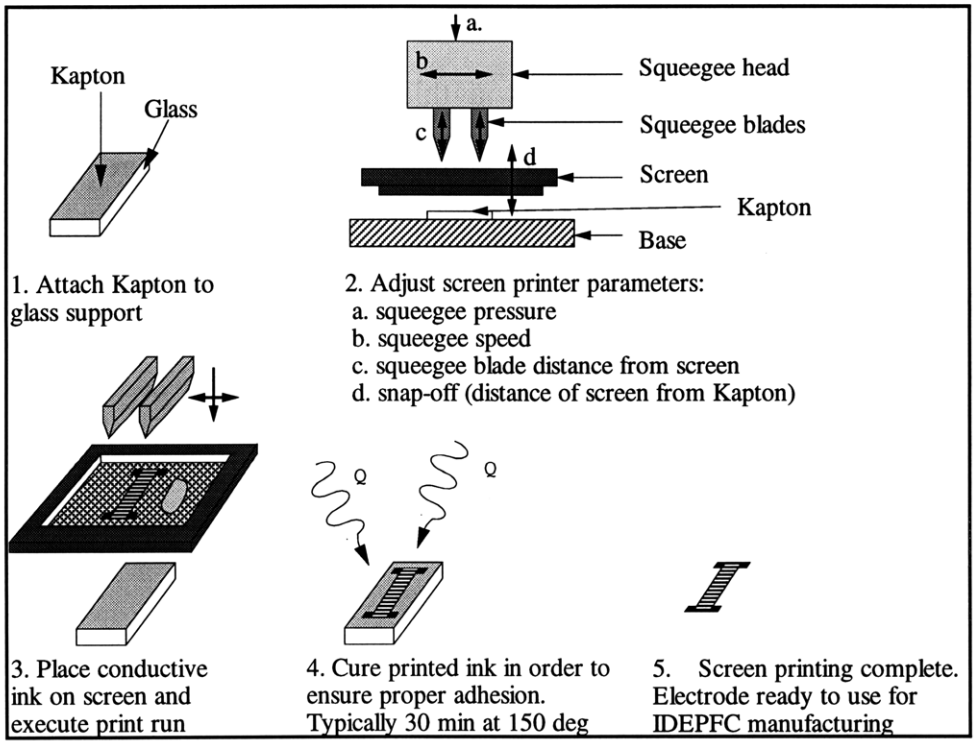

(b)

Figure 3.4. Illustration of (a) photolithography and (b) screen-printing techniques for electrode manufacturing.

- **Fibers**

The piezoelectric fibers used in the active composites are PZT 5H supplied by CeraNova (see Appendix A). They are circular in cross-section, with a diameter of 130 μm. Fibers typically come in lengths of 3.5" or 5". Due to significant variability in fiber characteristics, quality tests were conducted on a few fiber batches. This was done as overall composite performance seemed to be affected by varying fiber properties. While part of the composites in this work have been manufactured with known good quality fibers, most of the composites were manufactured with fibers not subjected to quality tests. This is, perhaps, one of the most uncertain aspects of this whole work as it becomes very difficult to discern when poor performance is attributable to fiber problems or other issues.

- **Matrix Material**

The matrix material used for the wet-layup of the active composites is a Shell Epon 9405/9470 Resin. This is a B-staging two-part epoxy chosen for its prepreg capability: it allows for partial cure, storage (as long as 24 hours), and then co-curing with other plies. This material is a structural bisphenol epoxy used for filament winding, RTM, and prepreg operations. The mixing ratios for parts A and B are 100 to 37 by weight. Air release agent is added (1% weight of epoxy mixture) to reduce the amount of air trapped in the resin. This corresponds to approximately 3 drops for 4 grams of epoxy. Matrix manufactured this way is referred to as "clear" epoxy. Older manufacturing techniques also required the

addition of 60% weight PZT powder dielectric filler (Morgan Matroc PZT 5H powder). This provided an increased material dielectric constant. When PZT powder is used it is also necessary to add (2% weight of PZT filler particles) a surface modifying agent (ICI Americas Hypermer KD-2 Dispersant) to improve the dispersion and wetting of the PZT particles. Matrix prepared with PZT filler is usually referred to as "doped". Part of the composites used in this work were manufactured with doped matrix.

When making doped matrix, PZT filler particles are added after the air release agent. The mixture is typically prepared in a mortar and a preliminary coarse mixing is done with a pestle. This is done to grind the PZT particles to a smaller size while distributing them more uniformly throughout the mixture. A more fine dispersion is achieved by sonicating the mixture for 15 minutes.

- **Supporting Materials**

Supporting materials used in the manufacturing process are sheets of GNPT (Guaranteed Non-Porous Teflon), 0.5 mil thick Kapton tape, 0.25" thick silicone rubber sheets, and aluminum top covers (see Figure 3.5). The silicone rubber and aluminum top covers are cut to the same size of the composite and are used to provide more uniform pressure during cure. All materials are capable of handling the elevated cure temperatures (350 °F).

Lastly, before undertaking the manufacturing process, some preliminary preparations must be completed. The electrodes must be prepared by punching holes in locations corresponding to those of the locator pins on the cure plate. This is done by aligning the top and bottom electrodes on top of each other and placing them simultaneously in a custom made 0.125" punch and die set. Also, the GNPT is cut larger than the electrodes and to fit around the locator pins; one piece per composite. Everything is now ready for manufacturing.

The Manufacturing Process

For simplicity, a step-by-step procedure will be provided to describe the entire manufacturing process. Figure 3.5 provides an overview of the manufacturing process.

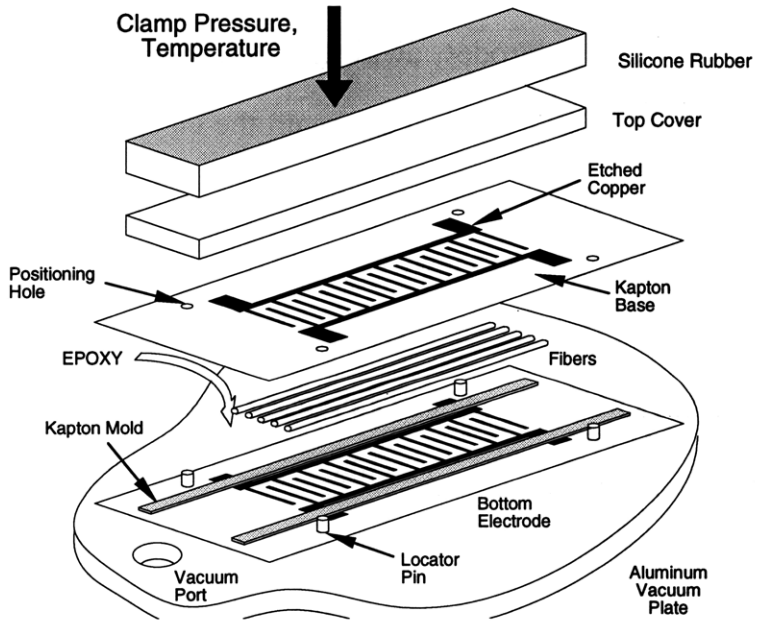

Figure 3.5. Manufacturing process overview.

Step 1. Preparation of the mold. This preliminary work is done to prepare the cure plate for placement of the fibers and subsequent steps. First of all, the cure plate is sprayed with mold release to allow for easy removal of any material in contact with it, in particular epoxy if it were to leak from the molds. It is then allowed to dry for 5-10 minutes. The same is done for the individual top cover plates. GNPT is then cut to fit around the locator pins (and under the electrodes), laid down, and taped all around to secure in place and prevent epoxy from spilling underneath. Particular care is taken to ensure this layer is flat. The bottom electrode is then positioned onto the GNPT over the locator pins. As with the GNPT the electrode is then taped as flat as possible with flash tape. Care is taken to avoid stretching: this could lead to misalignment with the top electrode. If degassing were to be used in successive steps, slits would have to be cut in the bottom electrodes, away from the active area, to provide an escape route for possible air trapped underneath the electrode.

The next step includes preparing the mold. The material used for the mold is Kapton tape. In order to provide sufficient containment, two layers of Kapton tape are used. This layer is slightly thinner than the fiber diameter and allows for sufficient compaction when applying pressure during the cure stage. The tape is then cut into 0.125"-0.25" wide strips. Since the composites will be 3.5" long, the length-wise mold strips are cut 4" long. These strips are placed halfway between the inner edge of the feeder rails and the tip of the opposite polarity fingers; the reason being the need to ensure that fibers are present only in the active area provided by the electrode pattern. Any extra non-active fibers would provide mechanical resistance to actuation. Additionally, the location

where the fibers meet the side molding has typically been a favorable spot for the formation of air voids: if this were too close to the active region, a higher risk of electrical breakdown would be present.

The end strips are then cut to the proper width and placed between the side mold at the location of the fiber ends. Usually a small buffer zone is left between the end of the fibers and the end strip: this allows extra epoxy to collect without spilling over the mold. Finally, the mold is carefully pressed to make sure good adhesion is achieved. The mold is now ready to accommodate the fibers. In the resulting active composite, Kapton surrounds the fibers and matrix material in the form of top and bottom electrode layers and Kapton tape along the edges in the inactive region.

Step 2. Fiber preparation. Each composite contains 74 (seventy four) 3.5" long fibers. This corresponds to a line fraction (X_2) of 80%. The fibers are cut to size and defective ones are rejected. Typically defective fibers have kinks and bends, some are just too short. The fibers are then rinsed with acetone to ensure no deposits, residues, or dirt are transferred to the composite. Any contamination that comes with the fibers could potentially become a weak spot in the final composite. This task is accomplished by placing the 74 fibers for each composite on porous Teflon and then over a wire mesh sitting on top of a glass container. Acetone is then sprayed on the fibers until clean. Drying is done at high temperature (120 °C) for about 15 minutes.

Step 3. Matrix preparation. Concurrent with the fiber preparation is the mixing of the matrix material. A few of the test specimens used in this work had PZT filler particles added to the matrix (composites labeled from AT74 to AT87

in Table 3.1), the remaining specimens used clear epoxy (AT89 through AT120 in Table 3.1). Weighing of matrix ingredients was done on a high precision scale (0.0001g resolution). For the case of clear epoxy, ingredients were added and weighed in the following order: part A, part B, and air release. The procedure is a little more complex for doped epoxy, in which case ingredients are added and weighed as follows: part A, part B, PZT powder, KD-2 dispersant, and air release. However particular care was taken to ensure proper mixing and homogenization of the epoxy. Proper mixing is necessary to ensure thorough breakup of secondary particles in order to obtain a fine low-viscosity mixture. After weighing, the mixture was transferred to a mortar and was thoroughly mixed with a pestle for about 5 minutes. Then it was transferred to a vial and subjected to ultrasonication. With this process, high energy mixing is achieved which enables the further breakdown of the filler particles and more homogenization. It is common procedure to keep the vial in a warm water bath during sonication to prevent boiling of solvents and organic materials in the mixture. This process lasts about 5 minutes. The epoxy is now ready to be used.

Step 4. Placement of fibers in mold. After the fibers have been cleaned, latex gloves are worn for all subsequent steps: this is an extra measure to prevent contamination. The cleaned fibers are then placed onto a piece of GNPT and are slowly pushed in the mold. This is a critical step as it is important not to break any fiber. The fibers are spaced such that the average space between fibers is 20% of the fiber diameter (approximately a 60% total fiber volume fraction) giving an active area about 10.5 mm wide. Once in the mold the fibers are gently rolled around with the tip of the fingers until nicely aligned

and no overlaps are present. This is another key step: overlaps must be avoided as they lead to fiber fracture and increase the final composite thickness. Both effects are detrimental to final performance. Additionally, it is important to check that the fiber ends are within the boundaries of the end mold strips. This step is repeated 4 times for all 4 composites on the plate. The final step is to place the cure plate onto a hot plate; temperature is then raised to about 80 °C. At the same time the mortar containing the epoxy is placed on the cure plate: this keeps the epoxy at the plate temperature and reduces viscosity to values more amenable for use with the fibers in the mold.

Step 5. Adding matrix to fibers in mold. Matrix is added to the mold using a small stick. At first little matrix is added to the fibers; it is applied transversely at three different lengthwise locations from edge to edge. In this stage, capillary forces keep fibers together and allow the matrix to effectively spread in the mold. It is also possible to remove any newly created overlaps by gently rolling the fibers. When the fiber configuration and placement is satisfactory more matrix can be applied with the same procedure from side to side at different locations. Enough matrix should be applied to cover the fibers; too much however would cause the fibers to "float", a situation potentially conducive to overlapping. The fibers are then adjusted one more time with the aid of a flat piece of Teflon. It is now a good time to warm up the cure oven to its intended cure temperature of 350 °F.

Step 6. Degassing (when applicable). In previous manufacturing efforts a degassing stage was used. Some of the composites used in this work were degassed; the majority, however, was not. It is nevertheless worthwhile to

discuss the details of this procedure. With the epoxy mixed with the fibers, a Plexiglas cover is placed on top of the cure plate. This cover is raised on its edges to avoid coming in contact with the composites. Vacuum bag tape is then placed around this cover and vacuum bag tape is sealed on top. Air was evacuated with the aid of a vacuum pump connected to the cure plate. During the degassing stage air voids can be seen surfacing on the matrix and popping. Vacuum is typically applied from 5 to 20 minutes, until no more activity is observed. At the end of the procedure, the bagging, tape, and Plexiglas cover are removed.

Step 7. Applying the top electrode. After matrix material has been added to cover the fibers (and after degassing, if applicable), the top electrode is positioned to complete assembly. This step has been identified as the most conducive to the formation and trapping of voids in the composite. The top electrode is positioned over two of the locator pins (the two pins around one of the mold end strips). The electrode is then slowly rolled onto the fibers while holding the other free end. At the same time slight pressure is applied with a piece of Teflon at the point of contact. Since the piece of Teflon is relatively sharp at the ends, this ensures that only a small area of electrode rolls onto the fibers and pushes air out of the way. If a large area of the electrode were to roll onto the fibers, air could easily be trapped. When all fibers are covered, the remaining two holes are dropped on the corresponding locator pins. At this point it is important to check for voids. Any remaining air can be pushed out using the Teflon strip, along the direction of the fibers. Doing this will also push matrix toward the ends and is collected in the small buffer space left in the mold.

The last step is to tape down and completely seal the top electrode with blue flash tape, therefore preventing possible matrix leakage and holding the top electrode in place.

Step 8. Covering the molds prior to curing. A few more steps are left before curing. First a strip of GNPT is cut to the same width of the composite but slightly longer. It is then placed over the composite and held in place with blue flash tape. The aluminum top cover will be positioned over the GNPT strip (which will prevent the cover from potentially sticking to the top electrode). Blue flash tape is used to secure the top cover in place. The silicone rubber strip is then positioned over the aluminum cover and again secured with blue flash tape. Overall this arrangement will guarantee good compaction for the composite as a result of a more uniformly applied load.

Step 9. Curing. The composites are now ready to be prepared for the last step: curing. The top plate is positioned over the cure plate and four clamps will provide the desired clamping force. Ideally the clamps should be all equal and should be placed at the location of the composites. Clamping pressure is subjective, depending on the types of clamps used. Generally, pressure has been estimated to range between 400 kPa and 700 kPa. As a general rule it should be tightened up to a medium-hard effort. The whole plate should then be put into the now warm over for cure. The required cure time for this type of matrix is three hours. After cure the oven door is opened and the plate is allowed to slowly cool to room temperature.

Step 10. Trimming and preparation. The manufacturing process is not complete until the composites are removed from the cure plate. After removing

the top covers, the composites can be removed from the locator pins. The composites are cut to the proper size, all excess Kapton is trimmed and the tabs are peeled apart. Thickness measurements are taken along the length of the specimen. Target thickness values are around 0.155 mm. After measuring electrode capacitance for top, bottom, and top and bottom together (to ensure no damage has been introduced and consistent values are observed), lead wires are connected. When connecting lead wires the top and bottom tabs are bonded together around the wire lead. Standard strain gage wire is used for this purpose. It must be noted that for copper electrodes the wires are soldered while for silver-based electrodes the wires are bonded with silver paste and then cured for 1 hour at 100 °C. Lastly, capacitance is measured once again and compared with the value measured before connecting the wires: this will give insight into the quality of the wire connection. The trimmed composite is illustrated in Figure 3.6.

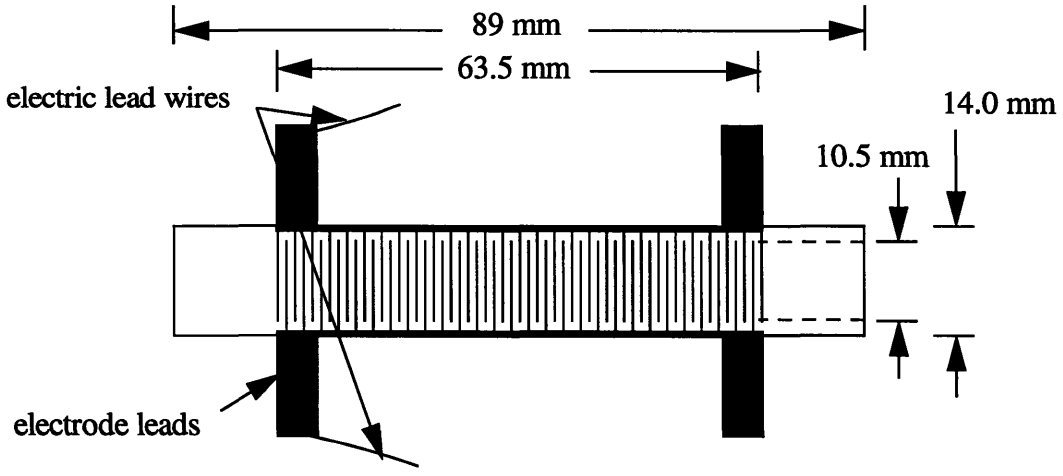

Figure 3.6. Illustration of composite after curing and trimming. This composite is not yet laminated.

As it is, the composite is now ready for the first series of tests.

3.2.3 Poling and Strain Measurements

The first series of tests is aimed at providing indicators of the composite's actuation performance. To this end, the composite is first poled at twice (or more) the coercive field level (in this case 2000V), at 60 °C, and in silicone oil, for 20 minutes. The oil bath is set in a Neslab EX-250HT high temperature bath and poling voltage is provided by a Model 664 Trek amplifier. Following poling, each actuator is aged for at least 24 hours prior to electromechanical testing. After the aging period, the composite's actuation strain is measured. A custom test setup has been arranged for measuring actuation strain. It is based on a laser interferometry system (ZYGO Axiom 2/20 laser set at a resolution of 32.76 μm/V and Keyence LB11/70 laser sensors) which has proven to be very accurate for the task. The composite is placed into the setup, clamped at one end and with a retro-reflector clamped to the free end. Actuation is achieved by subjecting the composite to a standard representative cycle, described in the next paragraph.

The Standard Representative Cycle

This is the standard electrical cycle used to actuate the composites to measure actuation strain and other piezoelectric properties. It consists of setting a DC and AC voltage level for actuation. The values are selected based on 2 limiting factors. First, a practical upper limit exists as composites tend to experience breakdown at large voltage levels. This upper limit has been of particular concern in this work since composites have been easily prone to

electrical breakdown. Second, a lower limit is necessary to avoid exceeding the negative coercive field, which would cause depoling. In the end the selected representative cycle was: V_{DC}=600V, V_{AC}=3000V_{pp}. This corresponds to an applied upper and lower limit of 2100V and -900V respectively. Electrical loads were applied with a Trek Model 664 high voltage amplifier. The typical response of an active composite to the representative work cycle is illustrated in Figure 3.7.

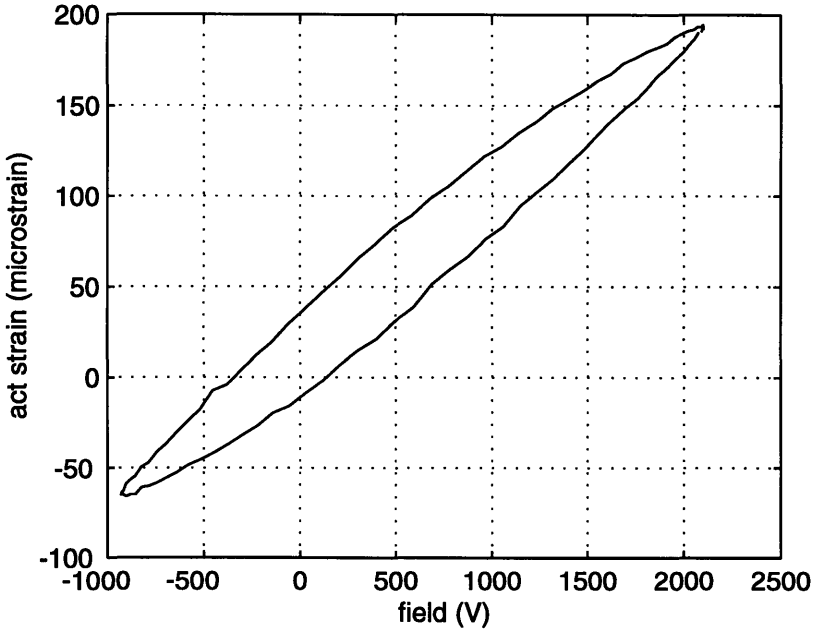

Figure 3.7. Representative work cycle response of an active composite.

3.2.4 Lamination with E-glass Plies

The manufacture of the laminate configuration follows poling and testing for electromechanical coupling of the baseline actuator. Two E-glass prepreg plies (Hexcel E120/F155 Fabric) are cut and a $[0_s°/0_a°/0_s°]_T$ laminate stack is prepared (where "a" and "s" represent the actuator and structural plies

respectively); the center ply is the PFC actuator. The laminates are then cured at 125°C for 90 minutes with an applied pressure between 300 kPa and 400 kPa. Figure 3.8 shows a cross-section of a laminated test article: the fibers, matrix, Kapton, and E-glass layer are clearly visible.

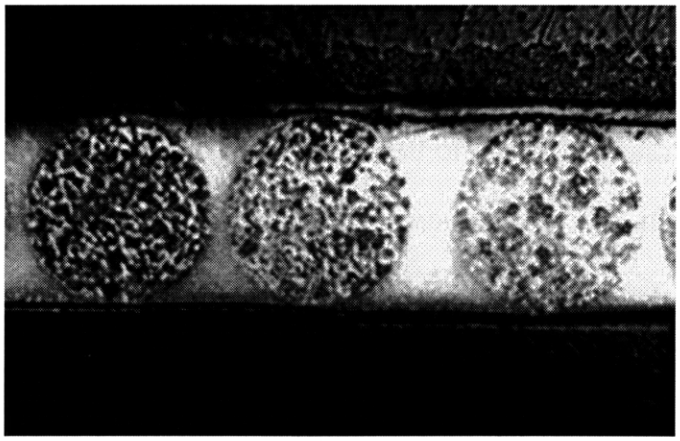

Figure 3.8. Cross-section photomicrograph of laminated composite (160x).

3.2.5 Further Preparation for Testing

One of the effects of lamination was thermal depolarization. This phenomenon is caused by the thermal compressive strains introduced in the soft active fibers which reduce the dipole alignment generated by poling. Ultimately, the compressive stresses inhibit the full polarization of the soft PZT 5H fibers. For this reason the completed actuators are then re-poled at the same (or higher) field level used in the preliminary poling, now at 65°C, for 20 minutes. After re-poling, tests indicated that performance improvements ranged from a 5% to 15% increase in laminated actuation strain. It is now common procedure to re-pole after lamination. Following poling, each actuator is aged again for at least 24 hours prior to further electromechanical testing.

The composite then needs to be prepared in order to be properly used in its intended testing environment. The envisioned tests call for uniaxial tensile loading. For this reason loading tabs are mounted at the ends of the composite to provide a proper gripping surface, therefore limiting interference with the stress generated in the active gage area. The active gage length corresponds to the central 2.5" of the composites. Tabs are sized and bonded according to the same ASTM standards referred to for specimen sizing [24]. A strain gage is then mounted in the middle of the active area: this is the only effective means for measuring strain while under load as it is not possible to fit the laser system to the INSTRON 8501 test machine (the laser system is confined to use on an optical bench). The final test article configuration was illustrated in Figure 3.1. The composite is now ready to be subjected to the full series of tests with the aid of the INSTRON 8501 test machine.

3.2.6 Composites Manufactured

The composites used for this work come from different manufacturing sessions. A first set was prepared during the period from 11/96 to 2/97 (AT74-AT87). The second set was prepared in 4/97 (AT89-AT120). Table 3.1 summarizes the composite properties and corresponding manufacturing highlights.

Table 3.1. Summary of manufacturing process and composite properties. The two sets are separated by the double line. Fiber quality is based on available quality tests; R.C. and Lam.R.C strain refer to representative cycle strains for non-laminated and laminated composites respectively.

Test Article	Fiber Quality	Avg. Thick. (mm)	Elect. Mat.l	Degas.	Doped Matrix	Prepole C (nF)	RC Strain (με)	Lam.RC Strain (με)	Total Repairs
AT74	N/A	0.152	copper	yes	yes	519	810	330	0
AT75	N/A	0.155	copper	yes	yes	484	900	310	0
AT76	N/A	0.157	copper	yes	yes	535	980	340	0
AT77	N/A	0.154	copper	yes	yes	573	900	350	0
AT78	Average	0.203	silver	yes	yes	572	1000	400	0
AT79	Average	0.166	silver	yes	yes	589	1000	300	0
AT80	Average	0.244	silver	yes	yes	449	1100	450	0
AT81	Average	0.223	silver	yes	yes	481	1100	400	0
AT84	Average	0.155	copper	yes	yes	417	800	275	0
AT86	Average	0.158	copper	yes	yes	395	800	300	0
AT87	Average	0.155	copper	yes	yes	452	800	375	0
AT89	Average	0.155	copper	no	no	469	500	180	0
AT90	Average	0.155	copper	no	no	472	850	270	2
AT91	Average	0.153	copper	no	no	462	900	N/A	2
AT92	Average	0.172	copper	no	no	447	860	300	2
AT93	Average	0.156	copper	no	no	431	780	375	5
AT94	Average	0.161	copper	no	no	472	800	310	2
AT95	N/A	0.163	copper	no	no	307	750	275	5
AT96	N/A	0.166	copper	no	no	397	970	350	5
AT97	N/A	0.162	copper	no	no	377	840	360	5
AT98	N/A	0.160	copper	no	no	364	880	330	1
AT99	N/A	0.162	copper	no	no	373	900	330	1
AT100	N/A	0.161	copper	no	no	379	900	350	1
AT101	N/A	0.158	copper	no	no	370	620	200	2
AT102	N/A	0.163	copper	no	no	397	740	250	5
AT103	N/A	0.167	copper	no	no	377	850	320	3
AT104	N/A	0.162	copper	no	no	431	730	235	4
AT105	N/A	0.163	copper	no	no	399	480	230	5
AT106	N/A	0.162	copper	no	no	407	670	240	4
AT107	N/A	0.162	copper	no	no	475	700	335	4
AT108	N/A	0.162	copper	no	no	431	720	375	3
AT109	N/A	0.161	copper	no	no	455	800	390	1
AT110	N/A	0.162	copper	no	no	464	880	380	2
AT111	N/A	0.162	copper	no	no	464	890	390	2
AT112	N/A	0.163	copper	no	no	444	800	450	4
AT113	N/A	0.159	copper	no	no	279	380	170	1
AT114	N/A	0.163	copper	no	no	401	660	300	3
AT115	N/A	0.160	copper	no	no	224	250	120	1
AT116	N/A	0.162	copper	no	no	236	310	N/A	3
AT117	N/A	0.163	copper	no	no	420	730	360	7
AT118	N/A	0.162	copper	no	no	371	680	255	2
AT119	N/A	0.156	copper	no	no	197	220	N/A	2
AT120	N/A	0.159	copper	no	no	275	410	200	4

3.2.7 Typical Material Problems

It is immediately evident from Table 3.1 that the first set of composites (AT74-AT87) displays better actuation strains, both laminated and non-laminated. Testing for the latest series of composites (AT89-AT120) was a difficult process and results varied considerably as illustrated in Table 3.1. The most critical problems were related to varying properties and susceptibility to electrical breakdown. Within the latest batches manufactured (AT89-AT120), the magnitudes of actuation strains were very inconsistent (see Table 3.1). For the non-laminated (non-clamped) composites from AT89 to AT120, the average strain was 702 με with a standard deviation of 204. Normally, "good" composites have non-clamped free actuation strains in the range of 900 με or greater. For the laminated composites the average strain was 302 με with a standard deviation of 79. Overall, composites ranging from AT74 to AT87 have better performance and quality (see Table 3.2).

Table 3.2. Summary of statistical parameters for composite sets.

Composite Range	AT74-AT87	AT89-AT120
Free Actuation Strain		
Average	908	702
Standard Dev.	129	204
Laminated Actuation Strain		
Average	348	302
Standard Dev.	53	79

A considerable amount of repairs had to be performed in order to provide working laminated composites for testing. All repairs concerned breakdown problems. In general the second set of composites could not handle the representative cycle voltages. Flaws could often be identified as void related for some composites, although some otherwise "perfect" specimens experienced

breakdown. It is this consistent breakdown problem that makes any explanation difficult. In an attempt to identify the source of performance and breakdown problems, potential candidates were identified: (1) *void content*, (2) *electrode pattern alignment*, (3) *compaction*, and (4) *fiber quality*. Following is a brief discussion of these issues.

Voids are regions of air trapped in the matrix where electric field concentrations are created. Small voids typically do not present any problems whereas large voids, particularly those which span across two or more fingers, are most likely to cause dielectric breakdown. Voids are originated either during matrix preparation or during manufacturing. When the matrix is being prepared and mixed, air can become trapped in the form of bubbles. The air release agent added to the matrix minimizes this phenomenon. These voids have been determined to have little or no effect on final performance. A more critical type of void is generated during manufacturing when the top electrode is placed onto the fibers in the matrix. Potentially large air voids can be trapped this way. These are the voids most responsible for dielectric breakdown. Originally curing under vacuum was envisioned as a solution for minimizing the presence of voids in the matrix. However, it was observed that it was mostly successful only at removing voids near the edges of the mold. The inner part of the composite would still be populated with voids, trapped underneath the top electrode. As a matter of fact, small voids would grow in size due to the vacuum, thus creating a configuration more conducive to breakdown. This problem will hopefully be removed with new vacuum-electroding techniques (currently under investigation). Additional sources of potential breakdown are intermittent

porosity in the fibers, air or moisture at the fiber/matrix interface, or contaminants in the matrix or on the fiber surface [10]. These flaws, including voids, provide a path of lowered resistance conducive to breakdown. Electrical damage is characterized by carbonized epoxy which acts as an electrical short. Typically damage initiates as a carbonized line between two electrode fingers of opposing polarity and then develops on a path leading away from the original breakdown site. Examples of observed breakdown patterns are illustrated in Figure 3.9. Site A represent one of the most often observed failures as air is usually trapped near the edge of the side mold during the application of the matrix.

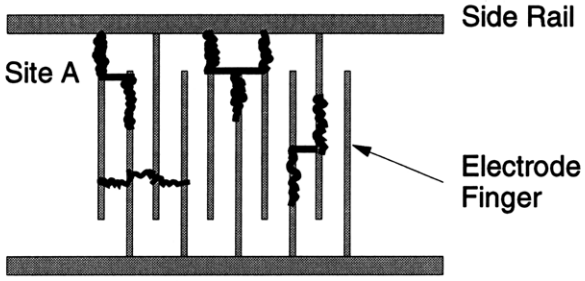

Figure 3.9. Typical damage sites and damage characteristics for dielectric breakdown in baseline actuators.

Electrode pattern alignment is important when it is desired to obtain good performance from active composites. If the electrode features are not properly aligned, significant changes in the electric field path lines will result and actuation performance will drop. The locator pins on the cure plate are used for the purpose of ensuring the best possible alignment. However, misalignment may still occur during the punching of the alignment holes in the electrodes or by stretching the lower electrode while taping it to the cure plate in the manufacturing preparation stage.

Compaction directly affects composite actuation: a higher fiber thickness fraction will result in increased actuation performance [10]. As a result, compaction will mostly depend on variability in the fiber diameter if the same number of fibers are used. Compaction will also be affected when PZT filler particles are used. In this work, mostly clear matrix is used therefore compaction issues were not a factor.

Fiber quality, on the other hand, is probably one of the most significant factors affecting composite quality. Unfortunately, it is also one factor that cannot be directly addressed as fibers are provided by an outside company. Fiber problems have been a constant throughout the development stages of active composites. Porosity issues have been the most serious impediment toward achieving consistent fiber quality, and unfortunately, manufacturing must continue with what is currently available. In general less porosity (increased densification) implies increased piezoelectric performance [10]. Similarly, larger grain sizes translate into higher actuation strains. From studies and tests on single PZT 5H fibers it was observed that considerable variability in fiber properties is possible [10]. In these studies, when taking fibers from a single batch, actuation strains at 20kV/cm varied from 70 $\mu\varepsilon$ for one fiber to 1100 $\mu\varepsilon$ for another one. This provides some explanation for the variability in observed actuation performance. It must be noted that existing fiber manufacturing techniques are currently improving, and future attempts will eventually see more unifrom fiber quality.

3.3 Testing Procedures

3.3.1 Introduction

The basic test in this experimental work consisted of actuation under load of laminated composites (active performance tests) [15]. An INSTRON 8501 series test machine was used for all mechanical tests. Previous testing efforts were performed with a custom test apparatus, with grips manufactured in-house and gravitational loads applied. While this provided all necessary data, the overall quality could be improved. Uncertainties in applied gravitational load levels, and the inability to ensure the test article was subjected exclusively to in-plane longitudinal deflections provided motivation for switching to a dedicated test system. This INSTRON machine was fitted with pneumatic grips and a dedicated control system which enabled thorough control over all test parameters providing a standard testing environment. Strain gages were used for strain measurements.

3.3.2 Baseline Tests

The baseline actuation under load test was aimed at characterizing the actuation authority of active composites when subjected to large tensile loads. The overall test structure is illustrated in Figure 3.10.

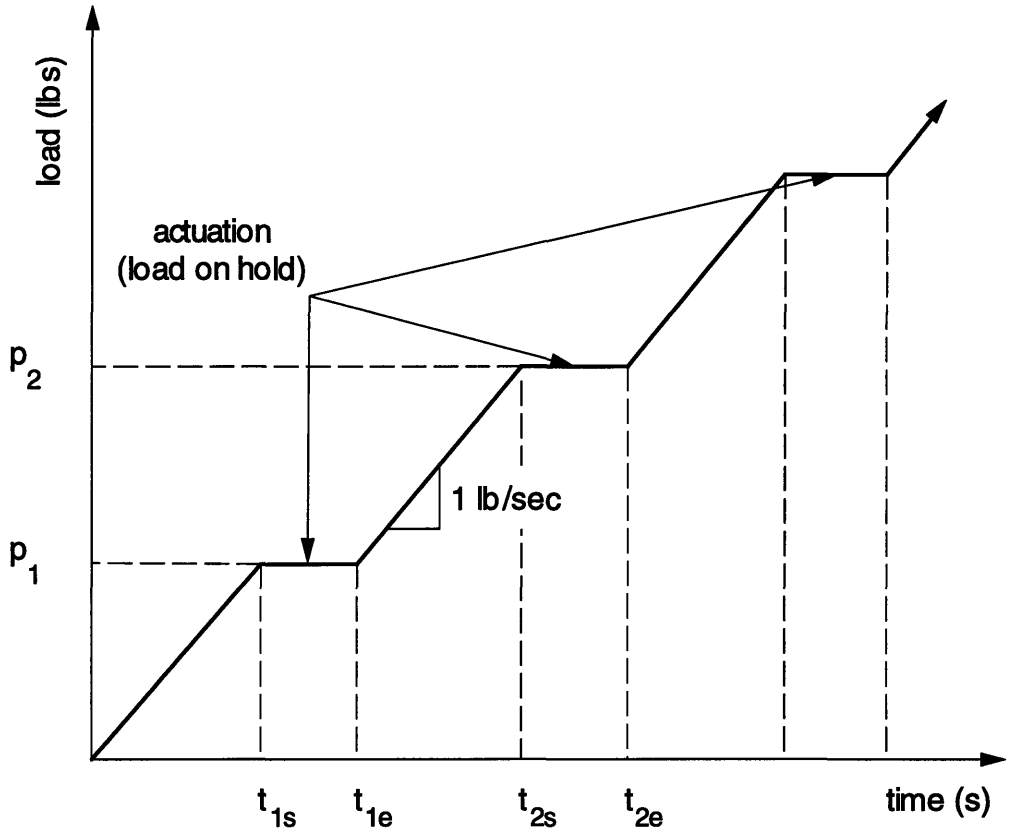

Figure 3.10. Illustration of the actuation under load test. The loads p1 and p2 correspond to the composite strain of interest. The corresponding actuation test (s) start and (e) end times are also illustrated.

The test consists of first loading the composite, at a fixed ramp loading rate of 1 lb/sec, to a predetermined load p_1 as in Figure 3.10. As load p_1 is reached and maintained (time t_{1s}), the actuation test starts: the composite is then actuated with a standard representative cycle (as discussed in section 3.2.2), and data is collected. In this case, load and strain gage data are acquired with a computerized data acquisition system. The strain gage output indicates the total composite strain. Actuation strain levels are extracted by taking the difference between maximum and minimum recorded strains while actuating. For simplicity the static strain level (total composite strain) may be estimated by averaging the

two strain values corresponding to the 0V field levels. An example of actuation under load data is provided in Figure 3.11 for a specimen at a load of about 25 lbs. In this case the actuation strain is about 300 με, and the static strain is about 920 με. When the actuation test is complete (time t_{1e}), loading resumes to the next larger strain level, here shown as point p_2. The test is then repeated until a target *peak strain* is reached. The test peak strain is monitored with the strain gage output: the application of load is manually halted when this strain is reached. After actuation at the peak strain, the composite is then unloaded. Throughout this work, actuation measurements were collected at 10 lbs (or 15 lbs) load increments up to the load corresponding to the peak strain. For a composite never before strained mechanically, this test represents the process of *accumulation of damage*, and the direct manifestation of this phenomenon will be in the magnitude of the actuation strain as loads are increased. The accumulated damage will depend on the peak strain the composite was exposed to. The higher the peak strain, the more the accumulated damage (manifested as reduced actuation strain).

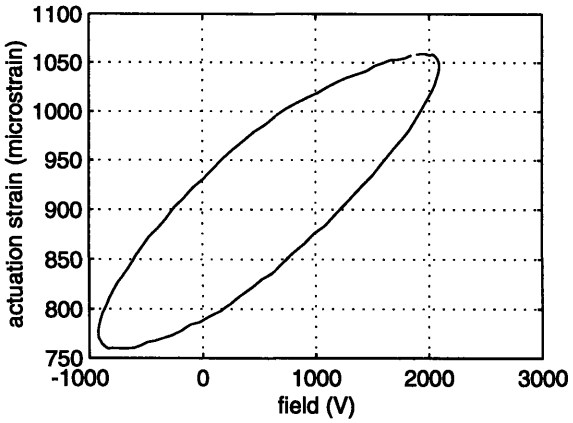

Figure 3.11. Actuation strain vs. applied voltage for composite AT98 at a load of about 25 lbs.

Some composites were subjected to this test twice consecutively. The purpose for this repetition was to illustrate the effect of the *accumulated* damage (corresponding to the proper peak strain loading) on the now *residual* actuation properties when running the test a second time. No further damage should accumulate in the composite during the repeated test since the peak strain of the first test is not exceeded. This provides invaluable insight into the feasibility of using active composites in structures which see the application of large repetitive loads. It is ultimately important that sufficient residual actuation authority be available in a damaged composite.

Two types of actuation curves can be derived from these tests: one for composites subjected to the test once and one for composites subjected to the test twice. There is a distinct difference in the actuation performance of a composite never before strained and a composite already loaded to a certain peak strain. The curves obtained for the former may be referred to as First Cycle Loading (FCL), those for the latter may be referred to as Second Cycle Loading (SCL). SCL curves will serve as indicators of residual properties.

It should be noted that all tests were conducted in **load control**. In other words, the test machine was controlled based on load feedback readings from a load cell. This procedure was dictated by the need to ensure the composites were actuated while under a constant load (a setup not possible with **position control**). As a result the gripping procedure became somewhat tricky. The test machine was set to apply a small, but positive, load (about 5 lbs). Then upon closing the grips onto the specimen, this load was applied instantaneously and maintained. If the load were set to be zero, then it would be possible for the

composite to be loaded in compression, as fluctuations in applied load were normally observed. Of course, this was an undesirable effect as it might have introduced damage in the composite and compromised the accuracy of the results. This setup also meant that in order to load the composite to a predetermined *strain* value it would be necessary to monitor the strain gage reading: when the desired strain was reached, loading was manually interrupted and put on hold.

Stiffness data (*stress vs. static strain*) can be derived from actuation under load tests. As mentioned earlier, the static strain during each actuation step may be derived from the actuation strain data (computing the mean of the maximum and minimum actuation strains). Since the load level is known (and the cross-sectional area of the composites is known) then stress vs. static strain curves can be constructed. Additionally a few pure stress vs. strain tests can be conducted on selected composites to provide further verification of stiffness measurements. With these tests, a ramp loading (1 lb/sec) will be specified: the load will be increased from its minimum value to the maximum expected value and then back to the initial value again. As with actuation tests, this test can be repeated to measure residual stiffness properties.

3.3.3 Fiber Fragmentation Measurements

In order to characterize the fragmentation process, several composites were immersed in sulfuric acid in order to dissolve the matrix material around the piezoelectric fibers. Additionally, useful insight can be gained from analysis of distribution functions of fragment lengths. Ultimately it is desired to extrapolate

key model parameters from model/experiment fragmentation correlations. These parameters determine the quality of the model predictions.

To dissolve the matrix, the composites were first placed in a fine porous teflon pouch. This was necessary to ensure acid could be drained without losing fiber fragments. The pouch was then placed onto a glass slide and into a container full of sulfuric acid (95.8% H_2SO_4). Effective matrix dissolution occurs after about 4 hours with "fresh" acid. Times are usually longer when using recycled acid. No incompatibilities were encountered between PZT-5H fibers and sulfuric acid: fibers were immersed in acid for a period of a few days and no detrimental effect was noticed. After the initial four hour bath, the composites were carefully removed from the acid bath and the top E-glass layer was gently removed while care was taken not to disturb the fibers. The composites were then immersed a second time to complete the matrix dissolution process. Once sufficient dissolution was achieved, the composites were lifted out of the bath by lifting the microscope slides and left to dry for a few hours. Fiber fragments from the central gage length were collected in a dark container and were inspected under a microscope to observe their degree of fragmentation. Care was taken to avoid including fibers fragments far from the central gage area and fragments close to repaired locations (epoxy was used to fill in gaps and holes generated from electrical breakdown). This task was simplified by the fact that fibers did not flow easily from their original locations, thereby enabling greater control and accuracy in collecting fragments. Photomicrographs of the fragment groups were taken to aid the fragmentation count and to provide permanent record. Fragment lengths were then measured from printouts of the pictures and

fragment distribution functions were compiled by using the fiber diameter as scaling parameter. More than 100 fibers fragments were counted for each composite. Since composites were loaded to different peak strain levels, this enabled the compilation of average fragment length (or break density) as a function of applied peak strain as well as distribution functions of fragment lengths as a function of applied peak strain.

Several photomicrographs of selected test article fragment groups were taken to characterize the details of fragmentation (see Figures 3.12-3.14).

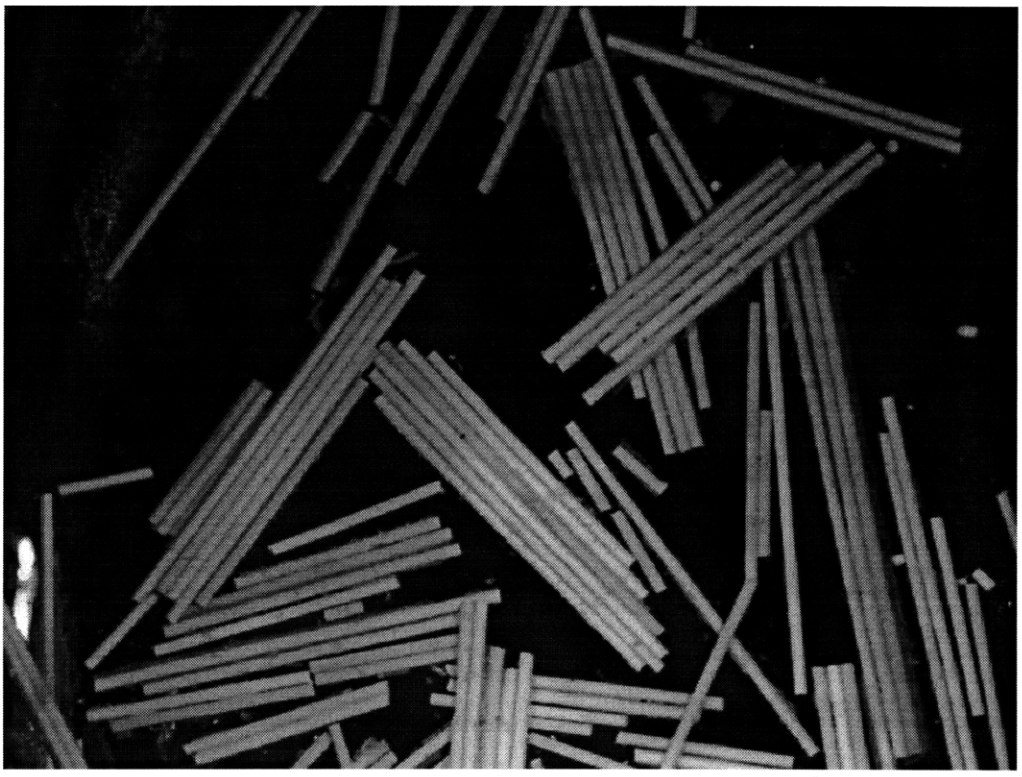

Figure 3.12. Photomicrograph illustrating the distribution of fragment lengths in composite AT115 loaded to a peak strain of 5500 με. The fiber diameter (130 μm) may be used as scale parameter.

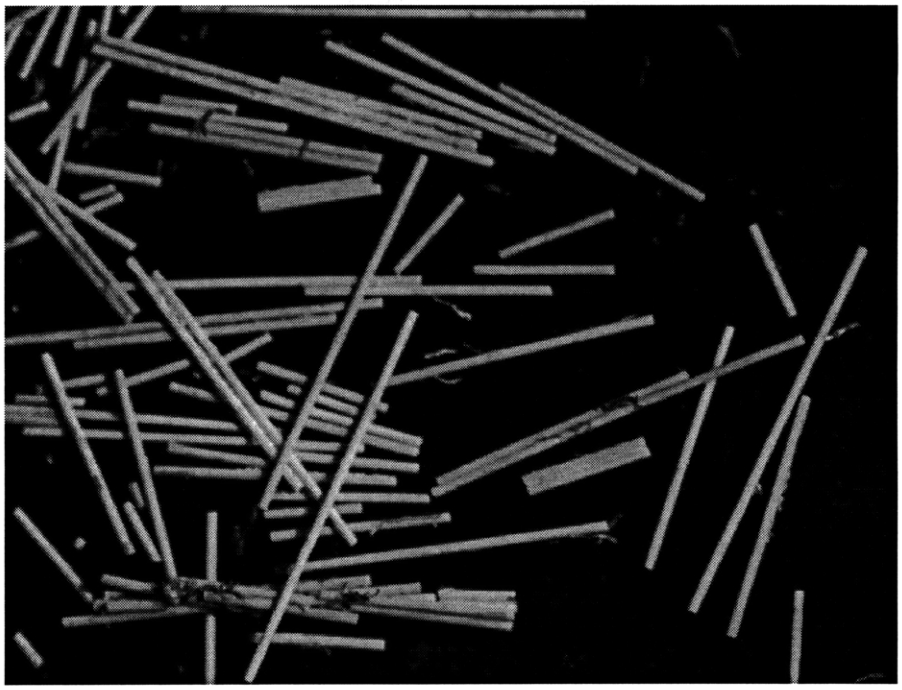

(a)

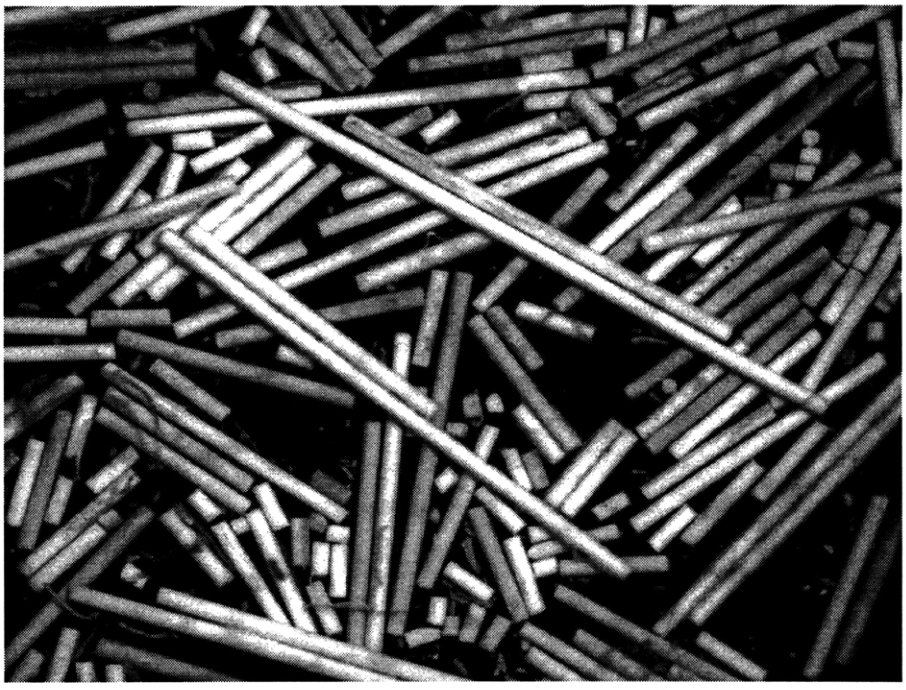

(b)

Figure 3.13. Photomicrographs illustrating the distribution of fragment lengths in (a) composite AT99 loaded to a peak strain of 8000 με, and (b) composite AT118 loaded to a peak strain of 12000 με. The fiber diameter (130 μm) may be used as scale parameter.

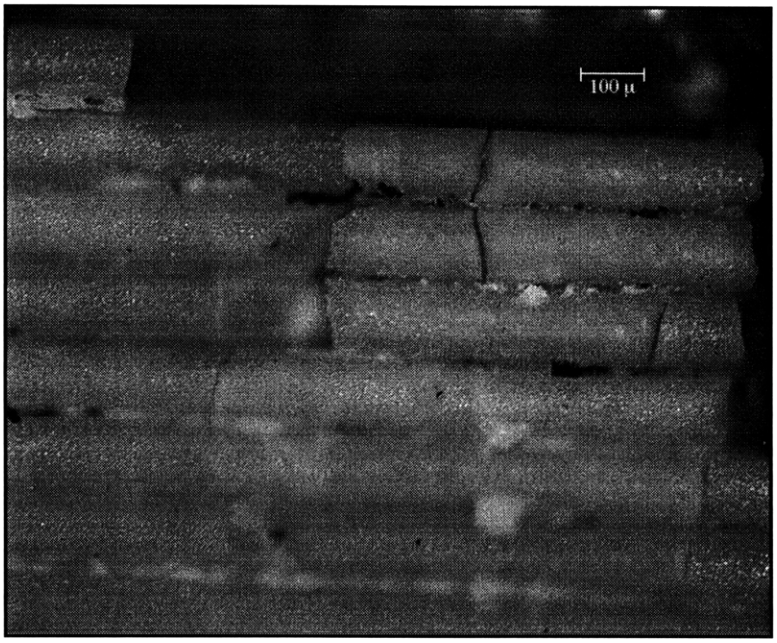

(b)

Figure 3.14. Photomicrograph of fractured fibers in laminated composite (loaded to peak strain of 9000 με) after matrix dissolution in sulfuric acid.

The distribution functions of fragment lengths for the experimental data are computed based on the definition of $P(x;n,\delta)$ in Chapter 2 (eqs. 21, 22). Recall that $P(x;n,\delta)\Delta x$ is the percentage of fragments of length between x and $x+\Delta x$, call that N_x/N_{tot}. Bins b1, b2, b3, etc. may be defined respectively for fragments of lengths $x_{min}<x_{b1}<x_{min}+\Delta x$, $x_{min}+\Delta x<x_{b2}<x_{min}+2\Delta x$, $x_{min}+2\Delta x<x_{b2}<x_{min}+3\Delta x$ with Δx a constant and x_{min} the minimum detected fragment length. Therefore the experimental distribution function of fragment lengths is:

$$P_{exp}(x_{bi};n,\delta)=\frac{1}{\Delta x}\frac{N_{x_{bi}}}{N_{tot}} \tag{85}$$

where i indicates the bin number of interest (i=1,2...maximum number of bins), $N_{x_{bi}}$ is the number of fragments in bin bi, N_{tot} is the total number of fragments measured, and Δx is the fixed bin size. The cumulant F is then determined as described in Chapter 2 (eq. 30).

3.4 Test Matrix

In order to properly validate the theoretical simulation provided in Chapter 2, a considerable amount of data must be obtained and analyzed. Performance metrics will be *actuation* performance, *stiffness* and *fiber fragmentation* data. An extensive testing program was envisioned for this work. A large number of composites were manufactured to this end: the total number being 43. Manufacturing and non-loaded testing were accomplished in different stages. The maximum strain envisioned for this series of tests was 12000 με. Historically, composites have reached ultimate strain levels ranging from 12000 με to 15000 με. In order to avoid failures while collecting actuation data at the higher strains it was decided to set a limit.

3.4.1 Test Samples

The following table summarizes the available composites sorted by actuation strain level. The numbers in parenthesis indicate the total number of repairs for the composite as incurred during all preparatory testing stages. Some of the composites had considerable electrical problems and ended up as candidates for non-electrical stiffness tests: AT89, AT91, AT95, AT105, AT106, AT116, and AT119.

Table 3.3. List of composites available for testing (strain, ε, in με). Composites marked with an asterisk (*) were not in electrical working condition and were used for purely mechanical stiffness tests.

450>ε	450>ε>400	400>ε>350	350>ε>300	300>ε>250	250>ε>200	200>ε
80 (0)	78 (0)	77 (0)	74 (0)	84 (0)	101 (2)	*89 (0)
112 (4)	81 (0)	87 (0)	75 (0)	90 (2)	104 (4)	*91 (2)
		93 (5)	76 (0)	*95 (5)	*105 (5)	113 (1)
		96 (5)	79 (0)	102 (5)	*106 (4)	115 (1)
		97 (5)	86 (0)		120 (4)	*116 (3)
		100 (1)	92 (2)			*119 (2)
		108 (3)	94 (2)			
		109 (1)	98 (1)			
		110 (2)	99 (1)			
		111 (2)	103 (3)			
		117 (7)	107 (4)			
			114 (3)			
			118 (2)			

3.4.2 Test Schedule

The task of organizing a thorough test matrix was rendered a little more difficult than expected by the higher-than-average variation in the quality and performance of the available pool of active composites. Some composites will be subjected to a test twice to measure residual properties. The test will be repeated as discussed in section 3.3.2 and will provide both FCL and SCL curves. Since it is desirable to have at least a pair of FCL and SCL curves for the same maximum strain level, composites with similar performance should be paired up. However, many repairs were done on some of the composites which might lead to inaccurate results. After careful evaluation of the pool of composites, it was decided that if performance was similar after repairs, then it would be suitable to pair composites, provided the repairs were minor.

The first tests will be stiffness tests, on electrically poor (preferably non-working) composites with little mechanical damage (few repairs). This will ensure that electrically sound composites will be available for actuation tests. The final configuration of the selected test matrix is illustrated in Table 3.4. All composites to be tested for use in this work are included in the list.

Table 3.4. Test matrix sorted in order of increasing maximum strain. Stiffness tests on electrically non-working composites are listed first. Tested twice refers to repetition of the actuation under load test to measure residual properties.

Test	Composite	Max Strain (με)	(A)ctuation or (S)tiffness	Tested Twice?	Status
1	AT105	6000	S	No	Elec Prb
2	AT106	6000	S	Yes	Elec Prb
3	AT95	6500	S	No	Elec Prb
4	AT91	7500	S	Yes	Elec Prb
5	AT119	10000	S	Yes	Elec Prb
6	AT89	12000	S	No	Elec Prb
7	AT116	12000	S	No	Elec Prb
8	AT97	3500	A	Yes	OK
9	AT108	3500	A	Yes	OK
10	AT81	4000	A	No	OK
11	AT87	4000	A	Yes	OK
12	AT92	4000	A	No	OK
13	AT94	4000	A	Yes	OK
14	AT101	4000	A	No	OK
15	AT84	4500	A	Yes	OK
16	AT120	4500	A	No	OK
17	AT76	5000	A	No	OK
18	AT79	5000	A	Yes	OK
19	AT90	5000	A	Yes	OK
20	AT104	5000	A	No	OK
21	AT78	5500	A	No	OK
22	AT110	5500	A	Yes	OK
23	AT113	5500	A	No	OK
24	AT115	5500	A	Yes	OK
25	AT80	6000	A	Yes	OK
26	AT93	6000	A	No	OK
27	AT96	6000	A	Yes	OK
28	AT112	6000	A	Yes	OK
29	AT74	7000	A	No	OK
30	AT75	7000	A	Yes	OK
31	AT86	7000	A	No	OK
32	AT103	7000	A	No	OK
33	AT107	7000	A	Yes	OK
34	AT98	8000	A	No	OK
35	AT99	8000	A	Yes	OK
36	AT109	9000	A	Yes	OK
37	AT102	10000	A	Yes	OK
38	AT77	10000	A	Yes	OK
39	AT117	11000	A	Yes	OK
40	AT100	12000	A	Yes	OK
41	AT111	12000	A	Yes	OK
42	AT114	12000	A	Yes	OK
43	AT118	12000	A	No	OK

3.5 Summary

In this chapter, techniques for manufacturing and testing active composites were described in detail. These included techniques for manufacturing the active ply, poling, laminating, as well as methodologies for conducting actuation under load and stiffness tests. These techniques are currently employed for all manufacturing and testing needs, and provide a sufficiently repeatable procedure. Material quality, however, still suffers from considerable variation. Possible explanations for these issues have been presented.

Chapter 4

Model/Experiment Correlation

4.1 Introduction

The most important part of experimental-based research work is the correlation between simulation and testing results. At this stage a considerable amount of experimental data is available for analysis. While it provides ample results for verification of the analytical model it also gives the opportunity to gain increased understanding of the material systems and manufacturing processes being used. In particular, issues of manufacturability have proven to be critical for the effective development of active composites, and most of the advances have resulted from careful analysis of manufacturing steps and their effect on final performance [15]. While care was taken to develop a consistent and repeatable manufacturing process, the current active composite material quality is still characterized by considerable variability in performance results. The most probable explanations for this behavior reside in the trapping of air voids and in the quality of the piezoelectric fibers.

Some manufacturing results (particularly in terms of quality of composite performance) were presented in the modeling and testing chapters, however, a unified analysis of the data is now necessary. Additionally it will be critical to

evaluate the accuracy and fidelity of the data collected. With this in mind, the main objectives for this chapter are:

- to organize test results to ensure that consistent behaviors are observed, and
- to correlate observed actuation, stiffness and fragmentation results with model simulations.

This chapter will be dedicated to analyzing and correlating experimental data for fiber fragmentation, actuation strain, and stiffness with model predictions. The first part of this chapter will discuss some of the issues associated with the general quality of the tests and the overall quality of the active composites. Then attention will be focused on the details of fiber fragmentation, i.e. the most critical issues affecting all subsequent correlations. After a qualitative analysis/discussion of the experimental fragmentation results, a more in-depth analysis with correlation to model results will be undertaken. This will provide better insight into key model parameters which are critical for accurate model predictions of the selected performance metrics. The following sections will then look into the quality of the data, and the corresponding correlation for actuation and stiffness performance. The last section will summarize and unify the analysis and discuss possible improvements to the methodologies used.

4.2 General Data Considerations

The first step in the experiment/model correlation consisted of organizing the experimental data. A few distinct testing problems occurred throughout the experimental phase as noted in Table 4.1: data acquisition, gripping, electrical, and strength problems. Data acquisition problems were characterized by strain gages

peeling off during testing. In this case the test was generally not repeated and only partial data was collected (mostly for verification). Gripping problems occurred as a result of loss of pneumatic gripping pressure. Loss of gripping pressure was detected both acoustically and by monitoring strain gage data. The corresponding tests were aborted and not repeated. Two electrical problems occurred. One was a typical breakdown of the same type encountered during representative cycle testing and poling (under no load). The other was an accidental disconnection of the lead wires for composite AT112: in this case it was decided to use the composite as strain gage dummy. The last problem was mechanical failure as composite AT118 ultimately failed at 12000 με. All other composites successfully completed the intended tests. Table 4.1 summarizes results from the testing schedule.

The analysis of the available data will involve consideration of fiber fragmentation, actuation, and stiffness data and correlation with model predictions. It is first most useful to analyze the data collected and investigate the information it provides. This will give improved understanding about the quality of the tests and of the underlying mechanisms. For the purpose of model correlation, fragmentation data is most critical, and because of the nature of the fragmentation tests, it is also most likely to be easily "contaminated" by mishandling or additional damage (see section 3.3.3). The following section will attempt to validate this data, correlate with model predictions, and provide a basis for all other model/experiment correlations.

Table 4.1. Actuation and stiffness test results.

Test Article	Max Strain (με)	(A)ct. or (S)tif.	Tested Twice?	Test Successful?	Comments (D=matrix dissolved)
AT105	6000	S	No	Y	D
AT106	6000	S	Yes	Y	D
AT95	6500	S	No	Y	
AT91	7500	S	Yes	Y	D
AT119	10000	S	Yes	Y	D; Data acquisition problem.
AT89	12000	S	No	Y	Data acquisition problem.
AT116	12000	S	No	Y	D; Data acquisition problem.
AT97	3500	A	Yes	Y	
AT108	3500	A	Yes	Y	
AT81	4000	A	No	Y	D
AT87	4000	A	Yes	Y	
AT92	4000	A	No	Y	D
AT94	4000	A	Yes	Y	D
AT101	4000	A	No	Y	
AT84	4500	A	Yes	Y	
AT120	4500	A	No	Y	D
AT76	5000	A	No	Y	
AT79	5000	A	Yes	Y	
AT90	5000	A	Yes	Y	
AT104	5000	A	No	Y	D
AT78	5500	A	No	N	Gripping problems; test aborted.
AT110	5500	A	Yes	Y	D; Data acquisition problem.
AT113	5500	A	No	Y	D
AT115	5500	A	Yes	Y	D
AT80	6000	A	Yes	Y	
AT93	6000	A	No	Y	D
AT96	6000	A	Yes	Y	D
AT112	6000	A	Yes	N	Elect prob: used as strain gage dummy
AT74	7000	A	No	Y	
AT75	7000	A	Yes	Y	
AT86	7000	A	No	Y	
AT103	7000	A	No	Y	D
AT107	7000	A	Yes	Y	D
AT98	8000	A	No	Y	D
AT99	8000	A	Yes	Y	D
AT109	9000	A	Yes	Y	
AT102	10000	A	Yes	N	Gripping problems, test aborted.
AT77	10000	A	Yes	Y	
AT117	11000	A	Yes	Y	
AT100	12000	A	Yes	Y	D
AT111	12000	A	Yes	N	D; Electrical short
AT114	12000	A	Yes	Y	
AT118	12000	A	No	Y	D; Loaded to failure

4.3 Fiber Fragmentation Data

4.3.1 Introduction

Fragmentation data was collected from direct estimation of the number and length of fragments after matrix dissolution using the techniques described in section 3.3.3. Overall, fragmentation data was collected for 17 composites and is illustrated in Figure 4.1 as average fragment length vs. applied maximum strain. It must be noted that one composite, T42, was not manufactured in any of the aforementioned batches. This composite was manufactured earlier in time and was included in this analysis to provide a data point in the very low strain regime, where no other data points were available. Specimen T42 was manufactured with doped epoxy and using degassing. It was loaded to a maximum strain of 2000 με and fiber fragmentation data was successfully collected. This additional data point was included to enable more accurate characterization of the model statistical parameters at low strain levels. While care was taken to avoid the introduction of handling damage, this process cannot guarantee that fragments as measured are derived exclusively from the applied test mechanical loads. Ideally, non-destructive techniques should be used to characterize the extent of fiber fragmentation, and this, perhaps, will be addressed in future work.

It is immediately clear that a trend of decreasing average fragment length with increasing peak strain is present. This is consistent with expectations for this test. The errorbars illustrate one standard deviation from the mean average fragment length as calculated from the corresponding distributions of fragment lengths.

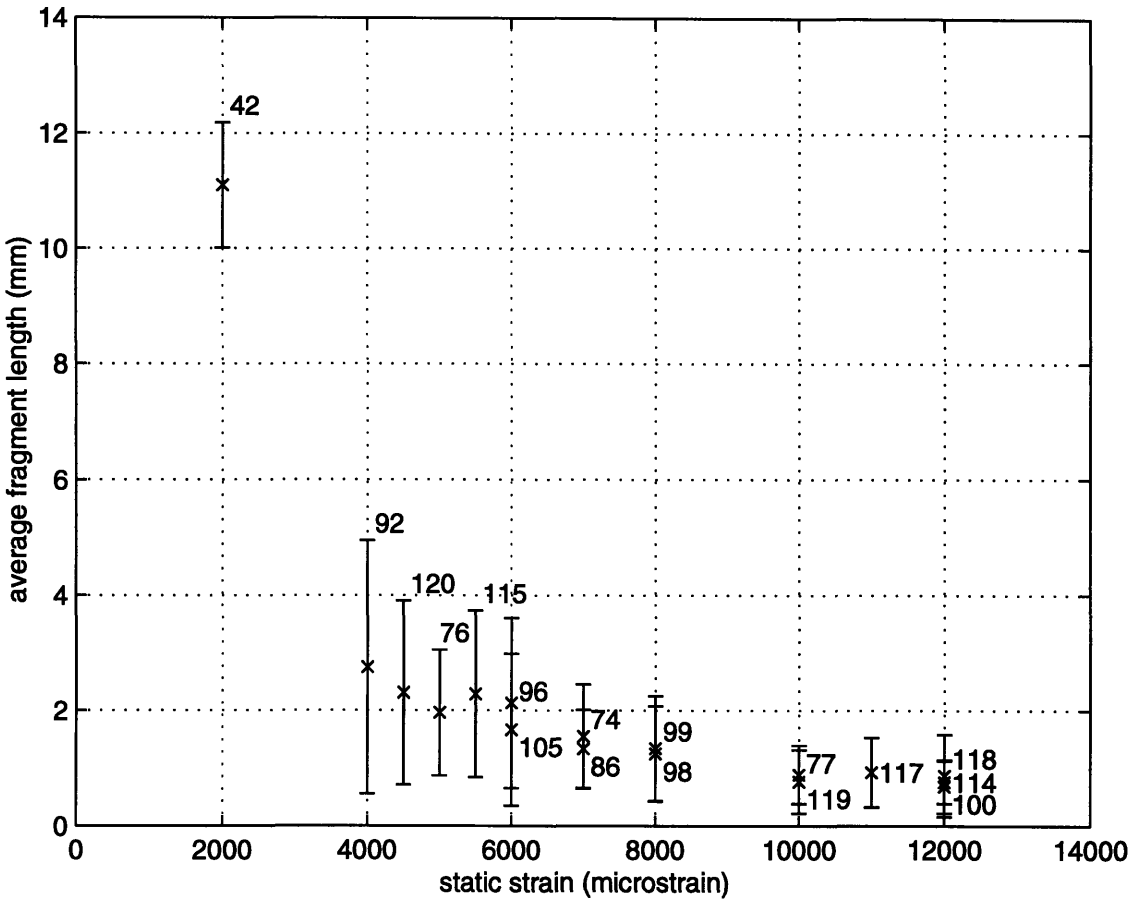

Figure 4.1. Fragmentation data for a pool of 17 composites. The number labels indicate the corresponding composite number.

There is a minor degree of variation in the detected pattern, particularly in the medium-low strain range. This stems from observations of unexpectedly small fragment lengths at these strain levels. In particular it seems as composites loaded between 4000 με and 6000 με have slightly smaller average fragment lengths. Perhaps additional damage was introduced between the testing and matrix dissolution steps. The only real way to validate this observation is to execute the entire testing more carefully. Further insight into the quality of fragmentation data may be gained by looking at the fragment distributions in Figures 4.2a-4.2d

(each figure contains distributions for three composites loaded to similar maximum peak strains).

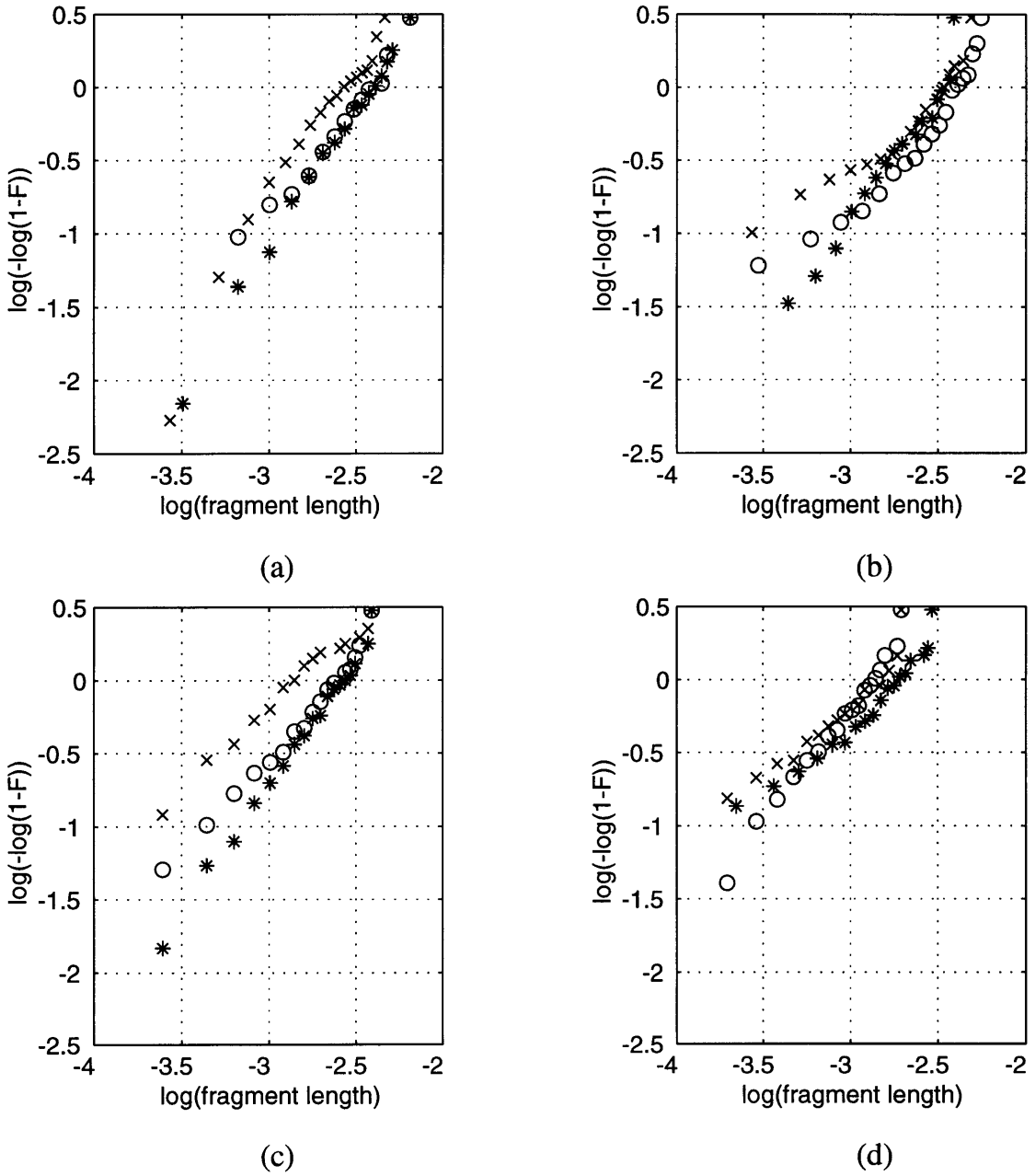

Figure 4.2. Plots of cumulative distributions of fragment lengths for composites loaded to peak strains of (a) 3500 με (AT108, ∗), 4000 με (AT87, o), and 4500 με (AT84, x); (b) 5000 με (AT76, ∗), 5500 με (AT115, o), and 6000 με (AT105, x); (c) 7000 με (AT74, ∗), 8000 με (AT99, o), and 10000 με (AT119, x); (d) 11000 με (AT117, ∗), 12000 με (AT114, o), and 12000 με (AT100, x). F is the cumulant of the fragment length distribution function.

The distributions of fragment lengths display consistent behaviors: lightly loaded composites have larger fragments in general, therefore the corresponding curve is shifted to the right. More heavily loaded composites will have curves shifted to the left. This pattern is observed when moving from Figure 4.2a (composites loaded to 3500 με, 4000 με, and 4500 με) to Figure 4.2d (11000 με, and 12000 με). Additionally the smallest fragments for lightly loaded composites should be larger than those for more heavily loaded composites. This is reflected by the left-most data point for each composite. As may be observed, some very small fragments are present in very lightly loaded composites (Figure 4.2a). While theory does not prevent the appearance of these small fragments in lightly loaded composites, it seems unlikely that composites in Figure 4.2a would have smaller fragments than those in Figure 4.2b (loaded to strains of 5000 με-6000 με), or similar to those in Figure 4.2c (loaded to strains of 7000 με-10000 με). This could potentially indicate the introduction of handling damage, or poor quality of fragmentation data. As will be seen in the following sections, the actuation performance showed a reduction consistent with what predicted with model simulations in Chapter 2. This seems to indicate that the *correct* fragmentation mechanisms are occurring in the composite as it is being strained, so the anomalies could be artificial.

For the case of multiple composites loaded to the same maximum strain there is good correlation among average fragment lengths. The three composites loaded to 12000 με displayed very similar average fragment lengths in Figure 4.1 and somewhat similar distribution of fragment length curves in Figure 4.3d. The same applies to composites loaded to 6000 με (Fig. 4.3a), 8000 με (Fig. 4.3b), and 10000 με (Fig. 4.3c).

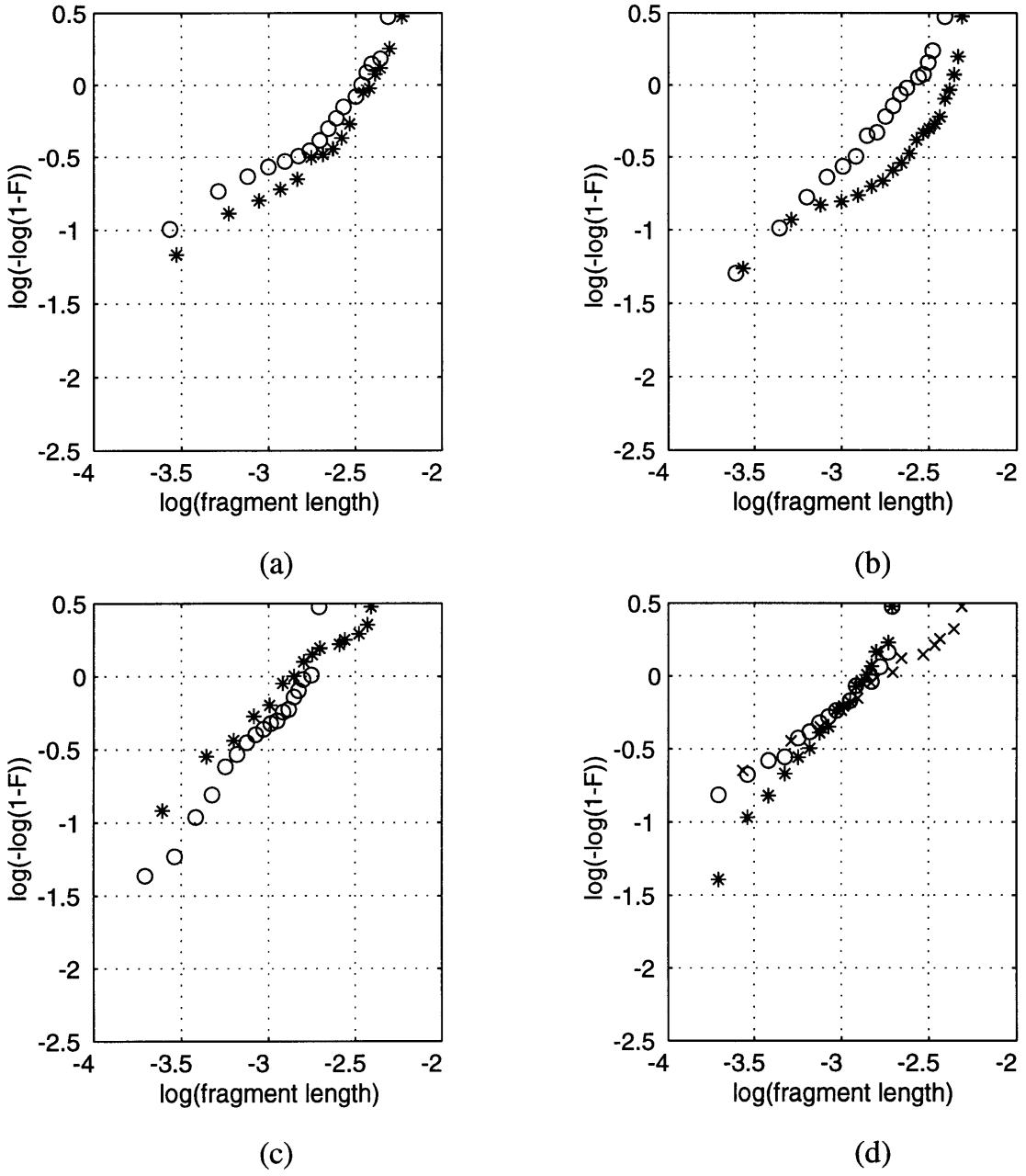

Figure 4.3. Plots of cumulative distributions of fragment lengths for composites loaded to peak strains of (a) 6000 με (AT96, *; AT105, o); (b) 8000 με (AT98, *; AT99, o); (c) 10000 με (AT119, *; AT77, o); (d) 12000 με (AT114, *; AT100, o; AT118, x). F is the cumulant of the fragment length distribution function.

It must also be noted that these results include all composites which were made in different manufacturing sessions, with different fibers, and possibly many

other differentiating factors. Composites were manufactured in batches of four. Table 4.2 helps to identify the manufacturing batches and the corresponding overall quality (based on actuation strain and capacitance, which have been seen to correlate very well with each other).

Table 4.2. Manufacturing batches. Fiber quality was established based on a set of single-fiber tests [10]. Overall quality is based on actuation performance and capacitance values (the larger the better).

Batch	Composites	Date Manuf.	Fiber Batch	Fiber Quality	Overall Quality
1	74, 75, 76, 77	11/24/96	N/A	N/A	Good
2	78, 79, 80, 81	2/9/97	8/22/95 #3	Average	Excellent
3	84, 86, 87	2/13/97	8/22/95 #3	Average	Average
4	89, 90, 91, 92	4/5/97	11/14/95 (89); 8/22/95 #3	Average	Average
5	93, 94, 95, 96	4/7/97	11/14/95 (93,94); 1/31/97 (95,96)	Average	Average
6	97, 98, 99, 100	4/8/97	1/31/97	N/A	Average-Good
7	101, 102, 103, 104	4/8/97	1/31/97 (101); 12/13/95	N/A	Mediocre-Average
8	105, 106, 107, 108	4/9/97	12/13/95	N/A	Mediocre
9	109, 110, 111, 112	4/9/97	12/13/95	N/A	Average-Good
10	113, 114, 115, 116	4/10/97	12/18/95	N/A	Poor
11	117, 118, 119, 120	4/10/97	12/18/95	N/A	Poor-Mediocre

Table 4.2 suggests that a minor degree of correlation between fiber batch and overall quality can be derived. In general the quality of batches 7 through 11 is mediocre, whereas all other batches are somewhat better.

4.3.2 Statistical Fragmentation Parameters

The first step in the validation process is extrapolating all necessary statistical parameters from the fragmentation data. This will provide a complete set of parameters for the model, which are necessary for all subsequent correlation with actuation and stiffness data. Once basic parameters have been set it will then be possible to apply the model to the actuation and stiffness data: the real

goal of this work. This will ultimately determine the quality of the overall modeling work.

Tailoring the model to accurately capture essential composite behavior is the most critical step of this thesis. It must be once again emphasized, however, that due to considerable variability in composite fragmentation data, there is room for ranges when fitting statistical parameters. Parameters of concern are the Weibull modulus, ρ, the fiber characteristic stress, σ_o, the corresponding characteristic length, L_o, and the residual (compressive) stress σ_{res}. Most important, however, is extrapolating an approximate value for the fiber recovery length, δ. The use of fragmentation data for this purpose is ideal as it provides information about fragmentation at the saturation regime. Saturation occurs when breaks are no longer formed as fibers are extensively fragmented. In this case all fragments are limited in length between δ and 2δ and therefore no more breaks can occur (the far field applied stress is never recovered in the small fragments). When saturation occurs, the fragmentation curve flattens and reaches a horizontal asymptote. The value of this asymptote can be used to represent the average fragment length or the corresponding inverse, the number of breaks per unit length. Since the maximum fragment length at saturation is 2δ then an approximate value for δ may be derived. By looking at the fragments from the pool of dissolved composites, it was noted that the smallest fragments lengths were of the order of the fiber diameter. This was consistently observed for all composites, in particular those loaded to the largest peak strains. Some of the composites loaded to the maximum test strain of 12000 $\mu\varepsilon$ also failed. This effectively impaired any chance of possibly collecting data at higher strain regimes, i.e. the regimes close to saturation. For this reason, it was assumed that

the fiber recovery length be of the order of the fiber diameter, namely 150 μm. This is the value used throughout the rest of this work.

The next step will then involve fitting the four main statistical parameters to the available fragmentation data over the available range of peak strain values. This is accomplished by using a weighted least squares fit of the model fragmentation curve to the available data. The weighing factor used is the standard deviation from the mean fragment length for each composite. The decision to employ a weighing factor was dictated by the necessity to account for possible inaccuracies in measured fragmentation data for composites loaded to smaller peak strains. This algorithm was executed in MATLAB by using the available *FMINS* function. *FMINS* minimizes a function of several variables by using a Nelder-Mead type simplex search method [25]. In this case, the function to minimize is the square of the standard deviation-weighted difference between predicted and measured mean fragment lengths. In particular a simulation for the average fragment length is used, properly modified to allow for the dynamic updating of the four key statistical parameters: ρ, σ_o, L_o, and σ_{res} as required by *FMINS*. Minimization starts with a set of 4 initial guesses for the parameters of interest, which are then automatically updated and modified based on the internal search routines of *FMINS*. Several sets of "realistic" initial guesses for ρ, σ_o, L_o, and σ_{res} were used as starting points. "Realistic" implies that the parameters have a reasonable value. For instance, the Weibull modulus for typical fibers ranges from slightly larger than 1 to about 15. Furthermore, for brittle fibers, as is the case with PZT 5H, this range is reduced from slightly larger than 1 to about 5. Typical starting guesses were as follows: ρ=2-3, σ_o=20-60 MPa, L_o=0.02-0.1 m, and σ_{res}=2-10 MPa. In the end the minimization successfully converged to the

same fragmentation curve, however, the values of the statistical parameters varied from solution to solution. In other words, multiple solutions for the statistical parameters are available to generate the same curve. This is probably a result of the freedom in fitting 4 variables with similar roles in the driving equations. This is the case for σ_o and L_o which both appear in the denominator of the expression of Weibull fiber strength: in one solution set, σ_o could be large and L_o small, and viceversa in another case. Effectively this provides some freedom in the selection of the final solution set. The final solution set which appeared more consistently in the minimization is the following: ρ=2.2, σ_o=56.11 MPa, L_o=0.02472 m, σ_{res}=1.637 MPa. The main model parameters used in this work are summarized in Table 4.3. Parameters have been subdivided into *fragmentation* and effective material properties to illustrate the area where they have key roles.

Table 4.3. Summary of main model parameters used in this work.

Fragmentation		
Recovery Length, δ (m)	1.5×10^{-4}	
Weibull Modulus, ρ	2.2	
Characteristic Stress, σ_o (MPa)	56.11	
Characteristic Length, L_o (m)	0.0247	
Residual Stress, σ_{res} (MPa)	1.637 (compressive)	
Effective Material Properties	*Actuator*	*Structural Ply*
Stiffness, E (GPa)	100	22
Thickness, t (RVE value) (μm)	82	110
Composite Length, L (m)	0.1	
Matrix Thickness (μm)	37	
Matrix Shear Modulus (MPa)	10	
Shear Lag Parameter, $1/\Gamma_o$ (m)	2.0232×10^{-3}	

The final model fit is illustrated in Figures 4.4 and 4.5. Figure 4.4 shows the average fragment length curve in its entirety. Note that at zero strain, the

fragment length is equal to the composite initial length of 0.1 m, assuming undamaged fibers. A more detailed view of the critical part of the curve is given in Figure 4.5, where all available fragment data is displayed.

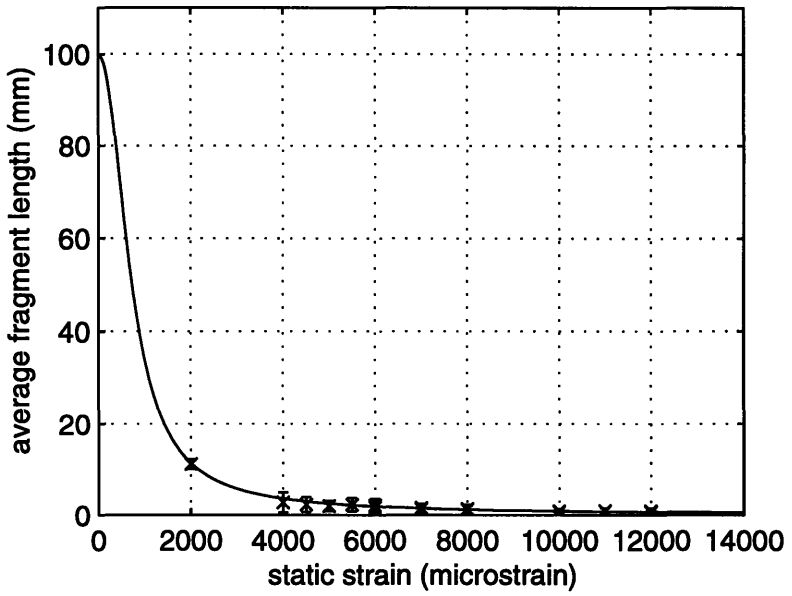

Figure 4.4. Final fit of model curve to available fragmentation data.

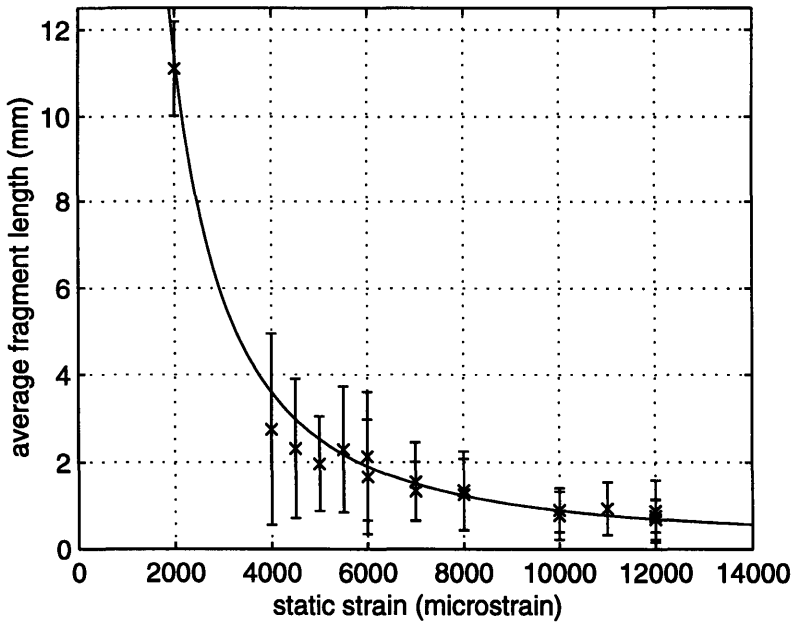

Figure 4.5. Detail of final fit of model curve to available fragmentation data.

As will be seen with the actuation under load curve, this solution seems to slightly underestimate the magnitude of the residual stress, represented as the point of rapid accumulation of breaks. It is however a good fit to the available fragmentation data. This further reinforces the idea that better data might provide more accurate fits and therefore more realistic model correlation. This is not to say that the actuation (or stiffness) data are not valid: possible inaccuracies introduced during the matrix dissolution step would only affect the fragmentation results and resulting model correlation.

4.3.3 A Note on Distributions

Distribution functions provide useful insight into the quality of this work. First they can help validate the accuracy of the distribution functions employed in the fragmentation algorithm. Additionally they are excellent indicators of the quality of the measured fragmentation data. A comparison of predicted and experimentally determined distribution functions is presented in Figure 4.6 for composites loaded to peak strain values of 5000 με, 8000 με, and 12000 με. The quantity visualized is log(-log(1-F)) as was done in Chapter 2. F is the cumulative distribution function of fragment lengths (eq. 30). An excellent degree of correlation was observed between experiment and theory, which indicates the correct fragmentation patterns are present and characterized in the model. Additionally, the same data sets illustrated in Figures 4.2a-4.2d are now compared to the corresponding model predictions in Figures 4.7a-4.7d.

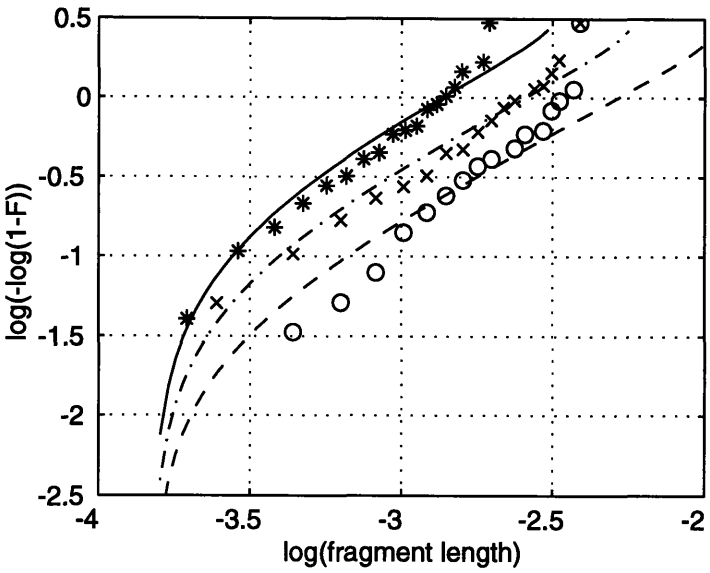

Figure 4.6. Weibull plots of the predicted (lines) and experimental (data points) fragment distributions for composites loaded to peak strains of 5000 με ('-' and '*'), 8000 με ('-.' and 'x'), and 12000 με ('--' and 'o'); log(-log(1-F)) with F the cumulant of the fragment distribution, versus log(fragment length).

Correlation between model predictions in Figures 4.7a-4.7d is more favorable for the more highly strained composites. Figures 4.7c and 4.7d display some exceptionally good correlation between predicted and experimentally determined fragment length distributions. However for lightly loaded composites as in Figure 4.7a, correlation is not as successful. Once again, this observation seems to indicate possible inaccuracies in the low strain level fragmentation data.

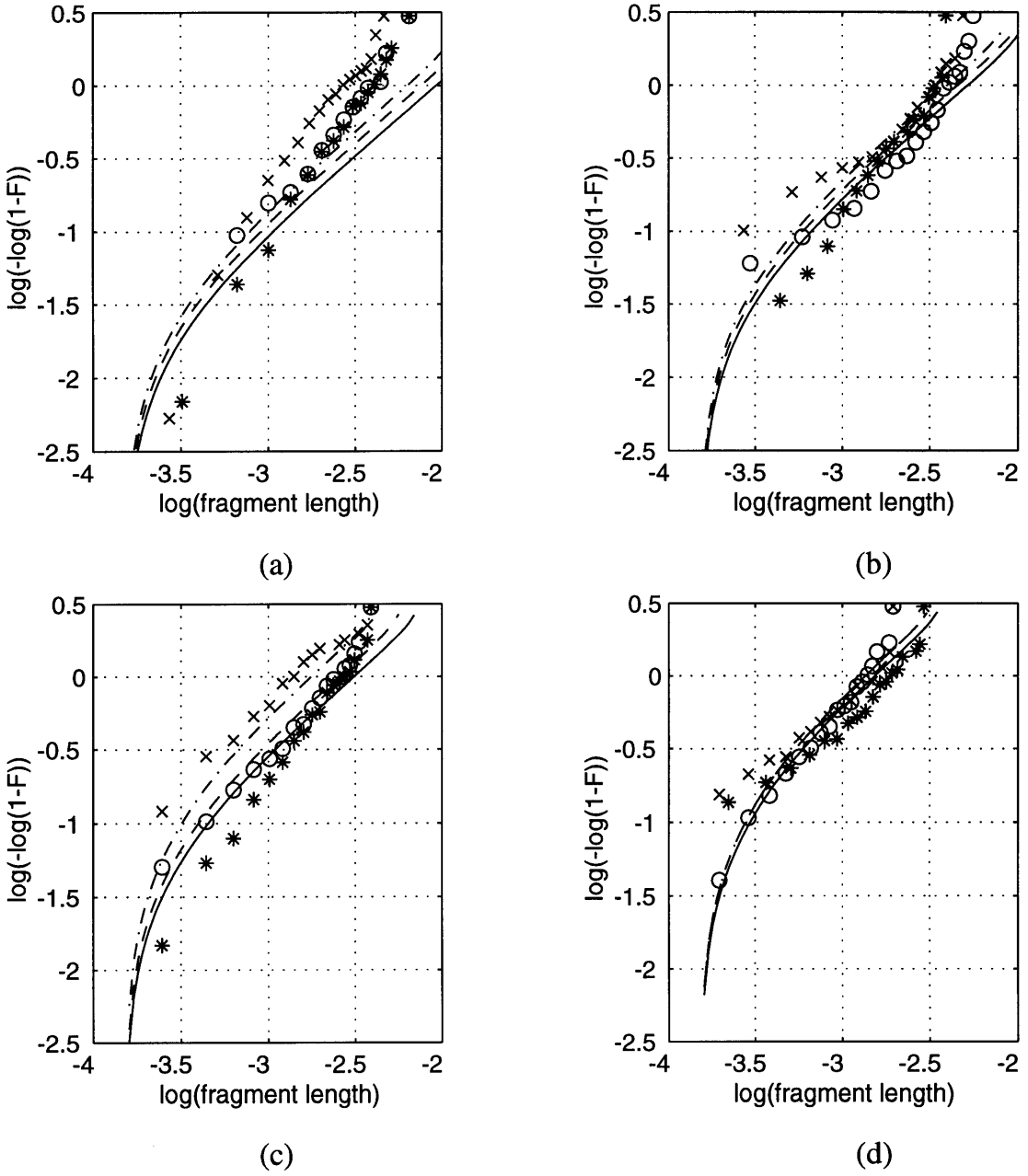

Figure 4.7. Plots of predicted (lines) and experimental (data points) cumulative distributions of fragment lengths for composites loaded to peak strains of (a) 3500 με (AT108, -, ∗), 4000 με (AT87, --, o), and 4500 με (AT84, -., x); (b) 5000 με (AT76, -, ∗), 5500 με (AT115, --, o), and 6000 με (AT105, -., x); (c) 7000 με (AT74, -, ∗), 8000 με (AT99, --, o), and 10000 με (AT119, -., x); (d) 11000 με (AT117, -, ∗), 12000 με (AT114, --, o), and 12000 με (AT100, -., x). F is the cumulant of the fragment length distribution function.

4.4 Actuation Under Load and Stiffness Data

4.4.1 Introduction

The actuation and stiffness data collected from tensile tests was consistent with expected behavior. Expected trends included reduced stiffness and actuation capability as composites were increasingly strained in their first loading cycle. Furthermore a greater reduction was noticed for those composites strained in their second loading cycle (after damage has been accumulated). This is a direct manifestation of the ineffectiveness of the fragmented active fiber at load transfer.

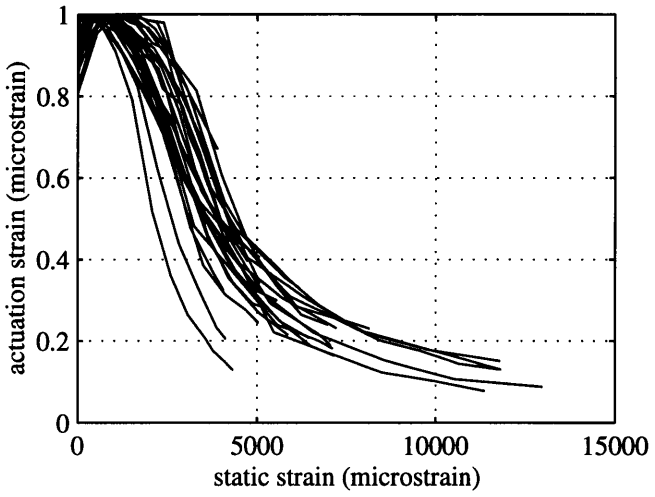

Figure 4.8. Illustration of actuation performance for all composites tested in this work. Note the definition of a "band" of performance.

Figure 4.8 provides useful insight into the range of actuation performance measured during testing. It is important to note that the actuation curves seem to define a *"band"* of performance. This is a critical result as it provides information about the tolerance available for fitting model parameters. As will be seen later, composites can have different residual compressive stresses, different fiber

statistical properties, etc. which end up giving somewhat varied performance. Note that actuation strain has been scaled to unit maximum strains (normalized by each curve's own peak strain).

Some composites loaded to the same peak strain as others displayed considerable variability in both actuation strain performance and stiffness. In that case, it was convenient to compute mean actuation strains and a mean stiffness in order to present one data set for each peak strain loading. The corresponding magnitude of the errorbars is then determined by the difference in the normalized values of the actuation strain and of the absolute values for stiffness.

Examples of results for actuation strain are illustrated in Figures 4.9a and 4.9b. Note that actuation strain varied from composite to composite, as was illustrated in Table 3.1. Similar stiffness plots are illustrated in Figures 4.10a and 4.10b. The remaining data is available in Appendix B and later in this chapter when model correlation is discussed.

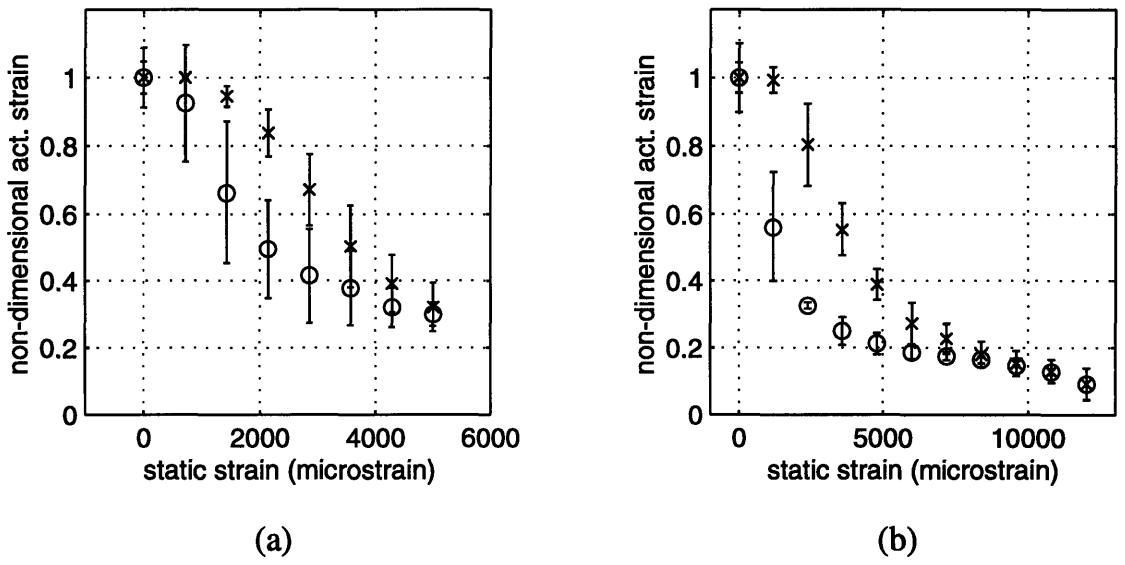

Figure 4.9. Illustration of the averaged actuation strain performance for composites loaded to peak strains of (a) 5000 με, and (b) 12000 με. First loading (FCL) data points are marked by 'x', residual points (SCL) by 'o'. Errorbars are computed with respect to the normalized values.

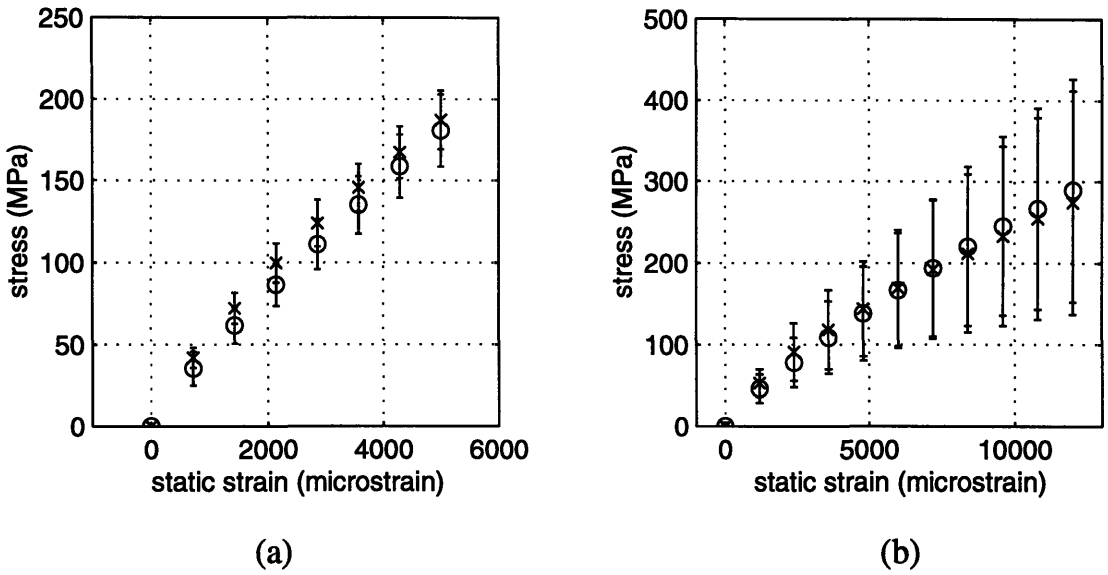

Figure 4.10. Averaged stiffness for composites loaded to peak strains of (a) 5000 and (b) 12000 με. FCL data points are marked by 'x', SCL by 'o'.

As for the case of actuation strain, stiffness FCL and SCL curves have key differences. FCL curves typically start with the undamaged average composite stiffness and asymptote (at the higher strain levels) to the stiffness of the glass lamina. As the active fibers fracture, they become more inefficient at load transfer (due to the effect of the recovery length) and the composite displays reduce stiffness. Composites loaded to 5000 με (Fig. 4.10a) show more consistent data, whereas those loaded to 12000 με (Fig. 4.10b) have considerably more variation. This was observed for a few composites during the experimental phase.

Figures 4.11 and 4.12 illustrate a sampling of the actuation strains recorded for composite AT96 strained from 0 με to a maximum of about 6000 με for a first loading cycle (FCL curve) and repeated test cycle (SCL curve) respectively. The static strain level may be estimated as the average of the two strain values corresponding to the 0V field levels.

In short, the actuation strain data derived in this experimental work is of acceptable quality and effectively characterizes the actual performance of active composites. There are still, however, factors particular to each composite. Some might display an actuation strain which decays rapidly after the first application of load, for others it might be more delayed. This indicates there might be different residual stresses among composites. There may also be slight differences in how damage evolves in each composite, a behavior attributable to different statistical properties (Weibull modulus, characteristic stress and length) associated with the piezoelectric fibers.

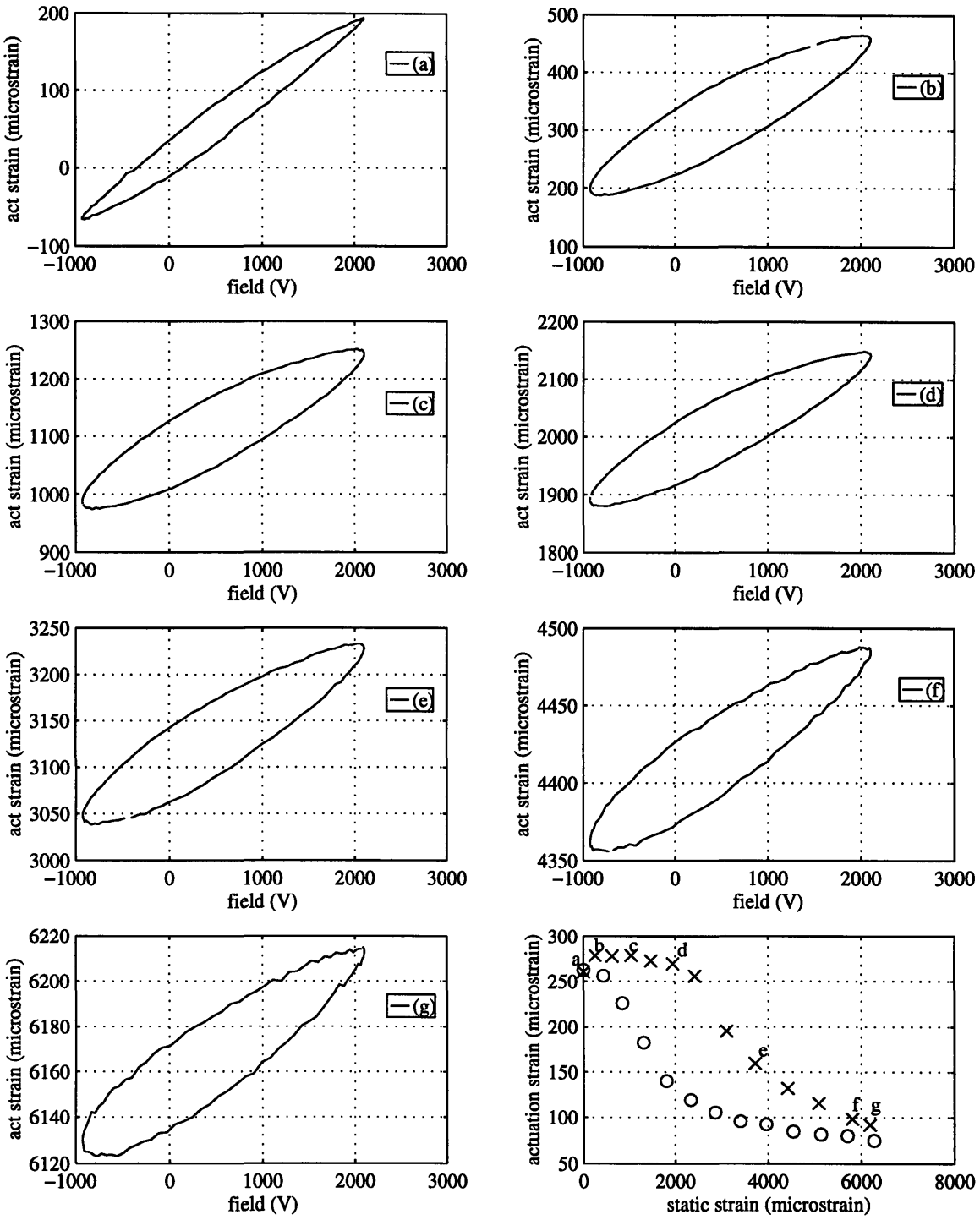

Figure 4.11. Illustration of FCL actuation strain vs. applied electric field for composite AT96, strained to about 6000 με. Increasing strain levels are indicated by the letters a, b, c...up to g, where the composite is loaded to a strain around 6000 με. Approximate static strain level readings may be estimated from the 0V field points.

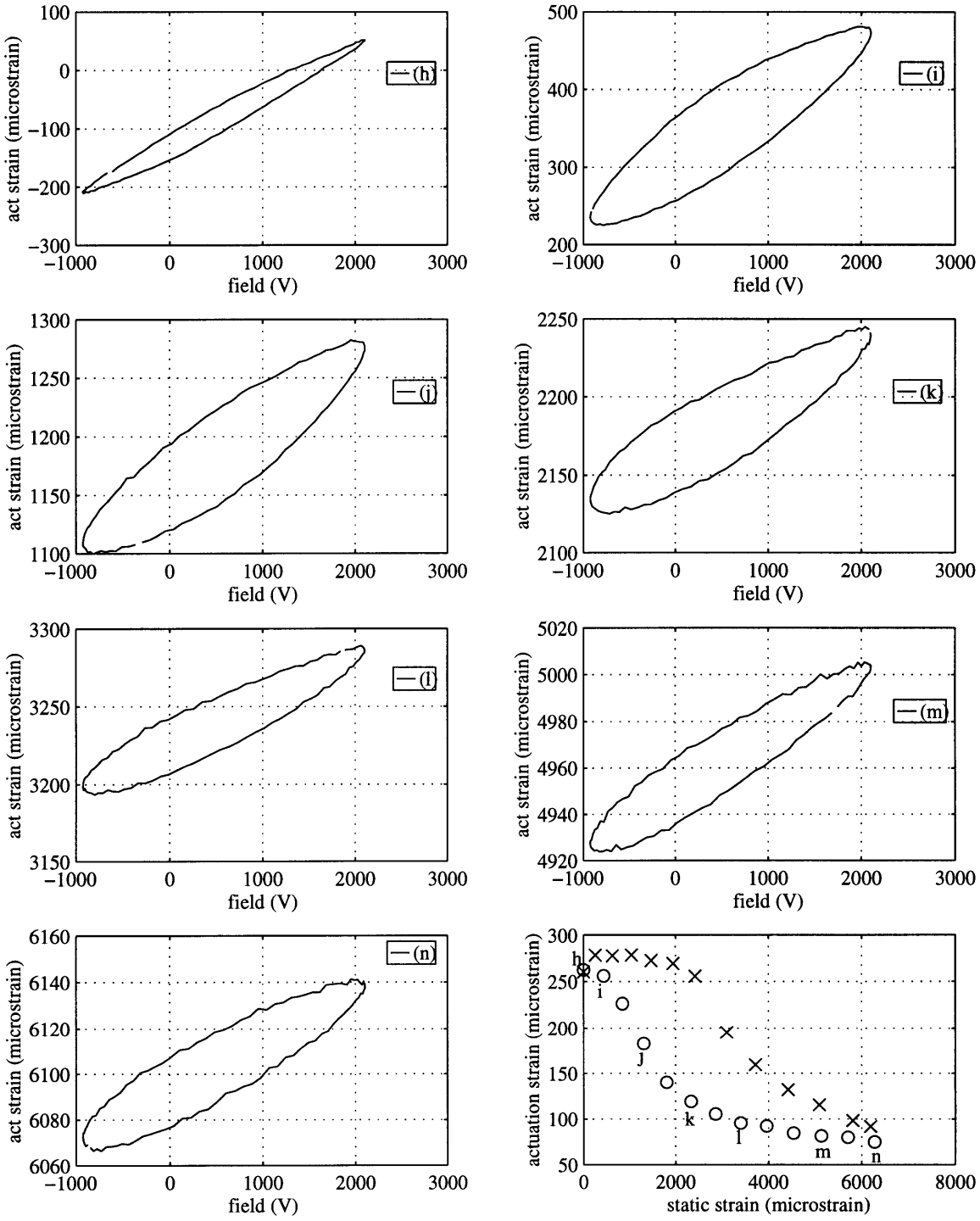

Figure 4.12. Illustration of SCL actuation strain vs. applied electric field for composite AT96, strained to about 6000 με. Increasing strain levels are indicated by the letters h, i, j...up to n, where the composite is reloaded to a strain around 6000 με. Approximate static strain level readings may be estimated from the 0V field points.

As mentioned in Chapter 3, stiffness data was also collected via direct stiffness tests. The reason for this redundancy was to validate the indirect method of collecting stiffness data from actuation strain tests. This enabled to maximize the number of the more important actuation under load tests and still have stiffness data available. Direct stiffness tests were described in section 3.3.2 of the previous chapter. Indirect measurements are derived from the actuation strain data: the strain gage instantaneously records the absolute strain the composite experiences as it is loaded. It is this strain, recorded before actuating the composite, that defines the static strain level. Since the load is also monitored, this results in a discrete data point for a stiffness curve. A few tests were also conducted on spare specimens to ensure creep would not affect the results. It turns out that within the standard timing of an actuation test (5 minutes maximum time when load is held to acquire actuation data) creep effects are in the order of a 0.5% change. In other words the creep effect is negligible.

Comparisons were made to verify the validity of the indirect method for the acquisition of stiffness data. Figures 4.13a through 4.13c illustrate the comparison of the two methods. As may be seen there is sufficient agreement to assume the indirect method is valid. It is however important to remember that as for the case of actuation strain, there is variability in actual properties: stiffness can vary slightly from composite to composite (see Figures 4.10a and 4.10b).

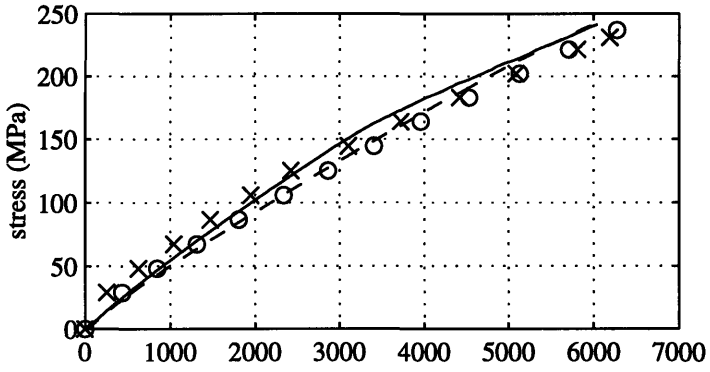

(a)

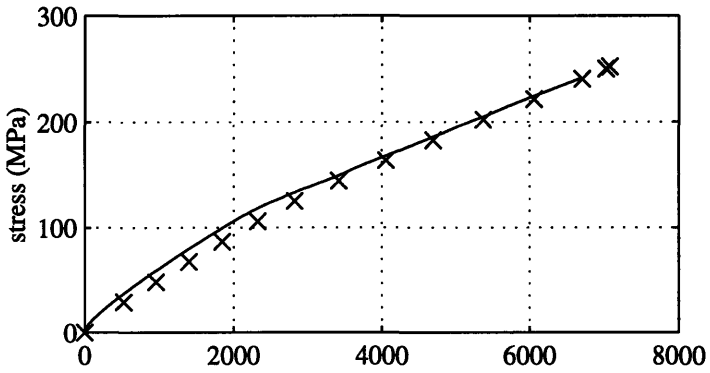

(b)

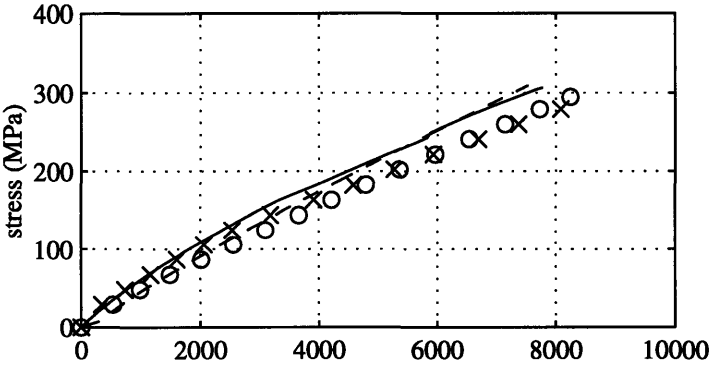

(c)

Figure 4.13. Illustration of direct (lines) and indirect (data points) method for measuring stiffness data for both undamaged and residual properties of composites: (a) AT106 (lines) and AT96 (points) strained to 6000 με, (b) AT95 (line) and AT74 (points) strained to 6500 με, and (c) AT91 (lines) and AT99 (points) strained to 7500 με. Continuous line and the symbol 'x' represent FCL curve, dashed line and the symbol 'o' represent SCL curve.

4.4.2 Actuation and Stiffness Model Correlation

This step is actually just a simple verification of the quality of the results obtained in the previous section, however it is the focal point of this work. No further analysis is required at this time, or even possible for that matter. With the 4 statistical parameters determined, the FCL and SCL curves are automatically defined. It is now time to evaluate the results obtained.

Samples of the main model/experiment correlations for stiffness are illustrated in Figures 4.14 and 4.15, and actuation strain in Figures 4.16 and 4.17. As may be observed, correlation is very good for both actuation and stiffness. The important task now is to characterize various types of material properties and discuss details of the correlations.

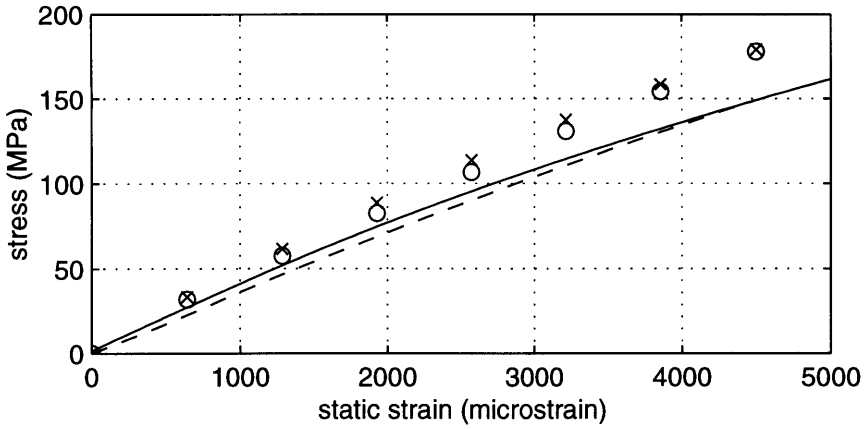

(a)

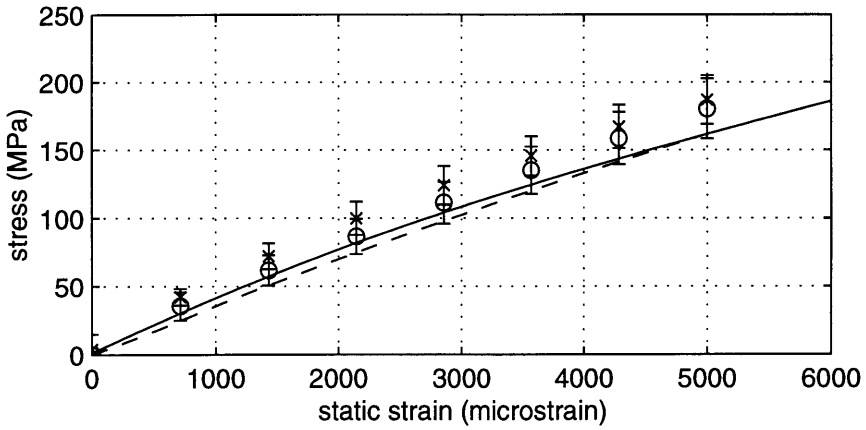

(b)

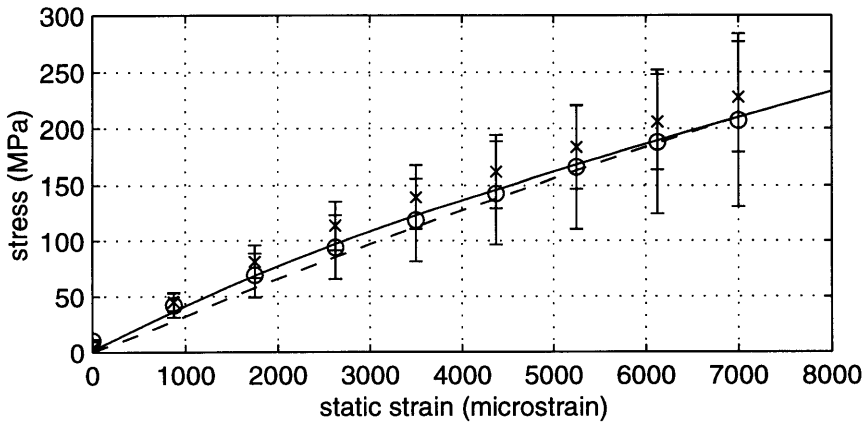

(c)

Figure 4.14. Model/experiment correlation of stiffness for composites loaded to peak strains of (a) 4500 με, (b) 5000 με, and (c) 7000 με. (-, x) FCL curve (eqs. 73, 69), (--, o) SCL curve (eq. 84).

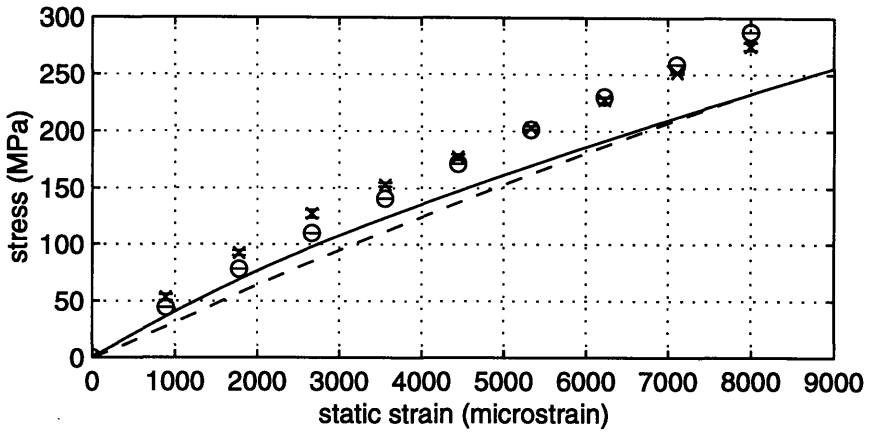

(a)

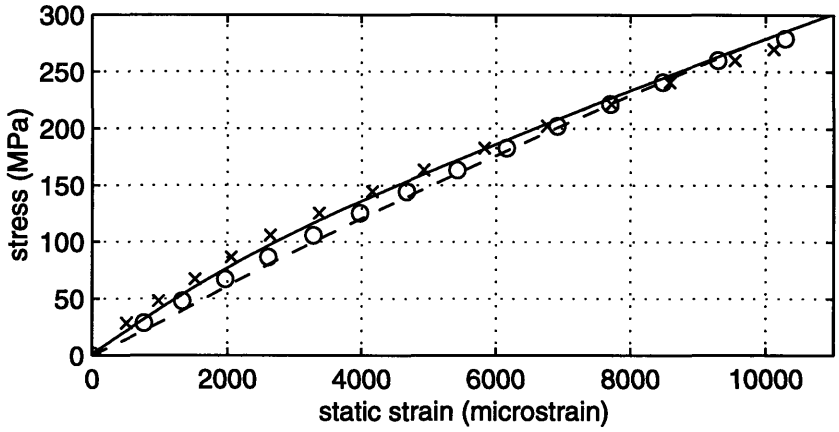

(b)

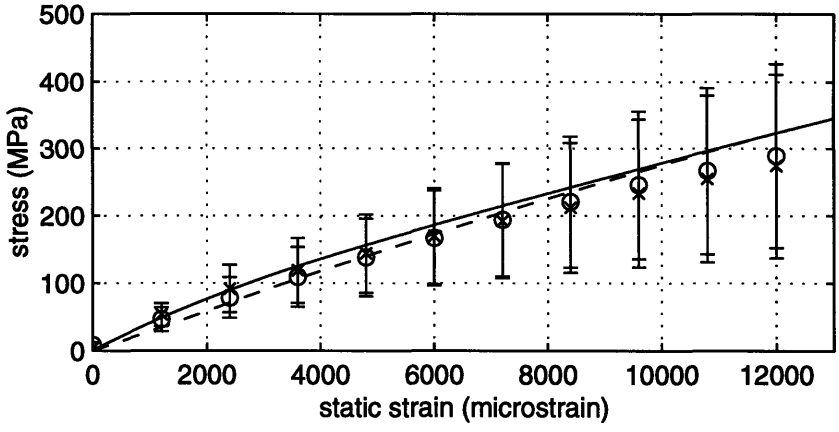

(c)

Figure 4.15. Model/experiment correlation of stiffness for composites loaded to peak strains of (a) 8000 με, (b) 10000 με, and (c) 12000 με. (-, x) FCL curve (eqs. 73, 69), (--, o) SCL curve (eq. 84).

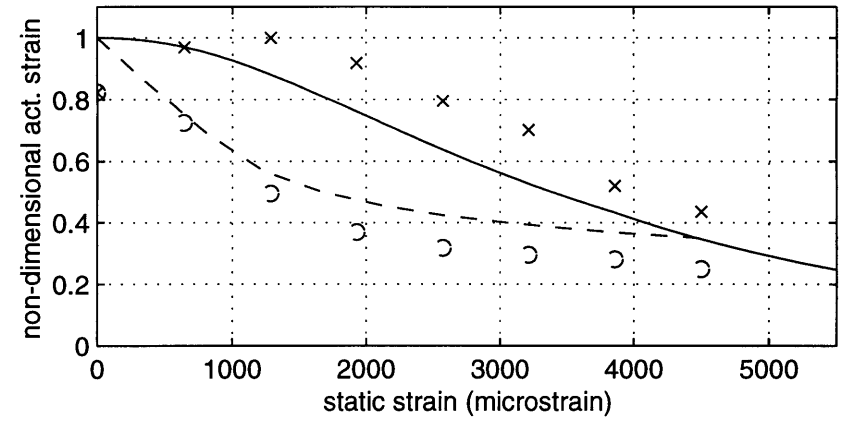

(a)

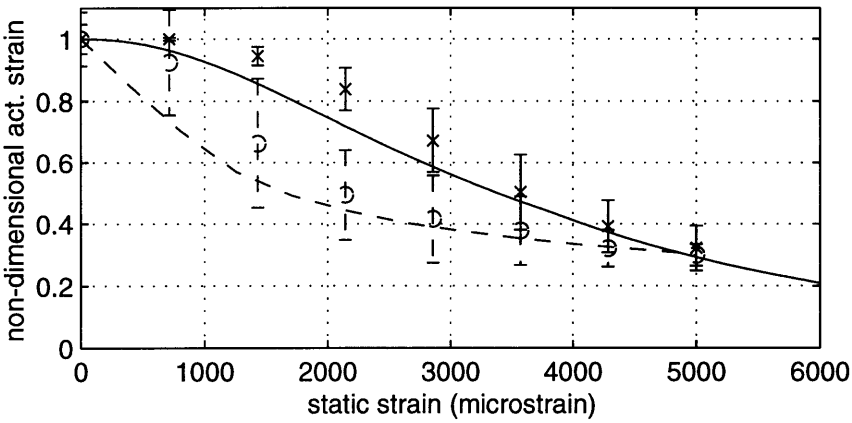

(b)

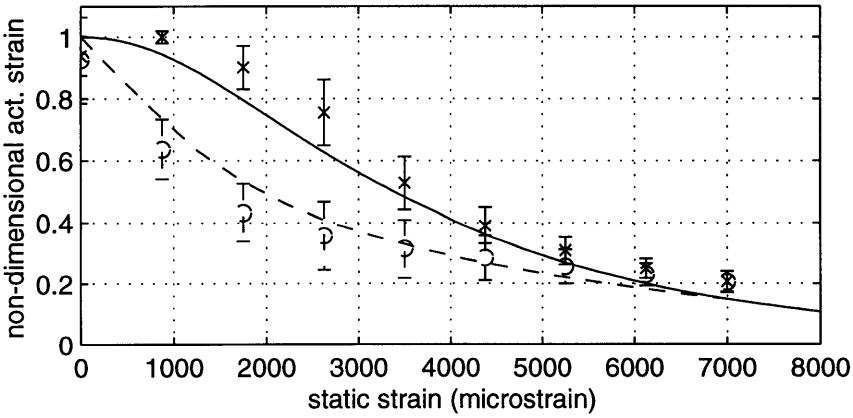

(c)

Figure 4.16. Model/experiment correlation of actuation strain for composites loaded to peak strains of (a) 4500 με, (b) 5000 με, and (c) 7000 με. (-, x) FCL curve (eqs. 73, 70), (--, o) SCL curve (eq. 82).

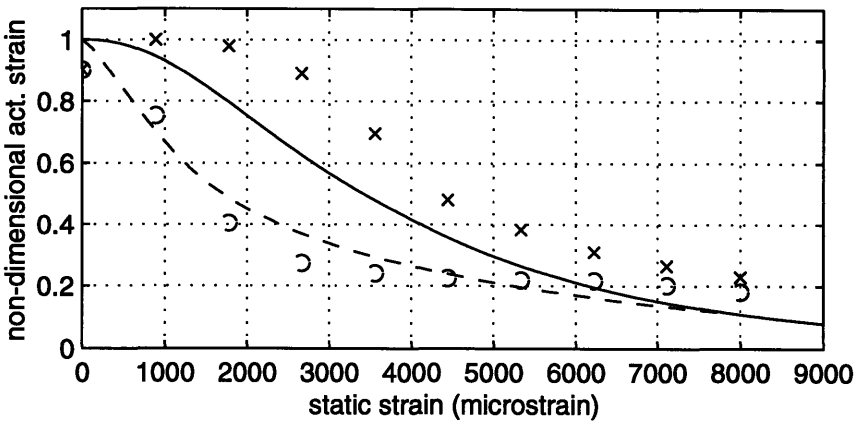

(a)

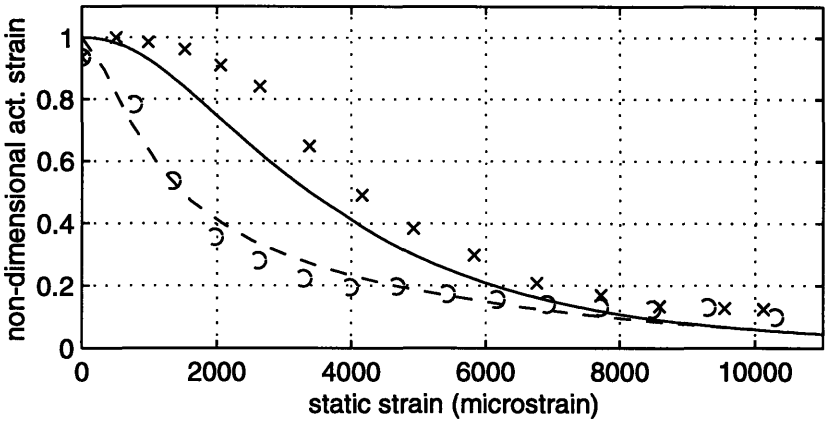

(b)

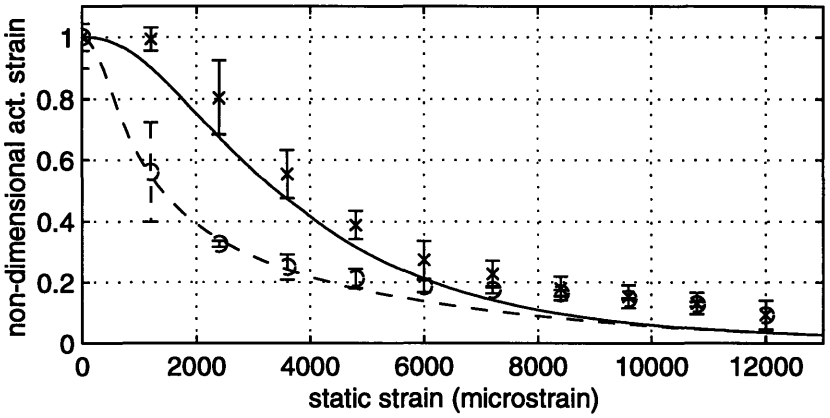

(c)

Figure 4.17. Model/experiment correlation of actuation strain for composites loaded to peak strains of (a) 8000 με, (b) 10000 με, and (c) 12000 με. (-, x) FCL curve (eqs. 73, 70), (--, o) SCL curve (eq. 82).

Particularly useful for estimating the validity of the effective material properties portion of the model was analyzing the stress-strain behavior. The overall model prediction captures the essential trends: the low- and high-strain asymptotes, and the stiffness reduction during the most intense fragmentation regime in the first loading cycle. In the initial stress-strain region (corresponding to undamaged material) the slope determined by the model has a value of approximately 38 GPa which compares favorably with what is predicted with a simple rule of mixtures: 37.8 GPa. Correlation with experimental results is not as direct as variability in stiffness is displayed. It is nevertheless possible to see that the general stiffness recorded experimentally is "centered" around this value. In the large strain regime (where most of the actuator fragmentation has occurred) the slopes asymptote, in both model and experiment, to a value of about 20 GPa, which is close to the stiffness of the structural lamina (22 GPa). This illustrates the minimal contribution of the highly fragmented active fibers to overall material stiffness in the high-strain regime. The reason for this ineffectiveness resides in the fiber fragment length being mostly recovery length, therefore incapable of efficient stress transfer. While stiffness measurements vary considerably from composite to composite the relative FCL and SCL (residual) responses are captured particularly well. The residual stiffness properties are characterized by reduced stiffness up to the peak strain. Within this regime, no fragmentation occurs but the material response is affected by the inefficiencies in load transfer. Once the composite is loaded above the previous maximum peak strain then fragmentation resumes and follows the path described in the first cycle curve.

Similar comparisons were performed in terms of actuation capability (see Fig. 4.12). In this case, model predicted actuation strain (non-dimensionalized) was compared with actuation strains of the same composites used in Figure 4.11. Considering the presence of significant variation in experimental properties, the degree of correlation is still quite remarkable. One trait that seems to be underestimated is the magnitude of the residual stress. The value determined by fitting the model FCL fragmentation curve to the data (σ_{res}=1.64 MPa, compressive) is probably too small. This may be seen from the actuation strain curves in Figures 4.12a through 4.12c, where degradation of FCL actuation strain as predicted by the model occurs sooner than is displayed by experimental data. A larger residual stress would delay the onset of fragmentation as a greater externally applied stress would be required to exceed the compressive pre-stress locked in the actuator. As mentioned in section 4.3.1, this is inevitable since all statistical parameters have been extrapolated from a fit to the available fragmentation data. Certainly, this would be one of the main issues to be addressed in future work.

It is interesting to observe a particular behavior displayed in the actuation data: for some composites at low static strain levels actuation capability actually increases to a maximum value then decreases monotonically (see Figure 4.13 and all previous actuation strain plots). This behavior has been justified by the presence of the mechanical pre-stresses, and is typical of PZT-5H (the fiber piezoelectric material), where compressive prestresses reduce the actuation properties at low mechanical stress levels [26]. Further modeling of this non-linear effect is necessary and will be included in future work. It is not until the compressive load in the actuator fiber is canceled that fragmentation begins.

Overall, the residual stress is a key element in accurately defining performance of active composites.

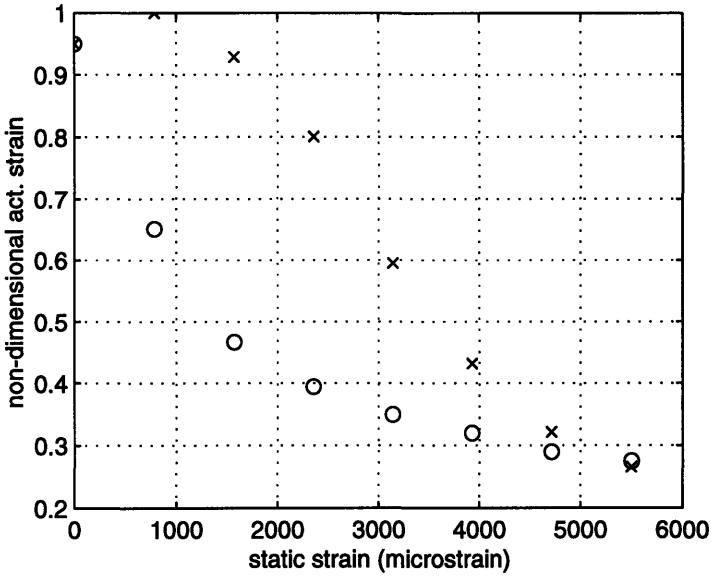

Figure 4.13. Illustration of the non-linear effects of the compressive residual stress on actuation strain for a composite (AT113) loaded to a peak strain of 5500 με. Note the preliminary increase in actuation strain at low static strain levels.

4.5 Summary

This chapter presented the experimental results for fiber fragmentation, actuation under load, and stiffness tests. Emphasis was placed on the need for good fiber fragmentation data in order to obtain accurate predictive capability of actuation and stiffness properties. The model predicted average fragment length curve was optimally fitted to the available fragmentation data in order to derive key model parameters. The optimal parameters were then used in the model to determine actuation and stiffness curves to correlate with experimental data. Successful correlation was observed demonstraing the viability of using this model as a tool for designing structures with active composites.

Chapter 5

Conclusions and Recommendations

5.1 Summary

This thesis was directed at the development of a model for the prediction of actuation and stiffness properties of active fiber composites under mechanical tensile loads. Active composites are new materials with the potential of revolutionizing engineering structures by making active control of structures a more tangible reality. With active control of structures, actuators and sensors can be successfully incorporated into a passive structure to improve performance. Active composites have the advantage of enabling seamless integration by virtue of exceptional conformability, robustness and performance. One of the immediate candidates for the use of active composites is the integral application to helicopter rotorblades for structural vibration reduction. The reduction of structural vibration can lead the way to more efficient, maintainable, and quiet helicopters. Many more structural and acoustic applications can benefit similarly.

If active composites are used in heavily loaded environments, careful planning must be undertaken to ensure the actuator/sensor can function effectively while under load. For instance, if actuators were embedded into a

helicopter blade, they would be directly exposed to a major structural load path as the blades spin and generate large centrifugal forces. If the active composite design is not robust enough, the actuator might not be capable of fulfilling its functional requirement of inducing actuation during flight. It is therefore beneficial to develop a tool to predict with reasonable accuracy the effect of high load environments on active composites. Metrics of interest are actuation authority (strain) and stiffness. Other useful metrics are dielectric properties, however this work is exclusively concerned with actuation and stiffness. This thesis was motivated by this challenge.

Active composites are currently the result of the fusion of conventional composite technology with piezoelectric fibers and interlaminar electrodes. The basic operational mechanics remain the same except that now there is the added capability of inducing (or sensing) a deflection in a host structure. If high loads are present, the combination of strong, brittle fibers with tough matrix leads to the accumulation of damage in the form of fiber fragmentation. Tools are available for the characterization of fragmentation and load transfer within a composite. The goal of this thesis was to develop a unified model that integrates available fragmentation and load transfer theories to give predictive capability for metrics such as actuation strain and stiffness. The approach consisted of developing a model and at the same time conducting an extensive testing program for correlation and validation purposes. A parallel task was also to gain further understanding about the new active composite technology with the goal of continued technological improvement.

The modeling effort was investigated in chapter 2. This chapter dealt with fundamental issues of fiber fragmentation and load transfer with emphasis on the corresponding statistical and mechanical aspects. The first part of the chapter was devoted to the characterization of fiber fragmentation. The main theory was acquired from an elegant fragmentation model developed for standard composites with brittle fibers in a tough matrix. This work emphasized the importance of a critical scale parameter, the fiber recovery length. This parameter describes the area around a fiber crack where load transfer is inefficient. Also important was the understanding that a statistical representation of fiber strength must be provided and that all pertinent parameters must be derived via experimentation. This emphasizes the need for a dual theoretical and experimental approach. A few simplifying assumptions were introduced at this point, namely that the fiber recovery length is constant and stress (strain) recover linearly from the crack to the applied far field value over a distance equal to the recovery length. The main justification for such assumptions was the tight packing of fibers in the composite which would supposedly aid the load transfer mechanisms.

The second part of this chapter dealt with the details of load transfer. A one-dimensional load transfer model was developed for an active ply sandwiched between two passive structural plies. A representative volume element was identified based on this model and all necessary stress-strain relationships were derived. In particular the capability to model strain in the active or passive layer of an idealized composite fragment as a function of the applied stress in the passive layer was developed. The next step was the development of a technique to obtain the overall fragment strain leading to an averaging scheme to derive

global composite response. The metric for global composite response was selected as the strain (deflection) of the passive structural lamina. The last part of Chapter 2 was dedicated to the development of a theory for modeling residual properties, i.e. the properties of the composite once damage has been introduced in the active layer. Fragmentation and load transfer theories were then combined into a unified computer model capable of predicting actuation and stiffness properties of active composites.

The experimental program was discussed in Chapter 3. The details of the manufacturing of active composites were provided with consideration and attention to those steps most critical for material quality. Since one of the secondary goals of this work was to search for possible improvements to the material quality, much care was taken to identify potential problem areas in manufacturing. While no definitive answer was provided, it was possible to highlight the trapping of air voids as one of the main reasons for active composite failure (electrical in particular) as well as considerable fluctuations in fiber quality. Any potential solution to this problem will have to be considered in future work by properly modifying the manufacturing process and improving fiber quality. Details were provided about the configuration of the standard test article selected for this characterization work as well as the testing procedures for the acquisition of actuation and stiffness data. A large number of composites were manufactured to this end and a complete test matrix was envisioned to characterize as thoroughly as possible the actuation and stiffness properties of the standard active composites subject to different environmental loadings. These tests provided an extensive amount of actuation and stiffness data to be used for

subsequent correlation with model predictions. The most critical portion of this work, however, was collecting fiber fragmentation data after damage was accumulated in the composites. This was accomplished by dissolving the matrix material surrounding the damaged active fibers and compiling fiber fragment length distribution functions based on observed fragment lengths.

After the testing stage, a considerable amount of data was available for analysis and correlation. All results were analyzed in Chapter 4. Model/experiment validation was accomplished by first extrapolating all pertinent statistical parameters by fitting the model fragmentation curve to the available fragmentation data. With this knowledge in hand, the remaining task was to verify the accuracy and quality of the predicted actuation and stiffness properties compared to collected data. Very good correlation was observed, showing that the actuation and stiffness properties of active composites (including residual properties) can be successfully modeled. This concluded all experimental and theoretical work.

5.2 Conclusions and Contributions

5.2.1 Conclusions

This work developed a successful model for the prediction of actuation and stiffness properties of active composites. Provided all relevant fiber fragmentation statistical parameters can be successfully extrapolated from available fragmentation data, this model has proven to be a valuable tool for the advancement of active composites. While some difficulties were encountered in collecting good fragmentation data, the model did provide very good results.

This shows that *it is indeed possible to model actuation and stiffness properties of an active composite (structure)*, and a preliminary framework has been provided. In particular it was demonstrated that it is possible to obtain good correlation with experimentally determined actuation and stiffness trends. While the trends have been successfully captured, it became clear that the quality of the correlation is heavily dependent on the quality of the available fragmentation data. To this end, the information provided by the distribution functions of fragment lengths has proven to be critical for assessing the quality of fragmentation data. If additional damage is introduced in the composite at any stage after mechanical testing, inaccurate statistical parameters will be derived which will adversely affect the quality of predicted actuation and stiffness curves. Additionally it has become clear that a large statistical pool of test coupons is necessary to improve the quality of the model fit. Modeling the performance of an active composite is a complex task: many variables/parameters affect final performance. This finding reinforces the concept that highly standardized and repeatable procedures must be employed, from manufacturing to testing. In particular *less destructive fragment detection techniques should be employed.* By reducing the number of unknown variables affecting final performance, it will be possible to better identify and model active composites.

It must also be remembered that the fragmentation theory employed in this work was developed for a single fiber embedded in a matrix material, an arrangement referred to as a *single-filament-composite* (*sfc*). The composites used in this study are comprised of multiple fibers. While these fibers have been assumed to be non-interacting, this is probably not entirely true. This reinforces

the need to conduct similar tests on *single-filament composites*, particularly to extrapolate more accurate statistical parameters. Nevertheless, even with these simplifying assumptions this model has proven capable of effective material representation, and can therefore be used as envisioned.

5.2.2 Contributions

The general contribution of this thesis was the development of a set of tools for modeling actuation and stiffness properties of active composites subjected to tensile loads. Among these tools are a unified model and a set of testing methodologies aimed at directly characterizing actuation strain and stiffness. Additionally, a thorough description of the manufacturing of active composites has been presented.

The modeling effort successfully integrated existing fiber fragmentation and load transfer theories into a unified tool capable of modeling the properties of an active structure loaded in tension and accumulating damage in the form of cracks in the active element. This model can be applied to any structure where an active layer is embedded or bonded to a host passive structure. The additional capability of modeling *residual* properties has also been applied. This last feature will be most beneficial where there is the need to ensure that an active composite can provide sufficient actuation authority while subjected to repetitive loading cycles.

The testing and manufacturing methodologies presented in this work provide the capability to experimentally assess critical performance features of active composites to be employed in heavily loaded environments (tensile loads). This thesis has provided a set of useful tests for the evaluation of actuation and

stiffness properties of active composites. A link has also been established between measurable quantification of damage, in the form of fragmentation, and final performance. This work can now be used as a starting point for more advanced and refined tools to be used in the development of active composites.

5.3 Recommendations for Future Work

Perhaps the most immediate task in support of this work would be the acquisition of more (and better) fragmentation data. A larger experimental set of composites would ensure a more accurate characterization of performance metrics such as actuation strain and stiffness. In particular it has been shown that more low strain level data is necessary for accurately fitting a meaningful model curve to the experimental fragmentation data.

A fragment detection technique has been presented in this work, however, better methodologies should be investigated. Emphasis should be placed on techniques which do not affect the levels of accumulated damage but at the same time provide complete fragmentation data.

Additionally, the experimental work should be conducted on single-filament-composites to more accurately determine all fiber fragmentation statistical parameters. In the case of single-filament-composites, it would also be useful to investigate the effect of passive reinforcing fibers surrounding the single active fiber. Mathematical load transfer models are available for such configurations and by taking an approach similar to that employed in this work, it might be possible to gain better insight into the key dynamics of this problem.

Lastly, on the modeling side, it would be beneficial to investigate the effect of a linear elastic, but non-constant, recovery length, and compare with current model results.

References

[1]Derham, R. C. and Hagood, N. W., "Rotor Design Using Smart Materials to Actively Twist Blades", *Proceedings of the American Helicopter Society 52nd Annual Forum*, Washington, DC, June 4-6, 1996.

[2]Shaw, J. and Albion, N., "Active Control of the Helicopter Rotor for Vibration Reduction", *Journal of the American Helicopter Society*, July 1981, pp. 74-76.

[3]Du Plessis, A. J. and N. W. Hagood, "Performance Investigation of Twist Actuated Single Cell Composite Beams for Helicopter Blade Control", *6th International Conference on Adaptive Structures and Technology*, Key West, FL, 1995.

[4]Hagood, N. W., Bent, A. A., "Development of Piezoelectric Fiber Composites for Structural Actuation", AIAA Paper No. 93-1717, *Proceedings of the 34th AIAA Structures, Structural Dynamics, and Materials Conference*, La Jolla, CA, 1993.

[5]Bent, A. A., Hagood, N. W., and Rodgers, J. P., "Anisotropic Actuation with Piezoelectric Fiber Composites", *Proceedings of the Fourth International Conference on Adaptive Structures*, Paper 93-04-36, Cologne, FRG, 1993.

[6]Rodgers, J. P. and Hagood, N. W., "Manufacture of Adaptive Composite Plates Incorporating Piezoelectric Fiber Composite Plies", *Proceedings of the 36th AIAA/ASME/ASCE/AHS Structures, Structural Dynamics, and Materials Conference*, New Orleans, LA, April 10-14, 1995.

[7]Bent, A. A., *S.M. Thesis*, MIT, January 1994.

[8]Bent, A. A. and N. W. Hagood, "Improved Performance of Piezoelectric Fiber Composites Using Interdigitated Electrodes", SPIE Paper No. 2441-50, *Proceedings of the 1995 North American Conference on Smart Structures and Materials*, San Diego, CA, 1995.

[9]Rodgers, J. P. *S.M. Thesis*, MIT, May 1995.

[10]Bent, A. A., *Ph.D. Thesis*, MIT, February 1997.

[11]Curtin, W. A., "Exact Theory of Fibre Fragmentation in a Single-Filament-Composite", *Journal of Materials Science*, v. 26, 1991.

[12]Sutcu, M. "Weibull Statistics Applied to Fiber Failure in Ceramic Composites and Work of Fracture", *Acta Metall.*, v. 37, 1989.

[13]Gao, Z. and Reifsnider, K. L., "Tensile Failure of Composites: Influence of Interface and Matrix Yielding", *Journal of Composites Technology and Research*, v. 14, No. 4, Winter, 1992.

[14]Jones, R. M., "Mechanics of Composite Materials", Scripta Book Company, 2nd ed., 1988.

[15]Subrumanian, S., Reifsneider, K. L., and Stinchcomb, W. W., "Tensile Strength of Unidirectional Composites: The Role of Efficiency and Strength of Fiber-Matrix Interface", *Journal of Composites Technology and Research*, JCTRER, v. 17, No. 4, October 1995, pp. 289-300.

[16]Dow, N. F., Rosen, B. W., "Evaluations of Filament-Reinforced Composites for Aerospace Structural Applications", *NASA CR-207*, April, 1965.

[17]Rosen, B. W., "Tensile Failure of Fibrous Composites", *AIAA Journal,* November, 1964, pp. 1985-1991.

[18]Gulino, R. and Phoenix, S. L., "Weibull Strength Statistics for Graphite Fibres Measured from the Break Progression in a Model Graphite/Glass/Epoxy Microcomposite", *Journal of Materials Science*, v. 26, 1991.

[19]De Luis, J. and Crawley, E.F., "The use of Piezo-Ceramics as Distributed Actuators in Flexible Space Structures", Massachusetts Institute of Technology, 1987.

[20]Henstenburg, R. B. and Phoenix, S. L., *Polymer Composites*, v. 10, 1989.

[21]Widom, B., "Random Sequential Addition of Hard Spheres to a Volume", *The Journal of Chemical Physics*, v. 44, No. 10, 1965.

[22]Renyi, A., Publ. Math. Inst. Hung. Acad. Sci., v. 3, p. 109, 1958.

[23]Rodgers, J. P., Bent, A. A., and Hagood, N. W., "Characterization of Interdigitated Electrode Piezoelectric Fiber Composites Under High Electrical and Mechanical Loading", SPIE Paper No. 2717-60, *Proceedings of the 1996 Symposium on Smart Structures and Materials*, San Diego, CA.

[24]ASTM, "Standard Test Methods for Tensile Properties of Polymer Matrix Composite Materials", D3039/D 3039M-93, *Annual Book of ASTM Standards*, v. 15.03, ASTM, Philadelphia, pp.118-27, 1995.

[25]MATLAB v. 4.2, On-line Manual, The Mathworks, Inc., 24 Prime Park Way, Natick, MA 01760.

[26]Zhang, Q. M., Zhao, J., Uchino, K., and Zheng, J., "Change of the Weak Field Properties of Pb(ZrTi)O3 Piezoceramics with Compressive Uniaxial Stresses and Its Links to the Effect of Dopants on the Stability of the Polarizations in the Materials", submitted to the *Journal of Materials Research*, April 1996.

Appendix A: Index of Equipment Suppliers

Electrode Material, 0.5 mil Copper/Kapton, *Southwall Technologies*, 1029 Corporation Way, Palo Alto, CA 94030.

Silver Ink, CB115, *DuPont Electronics*, Barley Mill Plaza, Wilmington, DE 19880.

PZT 5H Circular Fibers, *CeraNova Corporation*, 14 Menfi Way, Hopedale, MA 01747.

Baseline Epoxy, Epon 9405/9470 Resin, *Shell Chemical Company*, Houston, TX.

Air Release Agent, A530, *BYK Chemie GmbH*, Wesel, Germany.

Dispersant, Hypermer KD-2, *ICI Americas Inc.*, Wilmington, DE 19897.

Dielectric Filler, 1 μm dia 5H Powder, *Morgan Matroc* Inc., 232 Forbes Road, Bedford, OH 44146.

Ultrasonicator, Model VC-50, *Sonics and Materials*, Danbury, CT 06810.

Oil Bath, Exacal EX-250HT, *Neslab Instruments Inc.*, 25 Nimble Hill Road, Midland, MI 48686.

High Voltage Amplifier, Model 664, *Trek Inc.*, 3932 Salt Works Road, Medina, NY 14103.

Laser, Axiom 2/20, *ZYGO Corp.*, Laurel Brook Road, Middlefield, CT 06455.

Laser Sensors, LB11/70, *Keyence*, Woodcliff, NJ.

E-glass Fabric, E120/F155, *Hexcel Corp.*, Pleasanton, CA.

8501 Test Machine, *INSTRON Corp.*, 100 Royall Street, Canton, MA 02021.

Sulfuric Acid, Lot 2468 KTSB 95.8% H_2SO_4, *Mallinckrodt Baker Inc.*, Paris, KY 40361.

Appendix B: Additional Model/Experiment Correlation Plots

The following comprise the remainder of all plots (stiffness and actuation strain) prepared after testing. Note the overall good correlation.

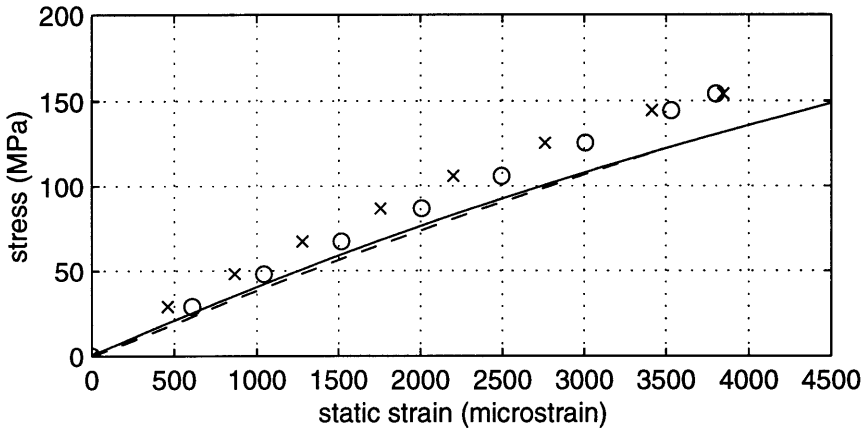

(a)

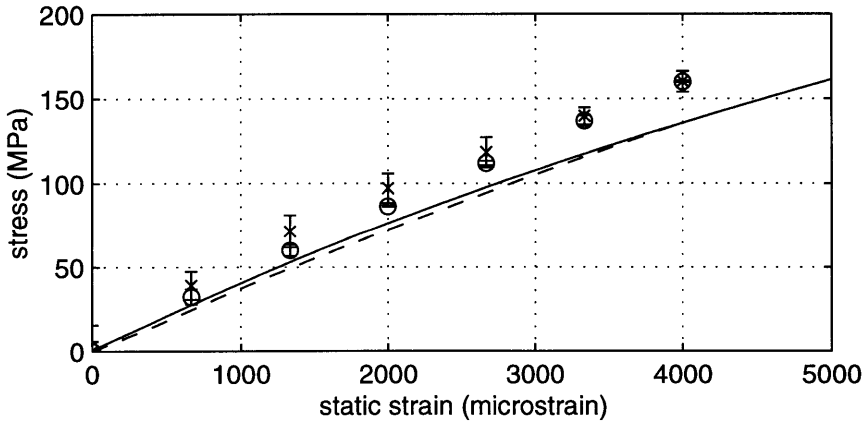

(b)

Figure A-1. Model/experiment correlation of stiffness for composites loaded to peak strains of (a) 3500 με, and (b) 4000 με. (-) FCL, (--) SCL.

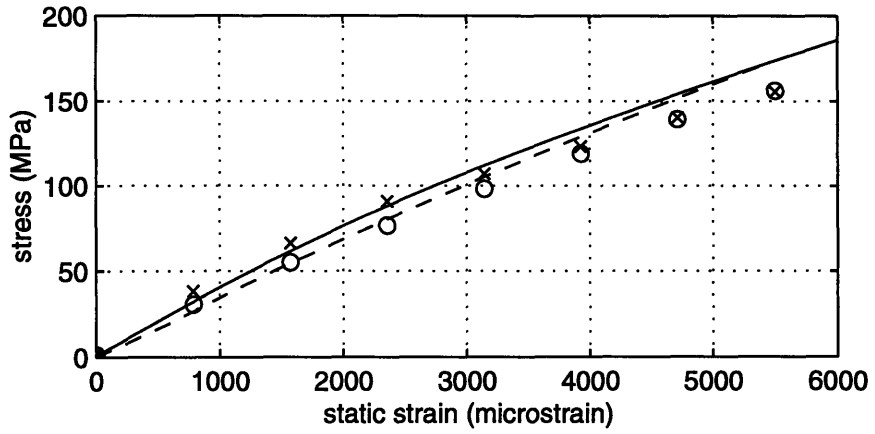

(a)

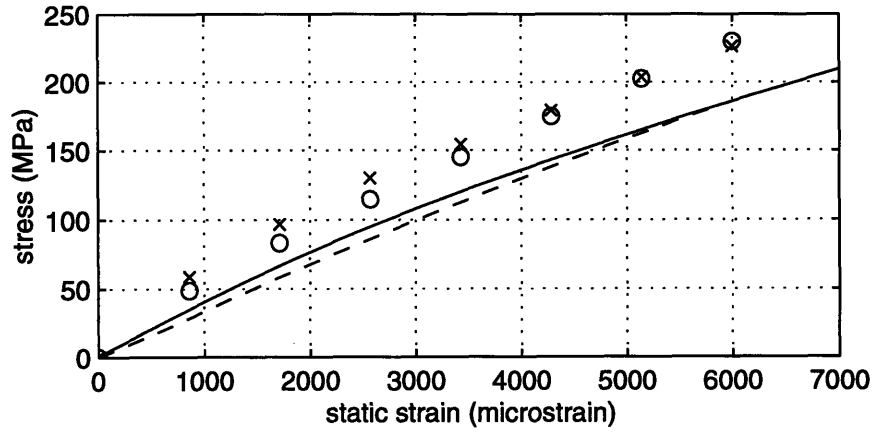

(b)

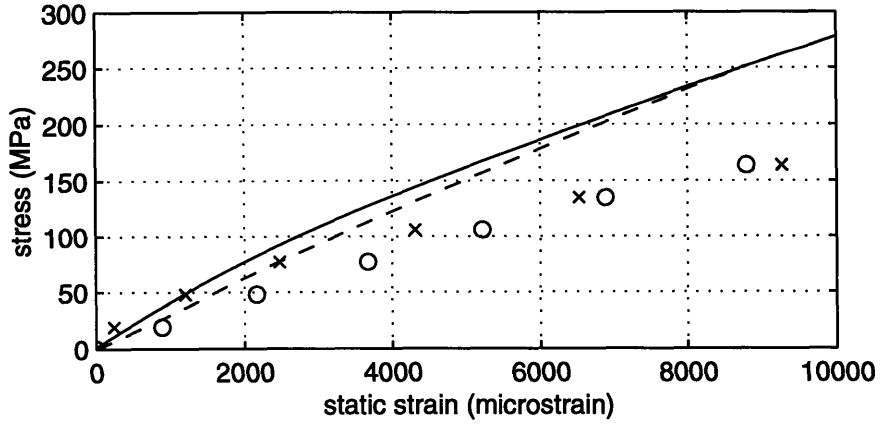

(c)

Figure A-2. Model/experiment correlation of stiffness for composites loaded to peak strains of (a) 5500 με, (b) 6000 με, and (c) 9000 με. (-) FCL, (--) SCL.

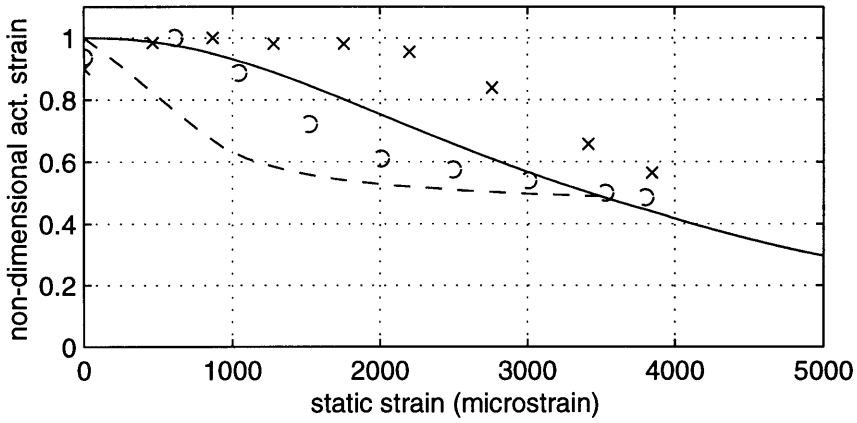

(a)

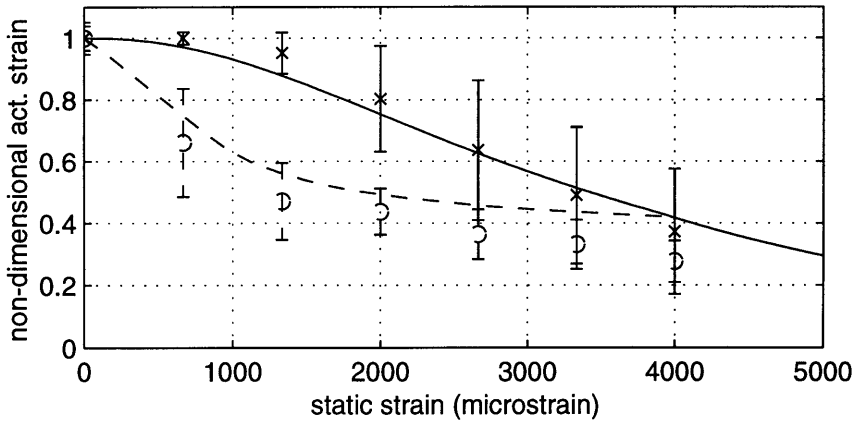

(b)

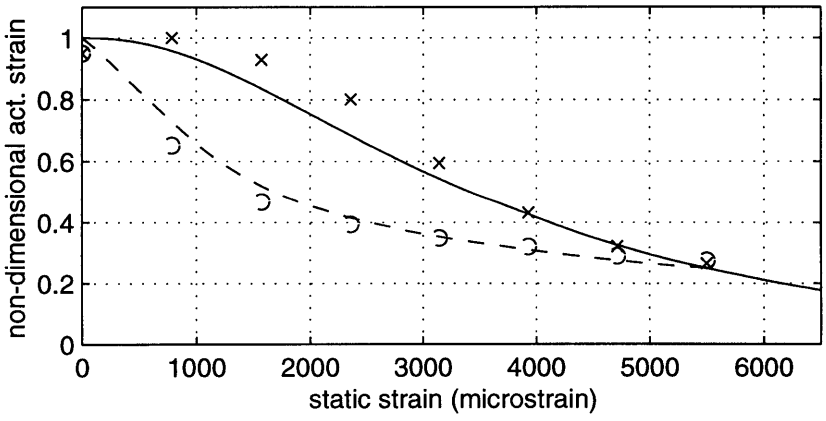

(c)

Figure A-4. Model/experiment correlation of actuation strain for composites loaded to peak strains of (a) 3500 με, (b) 4000 με, and (c) 5500 με. (-) FCL, (--) SCL.

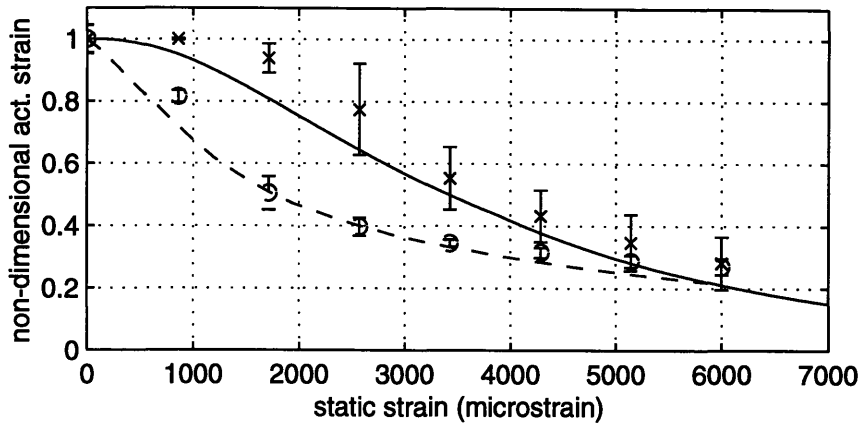

(a)

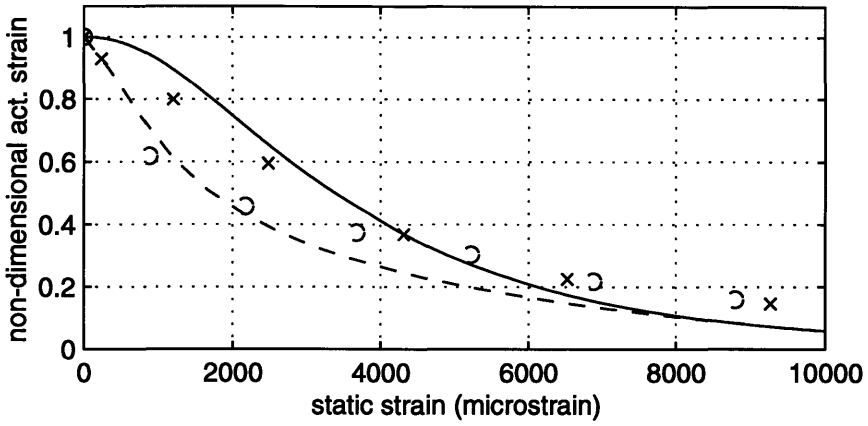

(b)

Figure A-5. Model/experiment correlation of actuation strain for composites loaded to peak strains of (a) 6000 με, and (b) 9000 με. (-) FCL, (--) SCL.

Appendix C: Additional Fragmentation Photomicrographs

The following are additional samples of photomicrographs taken after matrix dissolution for various peak strain values.

Figure B-1. Photomicrograph of composite AT92 loaded to a peak strain of 4000 με.

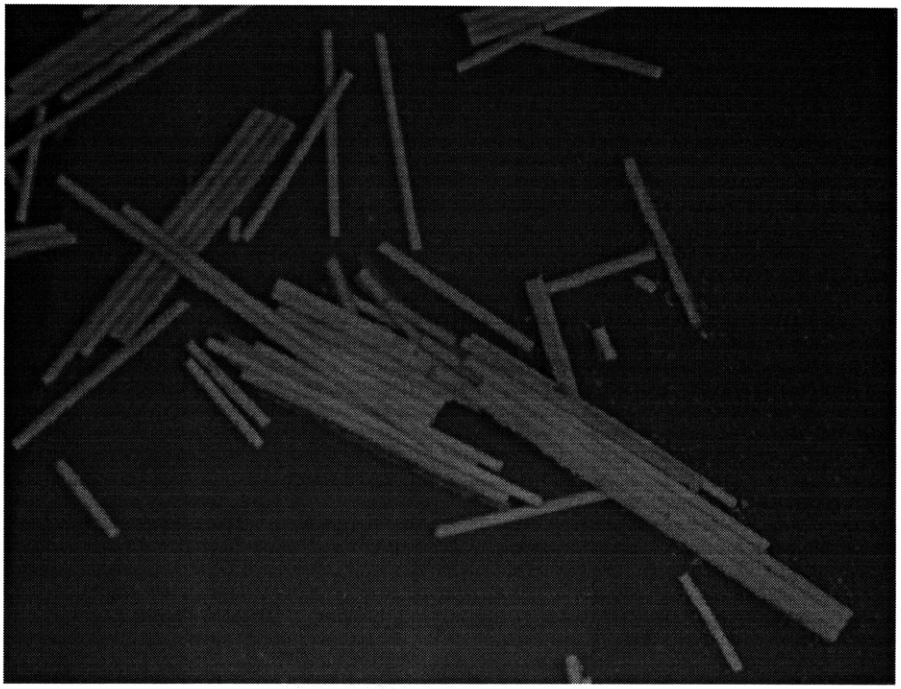

(a)

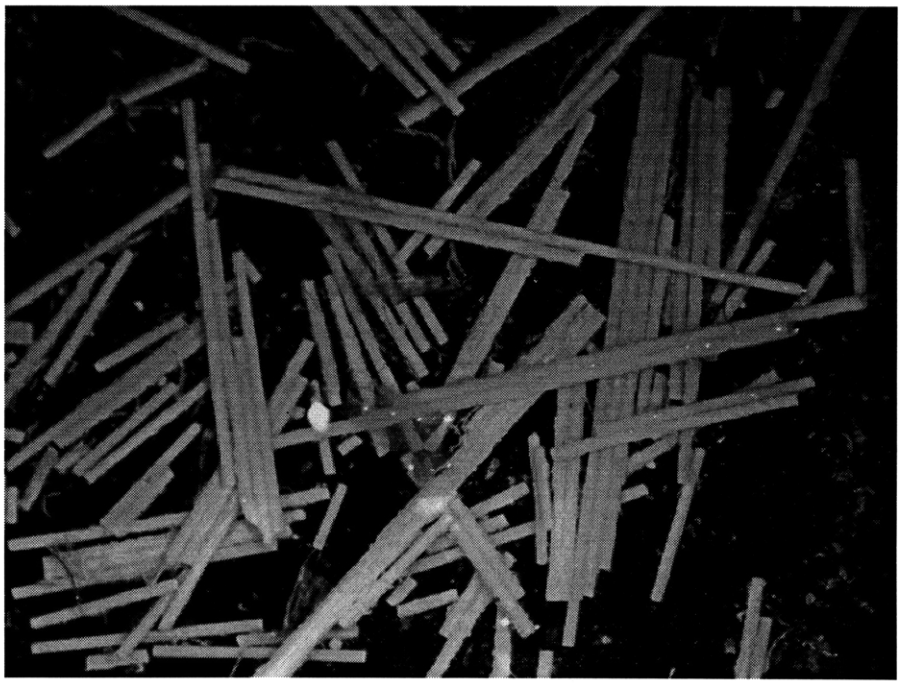

(b)

Figure B-2. Photomicrograph of composite (a) AT120 loaded to a peak strain of 4500 με, and (b) AT96 loaded to 6000 με.

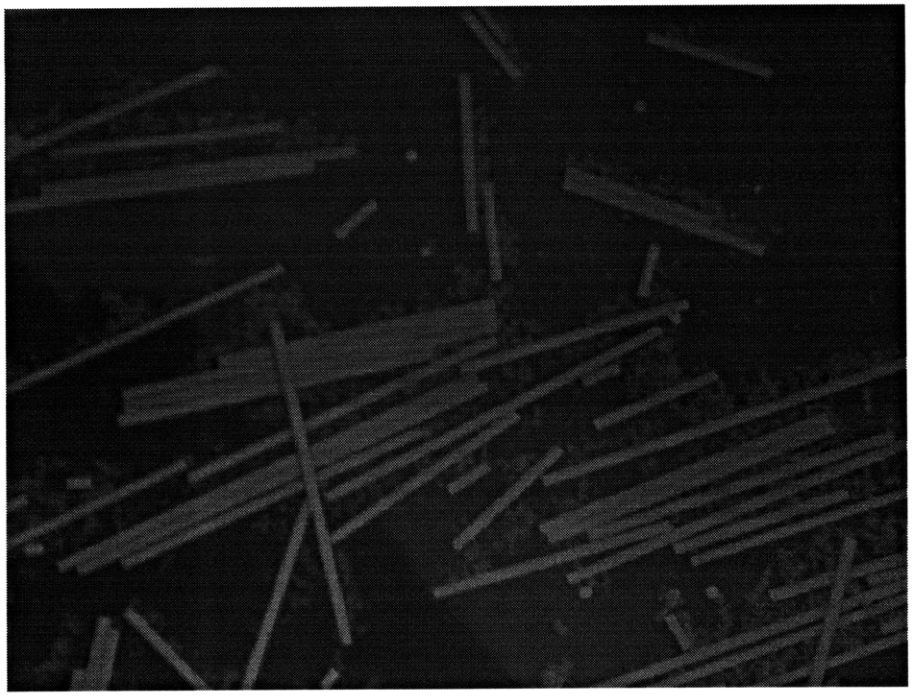

(a)

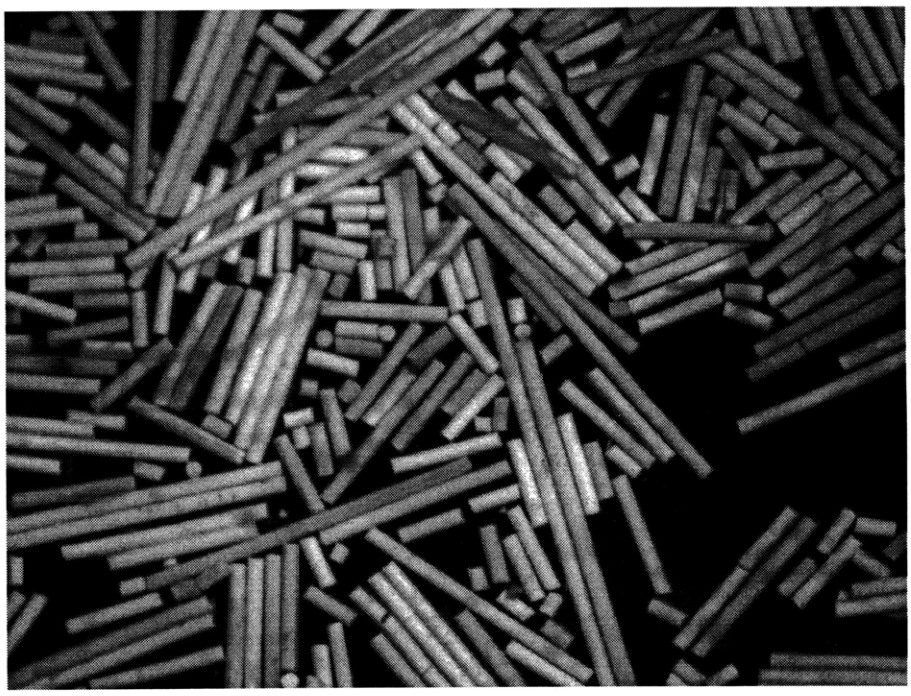

(b)

Figure B-3. Photomicrograph of composite (a) AT98 loaded to 8000 με, and (b) AT119 loaded to a peak strain of 10000 με.